First-principles electronic structure based investigations of Mn_2NiX magnetic alloys with Inverse Heusler structure

by

Souvik Paul

A Thesis
submitted for the degree of

Doctor of Philosophy

Thesis Supervisor

Dr. Subhradip Ghosh

Department of Physics
Indian Institute of Technology Guwahati
Guwahati 781039, India

August 2014

First-principles electronic structure based investigations of Mn_2NiX magnetic alloys with Inverse Heusler structure

by

Souvik Paul

A Thesis
submitted for the degree of
Doctor of Philosophy

Supervisor

Dr. Subhradip Ghosh

Department of Physics
Indian Institute of Technology Guwahati
Guwahati 781039, India

August 2014

Declaration

The work in this thesis is based on research carried out at the Department of Physics, Indian Institute of Technology Guwahati, India under the supervision of Dr. Subhradip Ghosh. No part of this thesis has been submitted elsewhere for any other degree or qualification. Works presented in the thesis are all my own unless referenced to the contrary in the text.

Signed: _____

Date: _____

Certificate

It is certified that the work contained in the thesis titled "*First-principles electronic structure based investigations of Mn_2NiX magnetic alloys with Inverse Heusler structure*" by Mr. Souvik Paul, a student of the Department of Physics, IIT Guwahati was carried out under my supervision and has not been submitted elsewhere for award of any degree.

Subhradip Ghosh

Some debts in life cannot be repaid, they can only be acknowledged. As a recognition of those unpayable debts, this dissertation is dedicated to ***my parents and Snigdha***.

Acknowledgements

First and foremost, I offer my sincerest gratitude to my supervisor Dr. Subhradip Ghosh for his guidance. I am thankful to him for his valuable suggestions, immense patience and lucid way of explaining the difficult concepts in condensed matter physics during my Ph.D. His insightful comments and constructive criticisms at different stages of my research were thought-provoking and they helped me to focus on my ideas. I am grateful to him for holding me to a high research standard and enforcing strict validations for each research results, and thus teaching me the proper way to research.

I take this opportunity to thank my doctoral committee members - Prof. S. Ravi, Dr. P. K. Padmanabhan and Dr. A. N. Panda for those immensely useful discussions during the yearly assessments of my research work. My special thanks go to the HODs, i.e., Prof. S. Ravi and Prof. S. Basu for providing me the opportunity of work in the department. I thank all the technical assistants, academic and non-academic stuff of the department who helped me in various ways during my research period. My thesis would have been incomplete without the fruitful discussions and useful collaboration from Dr. Biplab Sanyal, Uppsala University, Sweden. I would like to thank Dr. Biswanath Dutta for his selfless help during the early days of my Ph.D. I want to acknowledge Dr. Munima B. Sahariah for helping me in plotting with MATLAB. I am thankful to SINC-HPC2N, Sweden and CDAC, Pune, India for the allocation of supercomputing time. I also thank the department of Physics IIT Guwahati, India for allowing me to utilize Newton cluster, funded under the FIST programme by DST, India.

It is my great pleasure to thank all the research scholars of the department for providing such a friendly atmosphere throughout my doctoral years. My special thanks go to my senior and junior research scholars of the Numerical laboratory, they have been very kind and supportive. I thank my group members Debashish, Ashis and Srikrishna with whom I have shared many experiences of my research life. My batchmates - Apurba, Padam, Batakrushna, Swarnadeep, Deepanwita, Tribedi and Poulami have helped me to stay sane in the difficult periods. Special thanks to Soumen Da, Arindam Da, Ramesh, Biswajit, Anabil and Sk. Md. Obaidulla for their support to overcome setbacks and stay focused on my research. I greatly value their friendship and I deeply appreciate their belief in me. I would cherish their friendship throughout my life. I would always treasure the friendship of my childhood friends Suparna, Chiranjit, Bipradut and Subhajoy.

I feel privileged to thank all my teachers. I am blessed to get teachers like Dr. Kalyan Kumar Mondal, Dr. Muktish Achaaryya and Dr. Debopriya Shyam. I would like to thank Mr. Madhab Chandra Dutta and Mr. Ajit Kumar Ghosh who inspired me a lot to pursue physics during my younger days. My special thanks to Dr. Prabir Mukherjee and Dr. TaraShankar Nath whose simplicity and dedication towards their work still inspire me.

Most importantly, this doctoral work would have been impossible without the unconditional love, support and encouragement from my parents and Snigdha, to whom this dissertation is dedicated. I would like to express my heartfelt gratitude to Bubun, my maternal younger brother. The sisterly love of Tubli has influenced my life. I owe my life to them.

Abstract

The materials which respond reversibly to the environmental stimuli and adjust their physical, geometrical, mechanical and electromagnetic properties are often classified under the generic name “smart materials”. Shape-memory alloys (SMA) which have the peculiar ability to remember their original shape after deformations easily fit into this category. With the discovery of large magnetic field-induced strain in Ni-Mn-Ga magnetic SMA (MSMA), research in this area had flourished very rapidly. In this thesis, we have investigated various facets of Mn_2NiX (X= Al, Ga, In, Sn) materials, a possible set of shape memory alloys, with the help of first-principles electronic structure calculations. We have explored the energetics as a function of tetragonal deformation of the high temperature cubic phase in order to ascertain whether these materials would indeed exhibit shape memory effect. The results have been positive and encouraging, which motivated us to explore the origin behind the martensitic transformations, the key signature of potential shape memory effect, in these alloys. An investigation into the lattice dynamics of these materials pinpointed nesting in the Fermi surfaces of one of the spin bands as the mechanism behind the martensitic transformation. This study also indicates the existences of pre-martensitic modulated phases in all the materials. A deep exploration into the magnetic structures as a function of pressure, the crystal structure and chemical composition established that these materials would exhibit complex noncollinear spin structures only in a particular arrangement of atoms in the lattice and under finite pressure. This phenomenon carries, at least theoretically, the signature of magnetic barocaloric effect and adds to the list of functional capabilities of these materials. A quest for obtaining improvements in existing functionalities and for discovering more functionalities, led us to investigate the effects of anti-site disorder in selected sublattices on the magnetic properties. Our calculations indicate that due to presence of anti-site disorder, the martensitic transformations in these materials can be obtained by relatively small magnetic fields and that the materials would exhibit inverse magnetocaloric effects, both features being desirable for applications point of view. In a nutshell, the results presented in this thesis demonstrate the potentials of Mn_2NiX materials as a new series of multifunctional materials.

Contents

Acknowledgements **xi**

Abstract **xiii**

1 Introduction **1**
1.1 Smart materials . . . 1
1.2 Shape Memory Alloys (SMAs) . . . 3
1.2.1 Martensitic Transformation (MT) . . . 3
1.2.2 Shape Memory Effect (SME) . . . 5
1.2.3 Pseudoelasticity . . . 7
1.2.4 Applications of Shape Memory Alloys . . . 8
1.3 Magnetic Shape Memory Alloys (MSMAs) . . . 9
1.3.1 Ni-Mn based Magnetic Shape Memory Alloys (MSMAs) . . . 11
1.4 The role of first-principles electronic structure calculations in understanding materials properties . . . 16
1.5 Outline of the thesis . . . 17

2 Methods for calculating electronic structure in solids **23**
2.1 Introduction . . . 23
2.2 Density Functional Theory (DFT) . . . 24
2.3 Pseudopotential method . . . 28
2.3.1 The Phillips-Kleinman Construction . . . 28
2.3.2 Norm-Conserving Pseudopotentials (NCPP) . . . 29
2.3.3 Ultrasoft Pseudopotentials (USPP) . . . 29
2.4 Projector Augmented Wave (PAW) method . . . 30
2.5 Linearized Augmented Plane Wave (LAPW) method . . . 33
2.6 Korringa, Kohn and Rostoker (KKR) Green's Function method . . . 35
2.7 Exact Muffin-Tin orbital (EMTO) method . . . 38
2.8 Modeling of the chemical or substitutional disorder . . . 41
2.8.1 Coherent Potential Approximation (CPA) . . . 41
2.8.2 Special Quasirandom Structure (SQS) . . . 43
2.9 Summary . . . 44

3 Electronic structure, phase stability and possibilities of shape memory behavior in Mn_2NiX alloys **45**
3.1 Introduction . . . 45
3.2 Computational Details . . . 46
3.3 Results and Discussions . . . 48
3.3.1 Structural properties and energetics related to martensitic transformations . . . 48
3.3.2 Magnetic moments . . . 53
3.3.3 Electronic structures and analysis of the trends in phase stabilities and magnetic properties . . . 55
3.4 Summary . . . 62

4 Understanding the origin of the martensitic transformation in Mn_2NiX alloys from their lattice dynamics **65**
4.1 Introduction . . . 65
4.2 Computational details . . . 67
4.3 Results and Discussions . . . 70
4.3.1 Phonon dispersion . . . 70
4.3.2 Vibrational Density of States (VDOS) . . . 73
4.3.3 Inter-atomic force constants . . . 74
4.3.4 Fermi surfaces . . . 76
4.3.5 Elastic constants . . . 79
4.4 Summary . . . 81

5 Investigation of the magnetic structure of Mn_2NiX materials from the study of noncollinear magnetism **83**
5.1 Introduction . . . 83
5.2 Computational Details . . . 85
5.3 Results and Discussions . . . 87
5.3.1 Spin wave spectra of Mn_2NiX materials in inverse Heusler structure . . . 87
5.3.2 Band Structures and Fermi Surfaces . . . 89
5.3.3 Exchange interactions . . . 92
5.3.4 The role of chemical composition and crystal structure . . . 94
5.4 Summary . . . 97

6 Anti-site disorder driven improvements in the functionalities of Mn_2NiX materials **99**
6.1 Introduction . . . 99
6.2 Computational Details . . . 101
6.3 Results and Discussions . . . 103
6.3.1 Understanding the origin of discrepancy between theory and experiment for Mn_2NiSn . . . 103

6.3.2 Energetics of different configurations in Mn_2NiX materials 105
6.3.3 Dependence of the magnetic moments of Mn_2NiX on configurations . 108
6.3.4 Electronic structure of Mn_2NiX and dependencies on configurations . 110
6.3.5 Effects of configurations on exchange interactions and the Curie temperatures of Mn_2NiX 114
6.4 Summary 117

7 Conclusions and Scopes for future work **119**
7.1 Conclusions 119
7.2 Scopes for future work 121

Bibliography **123**

Publications **139**

Chapter 1

Introduction

During the past few decades, human intellects with the aid of science and technology have transformed the unimportant looking materials into sophisticated ones that can efficiently be utilized in advanced electronics and machineries. These developments would have never been achievable without immense improvements in the techniques of alloying, smelting and forging. With the combination of state-of-the-art theoretical methods and cutting-edge experimental techniques, we are now capable of unlocking the deepest mysteries hidden in the world of the materials. The knowledge of engineering material properties like physical, electrical, mechanical, thermal, optical, elastic, electromagnetic etc., have empowered us to fabricate materials with suitable properties for technological applications. The quest for novel materials that could miniaturize the mechanical, optical and electronic products and devices with improved properties and provide control over its functionalities like sensing, actuation, electromagnetic shielding, etc., has introduced a new class of materials called multifunctional materials. "Smart materials" belong to a special class of multifunctional materials that have sensing and actuation capabilities [1].

1.1 Smart materials

"Smart materials" or functional materials are the fruits of extensive research activities over the past few decades on technologies like tuning the materials mechanically for desired functional achievements, and thus to provide improved thermal and electrical properties [2–6].

These materials interact with their immediate environments to exhibit adaptive characteristics that fulfill previously impossible functions. Despite the fact that US miliary and aerospace departments had started to utilize smart materials from late sixties, it is only in recent times that these materials find applications in construction, transport, medical, leisure and domestic areas. These materials couple one or more properties together such that changing of one automatically changes the other. The changes in the materials can be achieved by external stimuli like stress, temperature, moisture, electric and magnetic fields. In addition, the term "smart materials" can be associated with those materials that can (i) respond reversibly to the changes in the surrounding environments, and (ii) provide an optimal response upon changes in the physical, geometrical, mechanical or electromagnetic properties. Researchers in this field are currently toiling in overcoming the unavailability of space, inadequate operating temperature, poor response time and forbidden cost. In this respect, it has to be mentioned that we have achieved considerable progress in the field of automotive sensors and actuators, integration with miniscule microcontrollers and advanced softwares. A sensor is a device that converts a mechanical signal to nonmechanical output, while an actuator does the exact opposite. One of the main advantages of these materials is that their mechanical response is one or more orders of magnitude larger compared to the response from conventional material behavior such as thermal expansion. There are many groups of smart materials, each exhibiting a particular property which can be harnessed in a variety of high-tech and everyday applications. These include piezoelectrics [7, 8] and electrostrictives [9] (coupling of mechanical and electric fields), piezomagnetics [10] and magnetostrictives [11] (coupling of mechanical and magnetic fields), and shape memory materials (coupling of thermal and mechanical fields) [1]. Depending upon the nature of coupling, smart materials can further be divided into two categories. Piezoceramics [12], piezoelectric polymers [13, 14], magnetostrictive ceramics, shape memory alloys and magnetic shape memory alloys exhibit direct coupling between mechanical and nonmechanical fields, whereas electro-rheological fluids (ERF) [15] and magneto-rheological fluids (MRF) [16], combine those fields via the viscosity of the materials [1].

1.2 Shape Memory Alloys (SMAs)

Shape memory alloys are the special kind of intermetallic compounds which have the peculiar property of remembering their original shapes and sizes, even after undergoing a structural deformation. First significant step towards the discovery of shape memory effect happened in 1930 [3]. The pseudoelastic behavior of Cu-Au alloys was first discovered by Swedish scientist Arne Ölander in 1932 [17]. In 1938, Greninger and Mooradian [18, 19] observed a displacive and diffusionless phase transformation from a high temperature phase to low temperature phase in Cu-Zn alloy. The term "shape memory" was first coined by Vernon in 1941 for his polymeric dental material [20]. Although the potential applications of SMAs were realized immediately after their discovery, their commercializations did not take place instantly. The reasons for the delay were due to the conventional melting, possessing, machining techniques and most importantly, due to the financial issues. Applications of SMAs in the engineering industry had started after Buehler and his colleges accidentally discovered NiTi while searching materials for heat shielding [21, 22]. They observed that in addition to exhibiting good mechanical properties, comparable to some common engineering metals, the material also possesses a shape recovery capability. Following this observation, in honor of its discovery at the Naval Ordnance Laboratory (NOL), US, the term "NiTiNOL" was proposed [23]. The discovery of NiTiNOL resulted in flurry of activities in the field of SMAs among the researchers. Thereafter, changes occurring in material's properties due to operation of heat, variation in compositions and appearance of micro-variants were widely investigated and researchers began to understand the underlying physics [1]. The shape memory effect is the recovery of the original structure of the material deformed by external forces as a result of increase in temperature, even if the applied force is relatively large. This property demands that these materials should possess higher energy density. However, low frequency response of the materials acts as a hindrance to limit their applications. In the next few subsections, some key features associated with shape memory alloys are described.

1.2.1 Martensitic Transformation (MT)

The martensitic transformation is often characterized by spontaneous symmetry-breaking displacive, diffusionless first-order phase transformation which is known to occur in many metallic alloys. The name martensite is after the German metallurgist Adlof Martens [24]. This

transformation portrays cooperative, homogeneous movements of atoms rather than long range diffusive displacements of atoms. The tiny movements of atoms, usually less than the interatomic distances, relative to their neighbors, result in extremely large macroscopic changes. The organized movements of large number of atoms with their neighbors are referred as military transformation, in contrast to civilian diffusion based phase transformation. As a consequence of diffusionless character of martensitic transformation, the martensitic phase is forced to form at low temperature, since diffusion is not conceivable in experimental time scale even to the interstitial atoms [25].

Crystallographically martensitic phase transformation is thought to occur via two mechanisms: (i) the Bain strain and (ii) the lattice invariant shear mechanism. The former was proposed by Bain in 1924 [26], which supplies the necessary strain for FCC to BCC structural transformation. This homogeneous volume conserving deformation produces 20% contraction along the z axis and expands the other two perpendicular axes (x and y) by 12% in the BCC structure.

During the martensitic transformation, the atoms are displaced in a very tiny amount relative to their neighbors to facilitate the formation of martensitic variants. However, the macroscopic effect is quite large which deforms the crystal structure. The passage of a slip dislocation through a crystal causes the formation of a step. The passage of many such dislocations on parallel slip planes causes macroscopic shear. Although slip causes a change in shape but not a change in the crystal structure [27].

According to the theory of martensitic transformation, the deformation that ignites the transformation must produce an invariant-plane strain, an undistorted and unrotated interface created due to the combination of large shear component and a small dilatational strain. However, the Bain strain cannot transform the structure alone, since no rotation is capable of modifying Bain strain into an invariant-plane strain. Nevertheless, when it combined with rigid body rotation, the overall homogeneous deformation produces an invariant-line strain; a stress-free and unrotated line joins the two phases. But, the experimentally observed shape deformation is an invariant-plane strain, and thus the above combination produces wrong crystal structure. This discrepancy is resolved with an additional contribution of shearing effect generated from slipping and twinning of micro-structures under lattice-invariant deformation [28]. The Bain strain and rigid body rotation produce a large structural deformation, while the

homogeneous lattice-invariant shear minimizes the strain energy generated by the deformation and produces the exact martensitic structure. [29–36].

1.2.2 Shape Memory Effect (SME)

Shape memory effect describes the ability of materials to recover the original shape of plastically deformed sample upon heating. This phenomenon is characterized with the crystalline phase change known as "thermoelastic martensitic transformation". At a temperature below the critical temperature, known as final martensitic temperature (M_f), the austenite phase completely transforms into martensitic structure. In this situation, the microstructures are designated with self-accommodating twins. Since the twinned martensitic structure is soft, it can easily be deformed to detwinned structures after applying appropriate amount of stress. Heating above a critical temperature, known as final austenite temperature (A_f), while unloading, recovers the original shape of the sample by converting the detwinned structure back into austenite structure [1]. The complete transformation cycle from austenite→martensitic→austenite can better be understood from a thermomechanical loading path, plotted in a 2D stress-strain-temperature diagram (F 1.1).

In F 1.1, σ represents the uniaxial stress on the sample and ε is the corresponding strain measured along the direction of the applied stress. Suppose, we begin at an initial position (point A), where the material is completely austenite. A stress-free thermal cooling up to a temperature M_f (point B) causes the material to completely transforms into twinned martensitic structure. After this point, several percentage yields can be obtained with tiny amount of stress. When the stress level exceeds σ_s, reorientation of the twinned martensitic variants along the direction of the applied stress starts. At the end of the plateau, i.e., at the stress level σ_f, the variants are completely oriented and detwinned martensitic structure is achieved. After this point, stress increases very rapidly against tiny increment in strain upto a point C. Unloading the stress while keeping the material's temperature fixed results in a linear decrease to a point D. At this point, the detwinned structure contains BD amount of residual strain. Upon heating, detwinned martensite starts transforming into austenite phase when a critical temperature, known as austenite start temperature (A_s), is reached (point E). The volume fraction of the austenite phase compared to the detwinned martensitic phase increases upon further increment in temperature and at a point F, the material fully recovers the

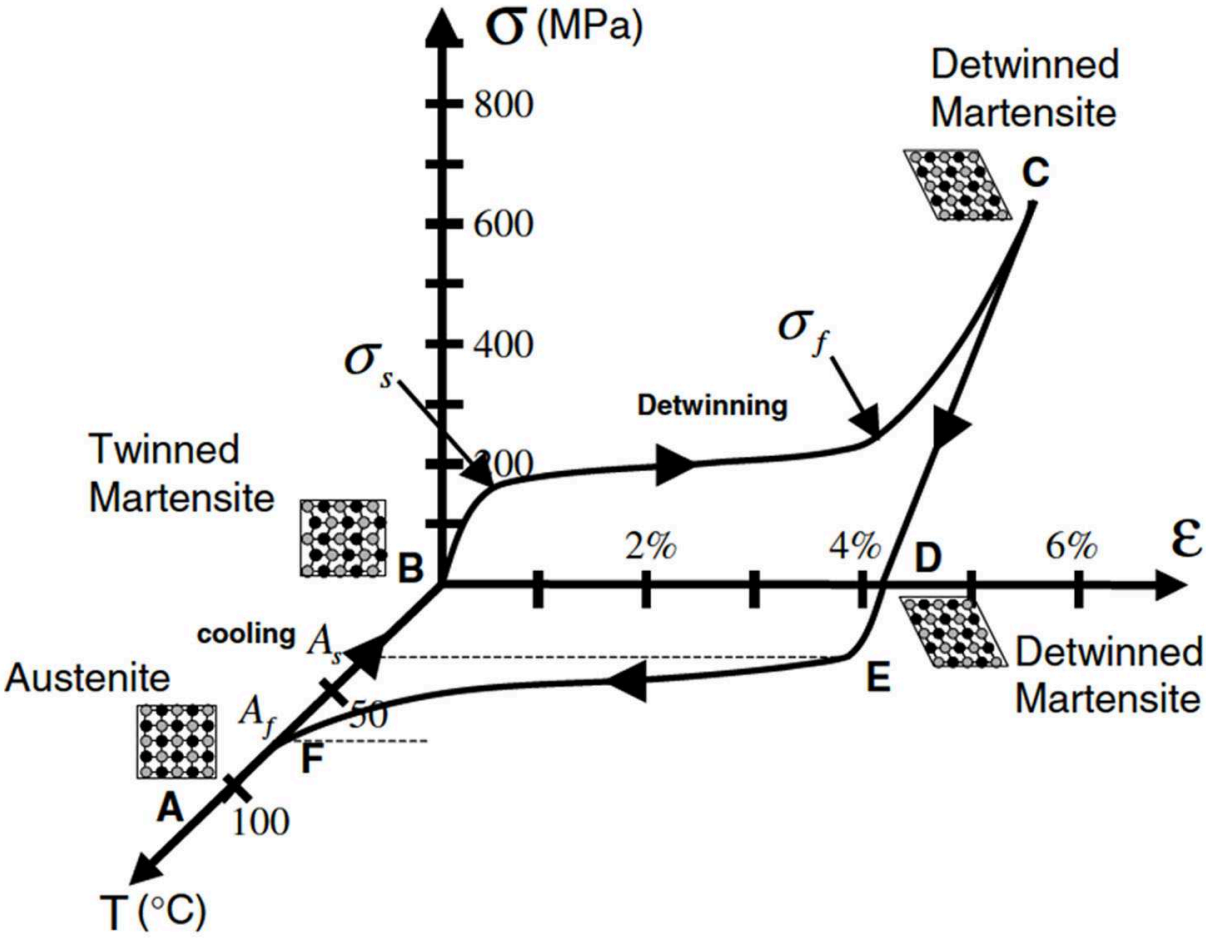

F 1.1: Stress-Strain-Temperature plot exhibiting the shape memory effect of a typical NiTi shape memory alloy [1].

residual strain and transforms completely into the austenite phase. Subsequent cooling below the temperature M_f again results in the formation of self-accommodated twinned martensitic variants, but with no associated shape change, and the whole cycle of the SME can be repeated. The above described phenomenon is called one-way shape memory effect, or simply SME, because the shape recovery is achieved only during heating after the material has been detwinned by an applied mechanical load [1].

The mechanism of shape memory effect described above allows the materials to remember only the high temperature austenite phase. However, it is possible for shape memory alloys to remember the shape of the martensitic phase under certain conditions [37, 38]. Two-way effect is not intrinsic to shape memory materials. Nevertheless, the materials adopt this behavior

after some specific thermomechanical treatments known as "training" procedure [3]. This property facilitates a spontaneous shape change of shape memory materials on both heating and cooling. Once the material has learned the behavior, it is possible to modify the shape of the material in a reversible way between the two shapes, only by changing of temperature across A_f and M_f without application of stress.

1.2.3 Pseudoelasticity

Pseudoelasticity or superelasticity represents a reversible elastic response of SMAs to the applied stress which occurs due to martensitic phase transformation between austenite and martensitic phases [39]. Contrary to the phenomenon described in the previous subsection, where temperature triggered the mertensitic transformation, pseudoelasticity is related to stress-induced transformation at a fixed temperature. A pseudoelastic loading path generally starts well above the temperature A_f, where stable austenite exists. Due to applied load on the austenite phase, detwinned martensite phase started to develop, and finally it returns to the initial austenite structure when the applied stress vanishes, thus the material behavior resembles elasticity [1]. A loading path (path 2) illustrating the pseudoelastic effect in details is shown in F 1.2.

When the material is mechanically loaded above temperature A_f, the austenite phase elastically transformed from point A to B. The line passing through the temperature M_s (martensitic start temperature) intersects the loading path at point B. Therefore, the stress level at this point, i.e., (σ^{Ms}), indicates that the material is on the verge of martensitic transformation. The volume fraction of detwinned martensitic phase compared to austenite phase increases as one moves from point B to C. The stress level at point C, i.e., (σ^{Mf}), where the loading path meets with the line passing through the temperature M_f, confirms the end of the transformation. Further loading beyond point C only increases the deformation in the detwinned martensite phase. When the stress is released, the detwinned martensitic phase elastically unload to point E. At this point, since the unloading path intersects the line passing through the temperature (A_s), the detwinned martensitic phase starts to convert into austenite phase. The strain recovery completes at point F which indicates end of the transformation. The material then elastically unloads to point A. The above loading and unloading cycle represents a hysteresis

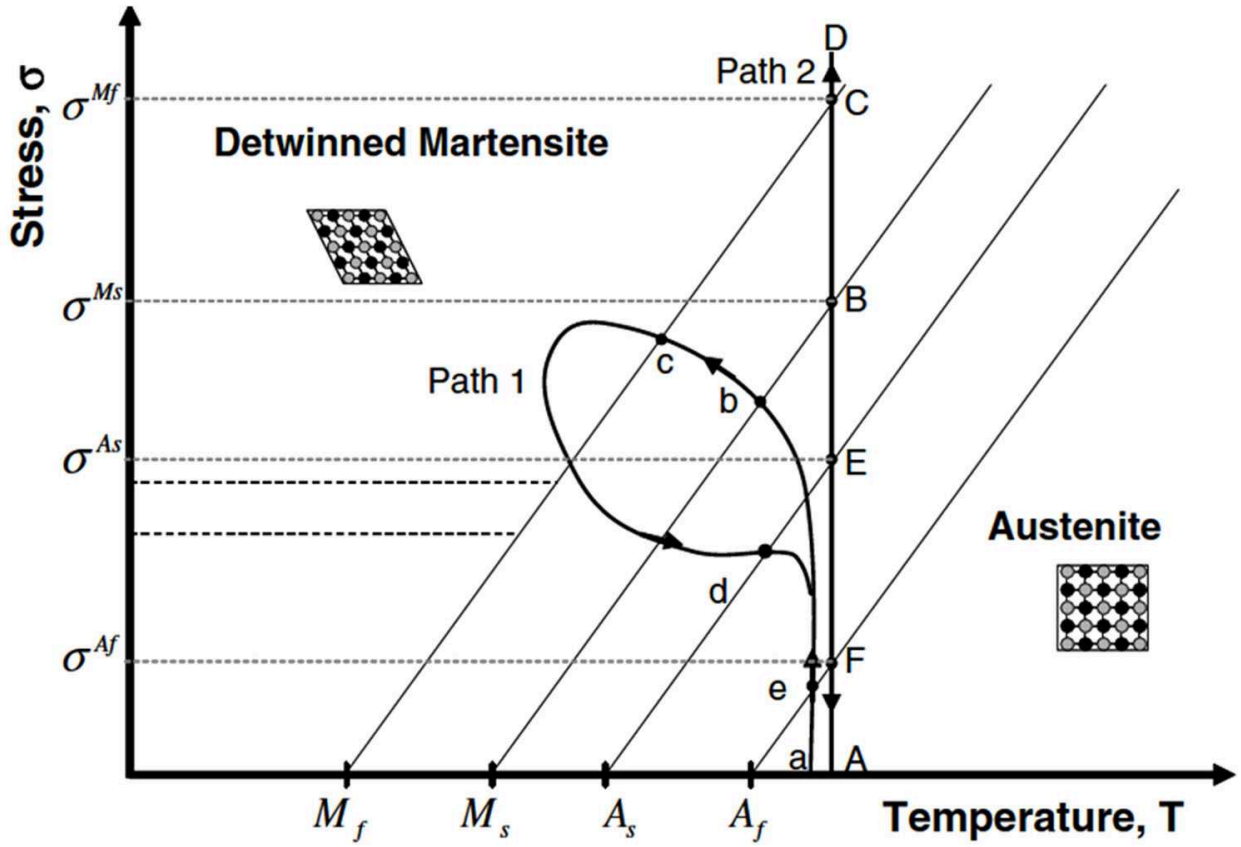

F 1.2: Phase diagram and two possible pseudoelastic loading paths [1].

in stress-strain diagram which accounts for the total dissipated energy during the transformation. The stress level corresponding to the beginning and ending of the transformation and the size of the hysteresis loop depend on the shape memory materials. Since the detwinned martensitic structure is formed during the transformation due to applied stress on austenite, they are called stress-induced martensite. There are many thermomechanical loading paths (like path 1) that also yield the formation of stress-induced martensite [1].

1.2.4 Applications of Shape Memory Alloys

In late sixties, the first successful technical use of shape memory alloys occurred for joining and fastening of tube and pipe couplings in aircraft and marine technology [3, 40]. The successful use of cryogenic Ni-Ti-Fe and Ni-Ti-Nb SMAs in high pressure hydraulic systems resulted in a large scale production of couplers in the following years [3, 41]. The latter SMA

is utilized in wire warp technology for nuclear application [42]. Ni-Ti based SMAs cannot be operated in hydrogen environment with high temperature and high pressure, due to hydrogen embrittlement. Super-elastic Ni-Ti SMAs have been registering continuous growth in applications like antennas, clothes, eyeglass, dental archwires and guidewires, etc. [3, 41]. The SMAs which possess wide hysteresis loop are used in variety of fastening applications [43]. Thermal shape memory actuators are used in thermal pressure control valves (Mercedes-Benz), carburetor ventilation valves, anti-scald valves, fire detection, smart idle screws, viscosity compensating devices, air-conditioning and ventilation devices [44]. Electrical shape memory actuators have replaced solenoid and electrical motors [41]. At present, huge demand for these actuators have been observed in robot technology, and most promisingly, several prototypes have been invented and successfully implemented. The most significant achievement of SMAs in medical science is to minimize the invasion procedure [45]. Medical devices build with SMAs are manufactured such that they can enter into the body through small opening, and change their shape inside the body cavity [42]. Needle wire localizer consisting of Nitinol is used to detect breast tumors because the subsequent surgery is more exact and less invasive [3]. A tube of SMA is inserted into clogged blood vessel, and due to body heat the memory material expands, which open the clogged arteries. Shape memory materials are applied for hip replacement and to repair broken bones [1]. The industrial safety valves build with Ni-Ti-Cu SMA are extensively used in petrochemical, semiconductor and pharmaceuticals industry and large oil and gas boilers, in order to minimize mishaps from toxic fluids and highly flammable materials [46]. Shape memory alloys gained popularity in recent past and at present, it is very active and promising research area. Researchers from all over the world frequently discovering new exciting physics based upon the already existing SMAs and materials with improved functional properties than the previous to overcome the barriers for advanced technological applications.

1.3 Magnetic Shape Memory Alloys (MSMAs)

After the invention of prominent shape memory effect in NiTi material, research activities on the new shape memory alloys with better functionalities had flourished. In particular, young researchers became excited due to the promises that those materials could efficiently act as actuating and sensing devices. Suddenly, huge demands of shape memory based technologies

were generated because they promised to be economical. The industries were contemplating on replacing the large complicated electro-mechanical devises with tiny and cheap shape memory crystals which consume less energy and can work for long time. Contrary to these expectations, it turned out that ordinary shape memory process in electro-mechanical devices is not really applicable. The hindrance occurs due to inherent slow heating and cooling rate against thermal control and therefore, additional devices are required to expedite the process, which in turn would increase cost and volume of the devices. The possibility of controlling shape memory effect by means other than temperature had opened up a research field aimed at designing next generation sensors and actuators which can operate efficiently at higher frequencies. Since controlling the magnetic field is easier than temperature, potential devices based on this effect were expected to be technologically much simpler.

In 1842, while examining a simple of iron, Joule invented that magnetic field can alter the dimensions of material which is merely an interplay between structural and magnetic degrees of freedom [47, 48]. Such an interplay, inherent to all magnetic materials, produces small changes to the dimensions of the cell. However, the deformation of the crystal structure in shape memory alloys originates from different microscopic mechanism. Normal ferromagnets like Fe and Ni exhibit strain associated with magnetostriction is $\sim 10^{-4}$%, while materials with large magnetostriction, for example Tb-Dy-Fe alloys (Terfenol-D), exhibit strain of nearly 0.1% [49]. In contrast, maximum magnetic field-induced strain (MFIS) achieved in magnetic shape memory materials till now is ~10% [50–52], two order of magnitude larger than those corresponding to conventional magnetostriction. Magnetic shape memory alloys possess all the properties of ordinary (non-magnetic) shape memory alloys. In addition to temperature and stress, magnetic field plays the role of extra degrees of freedom to achieve the desired functional effect.

Due to long-range magnetic ordering, below the Curie temperature, the martensitic variants (structural domain) remain magnetized [53]. The magnetizations of magnetic domains within those martensitic variants align themselves along their easy axis in such a way that it minimizes the magnetostatic energy [53–55]. If the magnetic anisotropy is weak, applied magnetic field only rotates magnetization directions of magnetic domains within martensitic variants which results in very small changes in dimensions and correspond to conventional magnetostriction. However, when the magnetic anisotropy is high and rotation of magnetic domains significantly increase the magnetic energy, the magnetic field orients the structural domains such that their magnetization axis becomes aligned with the external applied field

[56]. The difference in Zeeman energy [57] between the martensitic variants controls their rotational motion which brings about significant changes in the dimensions of the material [56, 58]. Generally, the deformation caused by induced strain is not restorable after the removal of the magnetic field. Reversibility in shape changes can only be achievable for small deformation. Besides heating the material, other possibilities to recover the induced strain are: rotation of the magnetic field and application of stress perpendicular to the magnetic field [56]. By extending the concept with conventional shape memory alloys, pseudoelastic or superelastic effect in magnetic shape memory alloys are termed with a prefix "magnetic". However, the main difference between thermally and magnetic-field induced pseudoelasticity is that the latter does not rely on the twin boundary motion, but on the coupling of structural and magnetic parameters at microscopic level leading to the possibility of inducing martensitic transformation upon application of a magnetic field. External magnetic field triggers the forward or reverse martensitic transformation depending upon whether austenite or martensite possess the higher magnetizations. Similar to thermally induced pseudoelasticity, the forward and the reverse transition in presence of magnetic field generates hysteresis loop [56].

1.3.1 Ni-Mn based Magnetic Shape Memory Alloys (MSMAs)

Till date, the most investigated magnetic shape memory alloy is Ni_2MnGa. This material generated tremendous interest when it was discovered because it exhibited a two-way shape memory effect and produced magnetic field-induced strain (MFIS) of about 6.6% in a magnetic field of less than 1 Tesla [59]. Subsequently, intense research has been carried out for over more than a decade. The primary focus has been to understand the structural and magnetic properties of these materials along with the mechanism of the mertensitic transformation. Numerous Xray diffraction (XRD) and Neutron scattering experiments have been performed to probe the crystal structure and structural parameters for the parent and the product phases of Ni_2MnGa [60–65, 68]. The high temperature austenite phase was unambiguously reported to be crystallizing in $L2_1$ structure, popularly known as Heusler structure [60–65] (F 1.3). Originated after a German engineer and chemist Friedrich Heusler, who investigated such an alloy in 1903, this intermetallic structure was found to be ferromagnetic. The associated space group is $Fm\bar{3}m$ (space group number 225) and can be best visualized with four interpenetrating FCC sublattice at (0,0,0), (0.50,0.50,0.50), (0.25,0.25,0.25) and (0.75,0.75,0.75). The octahedral symmetric positions, i.e., the last two sublattices, are occupied with Ni atoms and the

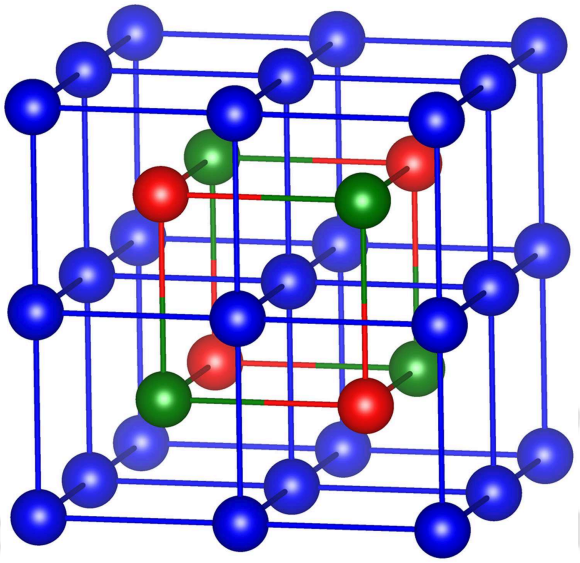

F 1.3: The cubic unit cell of the $L2_1$ Heusler structure. The blue, red and green spheres represent Ni, Mn and Ga atoms, respectively. Ni atoms occupy (0,0,0) and (0.50,0.50,0.50) sublattices, Mn atom sits in (0.50,0.50,0.50) sublattice and Ga atom fills (0.75,0.75,0.75) sublattice.

tetrahedral sublattices, i.e., first two sites, are occupied with Ga and Ni atoms, respectively. In Wyckoff notation, site symmetry of the first two occupied poisons are designated as 4a and 4b, and the last two equivalent occupied sites as 8c. Cu_2MnAl is considered as prototype for this class of materials. Experimental investigations found that the martensitic phase of Ni_2MnGa has nonmodulated tetragonal and orthorhombic structures [60, 63, 65, 68]. In addition to these martensitic phases, metastable premartensitic modulated phases are observed with $(c/a)< 1$ indicating a precursor phenomenon prior to the martensitic transformation [60, 64, 66, 68–71]. The unusual large magnetic field-induced strain in a moderate field, the observed large magnetocaloric effect [72] and the large negative magnetoresistance [73] makes the material a promising candidate for technological applications.

The understanding of the physics behind the martensitic transformation in Ni_2MnGa started with the understanding of precursor phenomenon in materials undergoing phase transition [5]. Precursor phenomenon or pretransitional phenomenon has been observed in varieties of materials like High T_C superconductors [74], ferroelectrics [75], manganites [76, 77] and shape memory alloys [78] via elastic constants and phonon anomalies [5]. This phenomenon arises as a result of mesoscopic texture within a single thermodynamic phase [5]. However, changes

in the physical properties occur at the nanometer level which result in satellite peaks in diffraction patterns implying the presence of modulated structures [79–83]. These meta-stable structures occur as an intermediate phase during the martensitic transformation and decide the way in which material approaches towards the martensitic phase. This type of transformation occurs due to lower resistive forces along specified direction decided by the symmetry of the high temperature phase. The high symmetric intrinsically unstable BCC structure lowers its symmetry due to internal displacements of each [110] planes along the $<1\bar{1}0>$ direction. It is important to mention that this property is not only limited to materials possessing cubic symmetry [5]. According to Friedel [84], since the transformation occurs at temperature higher than the Debye temperature, the crystal structure stabilizes due to excess phonon entropy caused by softening of phonon mode (acoustic TA_2) over the entire Brillouin zone [85]. The many observed varieties of the modulated (premartensitic) structures occur due to degrees of shuffling of [110] atomic planes with $<1\bar{1}0>$ vibration, which determines the periodicity of the stacking sequence in that phase. The periodicity of shuffled planes in the modulated structures is related to the pronounce softening of TA_2 phonon mode [5]. In 1947, while studying the kinematics of martensitic transformation in β-brass, Zener [86] proposed a model of soft mode that incorporated the elastic response of highly symmetric unstable austenite phase to energetically lower vibrational excitation. Since the shear elastic constant C' is a measure of resistance against a shear stress applied across [110] plane in $<1\bar{1}0>$ direction, the theory predicted that it would attain low value in the austenite phase compared to the other elastic moduli. Latter theoretical and experimental evidences showed that materials with BCC symmetry possess very low value of shear modulus. In effect, the softening of phonon branch and low value of shear modulus are the signatures of an unstable BCC structure that provide a channel through which the martensitic transformation can occur [5]. Certain shape memory alloys exhibit complete softening by exhibiting an anomalous dip in TA_2 phonon branch. This means that the phonon branch attains a minima at a particular wave vector $\mathbf{q}\neq 0$. The dip becomes more pronounced during cooling which means that the anomalous phonon branch softens most than the other branches. The origin of this anomaly is traced back to the nesting features of Fermi surfaces at specified wave vectors [87, 88]. Here, it is important to mention that the position of the dip depends on the compositions of the material. Although this kind of low energy excitations is not a necessary characteristic for the martensitic transformation to occur, however, it significantly alters the actual transformation path [5]. The wave vector corresponding to the pronounced phonon anomaly is related to the periodicity of the shuffling of atomic planes in modulated structure [89].

The theory of soft modes was first proposed by Anderson [90] and Cochran [91] for ferroelectrics to describe the structural phase transitions. They identified a particular transverse phonon branch whose displacement pattern is identical to the atomic displacements of the materials undergoing martensitic transformation. The restoring force of this branch weakens during cooling and finally frequency corresponding to that vibration branch vanishes at the transition temperature [5]. As a consequence, the parent phase becomes unstable and transforms into a low temperature structure.

Upon cooling below the martensitic temperature (T_M), the additional reflected peaks and diffraction angles in the X-ray diffraction measurements suggest existence of a periodical shuffling of atoms (modulation) along the [110] direction. Different types of modulated structures were found till now. If the modulation is formed in such a way that 5^{th} atomic plane along (110) direction remains in its original position, i.e., one period of modulation is accommodated in 5 (110) atomic planes, the structure is referred as 5M (M stands for monoclinic) modulation structure [64, 66, 70]. The corresponding modulation wave vector q/q_{max}= 0.4. However, based on more accurate results it was modified to q/q_{max}= 0.43. Similarly, for 3M modulated structure, the modulated wave vector was reported q/q_{max}= 0.33 [67, 70]. On the other hand, the structure 7M can be more complicated than a simple sine wave [65]. It can be a combination of several harmonics which leads to q/q_{max}= 0.28 [27].

For Ni_2MnGa, pronounced softening of TA_2 vibrational branch along [110] direction occurs at wave vector of ζ_0= 0.33 which implies the existence of premartensitic modulated structure [67, 70]. Experimental results reveal that premartensitic transformation begin at temperature T_{PM}= 260 K, which is well above the martensitic transformation temperature (T_M= 202 K) [92]. The energy of the soft mode increases as one approaches to the martensitic transformation temperature which signifies that softening of the vibrational mode is related to the premartensitic structure rather than to the martensitic one [27, 93]. It was shown that T_{PM} strongly depends on the external magnetic field while T_M has no such field dependence [94]. Analysis of the inelastic neutron scattering data in Ni-Al confirmed the presence of premartensitic structures. However, no measurement of premartensitic transformation temperature has been reported in Ni-Al. Apparently, the only relevant difference between Ni-Al and Ni_2MnGa is that the latter possesses a long range ferromagnetic order [95, 96]. Martensitic transformation in Ni_2MnGa can be suppressed with increasing the Ni content at the expense of Mn one [97]. The above facts clearly demonstrate that the coupling between magnetic and

elastic parameters drive the premartensitic transformation. However, recent experimental investigation on low energy spin wave and phonon anomaly in Ni_2MnGa showed no existence of magneto-elastic coupling between the respective parameters [27]. Therefore, the physical understanding of the microscopic origin of premartensitic transformation still remains incomplete and various characteristics have to be further examined in details before concluding to a comprehensive theory.

Low martensitic temperature (T_M~220 K) [60], having Curie temperature just above the room temperature (T_C~376 K) [60], brittleness in single crystalline form and excessive dependence of magnetic field-induced strain on the material structure pose restriction on the utilizations of Ni_2MnGa. Other Ni_2MnX (X= Al, Ge, In, Sn, Sb) [56, 98–101] Heusler alloys are incapable of exhibiting shape memory effect. Nevertheless, for all the materials, total magnetizations in the austenite phase are quite high (~4 μ_B), mainly for large localized moments in Mn sublattice (~3.5 μ_B). The total magnetizations are one of the important parameters for

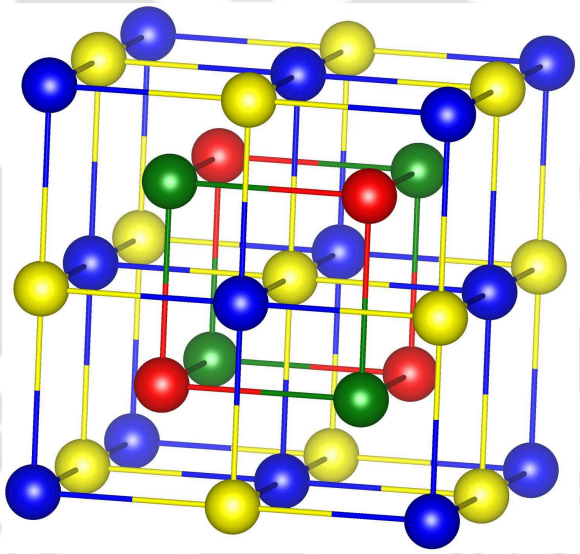

F 1.4: The cubic unit cell of the Hg_2CuTi inverse Heusler structure. The blue, green, yellow and red spheres represent MnI, MnII, Ni and Ga atoms, respectively. MnI, MnII, Ni and Ga atoms occupy (0,0,0), (0.25,0.25,0.25), (0.50,0.50,0.50) and (0.75,0.75,0.75) sublattices, respectively.

judging the industrial potentials of shape memory alloys, since magnetic field-induced strain is directly proportional to it. Therefore, quest for shape memory alloys with better functionalities automatically leads to Mn_2NiX materials, different aspects of which I studied intensively during my doctoral work.

Till date, the research on Mn_2NiX materials is rather few as the research on these materials with a focus to explore shape memory properties started very recently. The first successful attempt to measure the crystal structure of Mn_2NiSn was made way back in 1987 by Helmholdt and Buschow [102]. The Rietveld refinement analysis of their Neutron diffraction data collected at 4.2 K manifested that the crystal structure differs from usual Heusler structure. The results of Helmholdt and Buschow [102] revealed that the structure is inverse Heusler or Hg_2CuTi which is obtained from the Heusler structure when the position of Mn atom at (0.50,0.50,0.50) and Ni atom at (0.25,0.25,0.25) (in Ni_2MnGa) are interchanged, keeping position of the other two species unchanged (F 1.4). The structure can be associated with the space group $F\bar{4}3m$ (space group number 216). Due to lower point group symmetry (non-centrosymmetric cubic structure) than $Fm\bar{3}m$ space group, the degeneracy of 8c Wyckoff position is now broken, and occupied crystal positions (0.25,0.25,0.25) and (0.75,0.75,0.75) are denoted by 4c and 4d, respectively. After a long gap of 18 years, Liu *et al.* [103] first observed the shape memory effect in Mn_2NiGa. The material showed a martensitic transformation (T_M) at 270 K and a quite high Curie temperature (T_C) of 588 K, which is higher than prototype material Ni_2MnGa. The excellent field controllable shape memory effect up to 4% had been observed in this material. These results project Mn_2NiGa as a new promising shape memory material with functional parameters like T_M and T_C better than Ni_2MnGa. The only shortcoming of this material, in comparison to Ni_2MnGa, is its low magnetizations of about 1.2 μ_B/f.u [103–107]. Interestingly magnetic measurements on Mn_2NiSn obtained significantly high magnetizations of about 2.5 μ_B/f.u. [102] and 2.95 μ_B/f.u. [108]. These results thus indicate that the physics of Mn_2NiX materials could be quite interesting and thus worth exploring.

1.4 The role of first-principles electronic structure calculations in understanding materials properties

An understanding of materials properties from microscopic point of view can be obtained from *ab initio* calculations of their electronic structures. This means that one has to obtain the solution of Schrödinger equation for electrons in real solids, where their quantum mechanical

behavior is determined by the presence of other electrons and atomic nuclei. For such a many body interacting system, exact solution of the Schrödinger equation is not possible. However, this situation can be overcome by appropriate approximations. Recent advancements in computational powers and developments in the accuracy and efficiency of calculation strategies have greatly expanded our capabilities. Along with the improvements in computer based knowledge, theoretical breakthrough in the fields of nonempirical and parameter free "first-principles" methods have been achieved which project the many body interacting system onto a noninteracting single particle one, where a single term, known as exchange-correlation term, contains all the information about many body interactions [109–111]. Integration of first-principles based methods with advanced softwares facilitate tackling problems of wide variety accurately and successfully within reasonable time periods [110, 112–120]. Over the years, application of these methods in calculating the electronic structures of collinear and complex noncollinear magnetic ground states [121–124], dynamical properties of materials [125–127] and simultaneous comparison of these results with experimental observations confirmed the accuracy of these methods. Various problems related to disordered alloys [128–135] have also been encountered with these sophisticated tools. Now-a-days, these methods are widely accepted to predict properties of new materials where experimental evidence is not present. Therefore, we conclude that first-principles electronic structure methods are the essential theoretical tools to calculate the properties of the materials that we have planned to investigate during my doctoral research accurately.

1.5 Outline of the thesis

The available results on Mn_2NiX alloys revealed that the materials may have interesting functional properties worth investigation. In particular, the promising features of Mn_2NiGa warrant deeper explorations into the physics of these materials. In this thesis, we carry out first-principles based detailed investigations into the following aspects of Mn_2NiX (X= Al ,Ga, In, Sn) materials:

1. the possibilities of observing the SME in all the materials.

2. the mechanism behind martensitic phase transformations in these materials.

3. the magnetic structures of these materials and their possible connections to their functionalities.

4. the effect of chemical ordering and the possible consequences on the functionalities.

In the following paragraphs we briefly describe the contents of chapters of my thesis, starting from the second one.

Chapter 2 contains a description of the theoretical background on techniques that have been used. It starts with a brief description of the Density Functional Theory (DFT) formalism, a robust and efficient tool to solve many body problem in condensed matter physics in a computationally tractable way. Various implementations of the DFT which are used in this work are described next. In this work, we have used four different implementations: the Plane Wave Pseudopotential (PWPP) method, the Full Potential Linearized Augmented Plane wave (FP-LAPW) method, the Full Potential Korringa Kohn Rostoker (FP-KKR) method and the Exact Muffin Tin Orbital (EMTO) method. The choice of a particular implementation depends on the nature of the problem. In the Pseudopotential method, the central idea is to replace the actual crystal potential by an artificial (Pseudo) potential such that the wave functions in the core and in the valence regions join smoothly across the boundary in order for the quantum mechanical operators be expressible in a simple plane wave basis set with a reasonable computational cost. A more accurate description of the potentials and wave functions are provided by the full potential methods and FP-LAPW is one of them. In this method, the core region is described by a Muffin-tin approximation to the crystal potential. The FP-KKR and the EMTO methods are based on multiple scattering approaches. The importance of these methods is that the energy spectrum is obtained by solving the Green's function and hence the configuration averaging in case of disordered systems can be carried out in an efficient way. The most extensively used method to treat chemical and magnetic disorder is the Coherent Potential Approximation (CPA). Both FP-KKR and EMTO methods, in their current implementations, use CPA to study disorder, while for PWPP and FP-LAPW methods, the disorder is modeled by construction of large and artificial supercells. Thus, if the system possesses chemical and/or magnetic disorder, FP-KKR-CPA and EMTO-CPA methods are advantageous to use.

In Chapter 3, we first explore the possibilities of realizing shape memory effects in Mn_2NiX (X= Al, Ga, In, Sn) alloys, followed by an analysis of their electronic structures. We find volume conserving structural transformation from cubic (austenite) to nonmodulated tetragonal (martensite) phases in all four systems. We come to this conclusion based upon the energy

landscapes (energy versus (c/a) plot, where (c/a) determines the tetragonal deformation) as in all four cases global minima are obtained for $(c/a)\neq 1$. In addition, we find shallow minima in the energy landscapes of all four, which are indicative of the existences of modulated premartensitic structures. From the trends in the energy landscapes, we conclude that only Mn_2NiGa and Mn_2NiAl would be suitable for practical applications, since the T_M for these two materials only, would lie close to the room temperature. The trends in the energetics across the materials are explained by the hybridizations between Ni and two Mn atoms occupying crystallographic inequivalent positions in the inverse Heusler structure. We conclude that a relatively weaker hybridization between the magnetic atoms is responsible for a nearly stable cubic phase at low temperatures for Mn_2NiIn and Mn_2NiSn. The magnetic moments of the alloys are governed by the Mn atoms which are antiferromagnetically coupled and thus produce a smaller net moment in comparison to Ni_2MnX alloys. The net moments in Mn_2NiIn and Mn_2NiSn are smaller than the other two alloys by at least a factor of two. These trends are consistent with the weak hybridizations between the magnetic atoms in Mn_2NiIn and Mn_2NiSn arising due to larger distances between the magnetic atoms. The *sp* elements do not seem to play any direct role, except modifying the relative inter-atomic distances between the magnetic constituents influencing the hybridizations between them. Thus, the physical properties of these materials can be related to the relative sizes of the *sp* constituents. In a nutshell, this chapter demonstrates the shape memory possibilities in all four alloys considered and discuss their electronic structures and magnetic properties, making a comprehensive and comparative study.

In Chapter 4, we carry out investigations into the lattice dynamics of Mn_2NiX alloys in order to understand the origin of the martensitic transformations in these systems. In our study, the transverse acoustic TA_2 branch in the phonon dispersion plots for Mn_2NiX materials along $[\xi\xi 0]$ direction, ξ being the phonon wave vector, show unstable phonon modes, which are in accordance with our results of Chapter 3 that high temperature austenite phases of these materials are unstable. We try to explain the qualitative and quantitative features in the phonon dispersion plots from the vibrational densities of states, features in Fermi surfaces and elastic constants. We find that pure mechanical instabilities can be associated with Mn_2NiGa and Mn_2NiAl. We understand the features of the vibrational densities of states from the inter-atomic force constants associated with their nearest neighbor environments. We find that the nesting features in the minority band Fermi surfaces are responsible for the anomalous phonon instabilities in these systems. The phonon wave vectors at which the instabilities

are most pronounced indicate the possibilities of occurrences of premartensitic modulated phases, corroborating our findings of Chapter 3. However, the results also indicate that these premartensitic modulated phases could be quite complex and further investigations, both experimental, and theoretical, into this aspect are necessary.

In Chapter 5, we investigate the ground state magnetic structures of Mn_2NiX alloys. Specifically, we look into possibilities of stable noncollinear spin structures by computations on various spin spiral states. Till now, to the best of our knowledge, no magnetic shape memory alloy is reported having noncollinear magnetic structure as the magnetic ground state. Previous calculations on Ni_2MnGa and Ni_2MnAl alloys in Heusler structure did not find any spin spiral state as the lowest energy state. Our calculations showed that under about 3.5% compressions of the lattices, that is under external pressure, magnetic structures of Mn_2NiGa, Mn_2NiAl and Mn_2NiSn transform from a collinear ferrimagnetic state to noncollinear states, which are combinations of different planar spin spirals. For Mn_2NiIn, further compressions would be necessary to stabilize a noncollinear state. This phenomenon carries tremendous importance with respect to functionalities of these materials as this may be a signature that these materials would exhibit magnetic barocaloric effect (BCE). Our analysis shows that the hybridizations between the two spin bands (up and down) open up a hybridization gap at the Fermi level. This along with the nesting of spin-majority and spin-minority parallel Fermi sheets is responsible for the stabilizations of the spin spiral states over the collinear ones. We analyze these results further by computing the inter-atomic and intra-atomic exchange interactions. The results demonstrate that the magnetic frustrations of the Mn atoms at the octahedral sublattices stabilize the noncollinear spiral structures. Simultaneous investigations of the spin wave excitations of Ni_2MnX systems in Heusler structure demonstrate that the inverse Heusler type arrangement is necessary to obtain stable noncollinear spin configurations in Ni-Mn-*X* systems. In summary, the work of this chapter shows another distinctive feature of Mn_2NiX systems arising out of the structural arrangements of atoms, and that the effects of this on the ground state spin structures can be utilized for functional features.

In Chapter 6, we focus on the effects of chemical order on the functionalities in Mn_2NiX alloys. Recent experiments on Mn_2NiGa and Mn_2NiSn predicted that the arrangements of various species in these two systems are not exactly perfectly ordered inverse Heusler, but that the octahedral sites have disordered Ni_xMn_{1-x} configurations. Our investigations show that the introduction of such anti-site disorder on the octahedral sublattices improves the magnetizations by and order of magnitude in all four alloys under consideration. The impact from the

functionality point of view is that it magnifies ΔM which is the magnetization in the martensitic phase with respect to that in the austenite phase, resulting in a large Zeeman energy at relatively small magnetic field, a feature that facilitates martensitic transformation with application of relatively small magnetic field. The magnitude of ΔM being negative implies that these materials exhibit inverse magnetocaloric effect (MCE), a requirement for Green technology in refrigeration, for example. The results of this chapter is extremely significant as they demonstrate that the intrinsic partial disorder in these materials lead to significant advantages over the prototype Ni_2MnX systems with regard to various functionalities.

Chapter 7 concludes with a summary of the main results of the thesis. The importance of these results along with the possible extensions are discussed thereafter.

Chapter 2

Methods for calculating electronic structure in solids

2.1 Introduction

The electronic structure of a solid can be obtained by solving the many body Schrödinger equation

$$\mathcal{H}\Psi(\mathbf{r}_1, \mathbf{r}_2, ..., \mathbf{r}_i, ..., \mathbf{R}_1, \mathbf{R}_2, ..., \mathbf{R}_I, ...) = E\Psi(\mathbf{r}_1, \mathbf{r}_2, ..., \mathbf{r}_i, ..., \mathbf{R}_1, \mathbf{R}_2, ..., \mathbf{R}_I, ...) \quad (2.1)$$

where $\Psi(\mathbf{r}_1, \mathbf{r}_2, ..., \mathbf{r}_i, ..., \mathbf{R}_1, \mathbf{R}_2, ..., \mathbf{R}_I, ...)$, the many body wavefunction, contains all the information about electrons and nuclei. The indices i and I are for electrons and atomic nuclei, respectively. $\mathcal{H}$ is the Hamiltonian and E the total energy of the system. The Hamiltonian describes the motion of each individual electron and nuclei for every atom in the system and thus, takes the following form

$$\mathcal{H} = -\frac{\hbar^2}{2}\sum_I \frac{\nabla_I^2}{M_I} + \frac{1}{2}\sum_{I\neq J}\frac{Z_I Z_J e^2}{|\mathbf{R}_I - \mathbf{R}_J|} - \frac{\hbar^2}{2}\sum_i \frac{\nabla_i^2}{m_i} + \frac{1}{2}\sum_{i\neq j}\frac{e^2}{|\mathbf{r}_i - \mathbf{r}_j|} - \sum_{i,I}\frac{Z_I e^2}{|\mathbf{r}_i - \mathbf{R}_I|} \quad (2.2)$$

where M_I denotes nuclear mass, m_i is the electron mass, $\mathbf{R}_I$ and $\mathbf{r}_i$ stand for nuclear and electron coordinates, respectively, and Z denotes the atomic number. The first and third terms in the Hamiltonian are kinetic energies of nuclei and electrons, respectively. The second,

fourth and fifth terms are Coulomb interactions between nuclei and nuclei, electrons and electrons and electrons and nuclei, respectively.

The nuclear degrees of freedom can be disentangled from the electronic ones via adiabatic approximation [136]. Being much lighter than the ions, electrons can move much faster than nuclei in the solid. The time scale for the electronic relaxation is usually much smaller than the ones for the ions. This effectively means that the ions can be considered at rest while studying the electronic degrees of freedom. Thus the total wave function of the system can approximately be written as the product of the functions describing the ions and the electrons. Thus the electronic structure problem can be solved by concentrating on the many body Schrödinger equation for electronic degrees of freedom only. Within this approximation, the electronic description can be given as,

$$\mathcal{H}_e \psi_e = E_e \psi_e \tag{2.3}$$

where the Hamiltonian is given by

$$\mathcal{H}_e = -\frac{\hbar^2}{2}\sum_i \frac{\nabla_i^2}{m_i} + \frac{1}{2}\sum_{i\neq j}\frac{e^2}{|\mathbf{r}_i - \mathbf{r}_j|} - \sum_{i,I}\frac{Z_I e^2}{|\mathbf{r}_i - \mathbf{R}_I|} = T + W + V_{ext} \tag{2.4}$$

The first term, T, is the kinetic energy of the electrons. The second term, W, is the Coulomb potential and the third term, V_{ext} is the external potential.

2.2 Density Functional Theory (DFT)

In spite of simplifications achieved by the adiabatic approximation, the problem still remains a many body one and is practically impossible to solve for solids even with modern day computers. The Density Functional Theory (DFT) developed half a century ago, provides an excellent way to circumvent this problem.

Due to its remarkable success in describing the ground state properties of large number of materials in different forms like bulk, surfaces, interfaces, nanostructures, DFT has become the essential computational tool of modern day electronic structure calculation. Instead of complicated many body wave function formalism, which depends on the coordinates of all

the electrons in the system, DFT immensely simplify the many body problem by constructing the ground state properties as functionals of single particle electronic charge density. The basis of DFT is the following two theorems proposed by P. Hohenberg and W. Kohn [109]

Theorem I: For any system of interacting particles in an external potential $V_{ext}(\mathbf{r})$, the potential $V_{ext}(\mathbf{r})$ is determined uniquely, except for a constant, by the ground state particle density $n_0(\mathbf{r})$ [110].

Theorem II: A *universal functional* for the energy $E[n]$ in terms of density $n(\mathbf{r})$ can be defined, valid for any external potential $V_{ext}(\mathbf{r})$. For any particular $V_{ext}(\mathbf{r})$, the exact ground state energy of the system is the global minimum value of this functional, and the density $n(\mathbf{r})$ that minimizes the functional is the exact ground state density $n_0(\mathbf{r})$ [110].

Since the functional $E[n]$ is not known, the Hohenberg-Kohn theorems, at first, appear to be inappropriate for practical application. However, Kohn and Sham later transformed the rather abstract looking theorems into a practical scheme [111]. The basic idea of Kohn-Sham approach is the introduction of an auxiliary noninteracting electronic system where the electrons are exposed to an effective external potential $V_{eff}(\mathbf{r})$. The constrains on the effective potential is that the resulting density of the noninteracting system equals to the density of the true interacting system. This procedure of Kohn-Sham along with the variational principle leads to Schrödinger-like equations:

$$(H_{KS} - \epsilon_i)\phi_i(\mathbf{r}) = 0, \tag{2.5}$$

where ϵ_is are the eigenvalues and H_{KS} is the effective Hamiltonian.

$$H_{KS} = -\frac{1}{2}\nabla^2 + V_{eff} \quad (in\ Hartree\ units) \tag{2.6}$$

with

$$V_{eff} = V_{ext}(\mathbf{r}) + V_{Hartree}(\mathbf{r}) + V_{xc}(\mathbf{r}) \tag{2.7}$$

The second term is called Hartree potential,

$$V_{Hartree} = \frac{1}{2}\int \frac{n(\mathbf{r})n(\mathbf{r}')}{|\mathbf{r} - \mathbf{r}'|}\, d\mathbf{r}d\mathbf{r}' \tag{2.8}$$

and the last term is exchange-correlation potential defined as,

$$V_{xc} = \frac{\delta E_{xc}[n]}{\delta n(\mathbf{r})} \tag{2.9}$$

where E_{xc} is the difference between the kinetic energy plus the internal interaction energies of the true interacting many body system and those of the auxiliary single particle system with electron-electron interactions replaced by the Hartree energy. The density is calculated from single-electron orbitals

$$n(\mathbf{r}) = \sum_{i=1}^{N} |\phi_i(\mathbf{r})|^2 \tag{2.10}$$

and the total number of electron is

$$N = \int n(\mathbf{r})\, d\mathbf{r} \tag{2.11}$$

Within the Kohn-Sham approach, expression for the ground state energy functional turns out to be

$$E_{KS} = T_s[n] + \int V_{ext}(\mathbf{r}) n(\mathbf{r})\, dr + E_{Hartree}[n] + E_{xc}[n] + E_{II} \tag{2.12}$$

where E_{II} is the interaction between the nuclei. The single particle kinetic energy T_s is given by

$$T_s = \frac{1}{2} \sum_{i=1}^{N} \nabla^2 \phi_i(\mathbf{r}) \tag{2.13}$$

Equations 2.5 - 2.7 are well-known Kohn-Sham equations, with the resulting density $n(\mathbf{r})$ and the total energy E_{KS} given by equations 2.10 and 2.12. These equations have single particle form with the potential that must be found self-consistently with the resulting density.

The above formulae represent the non-spinpolarized Kohn-Sham scheme for electrons in a solid. The spin-density functional formalism is obtained by introducing two spin-densities $n^{\uparrow}(\mathbf{r})$ and $n^{\downarrow}(\mathbf{r})$. They are solutions of the Kohn-Sham equations 2.5 for the same effective potential as above, the only modification occurring in the exchange-correlation part. Now, the

spin-dependent exchange-correlation potential can be written as,

$$V_{xc}^{\sigma}([n^{\uparrow}, n^{\downarrow}; r]) = \frac{\delta E_{xc}[n^{\uparrow}, n^{\downarrow}]}{\delta n^{\sigma}(\mathbf{r})} \tag{2.14}$$

where ($\sigma = \uparrow or \downarrow$) depends on both the spin densities.

The solution of the equation 2.5 requires certain approximations for the exchange and correlation term because they are not known exactly, except for the free (homogeneous) electron gas. The most widely used approximations are the Local Density Approximation (LDA) and the Generalized Gradient Approximation (GGA). Within the LDA, the exchange-correlation energy density per electron is assumed to be the same as that in a homogeneous electron gas [111]

$$E_{xc}^{LDA}[n] = \int d^3 r n(\mathbf{r}) \varepsilon_{xc}^{hom}(n(\mathbf{r})) \tag{2.15}$$

where ε_{xc}^{hom} is the sum of the exchange and correlation energies of the homogeneous electron gas of density $n(\mathbf{r})$. Along with the electron density, GGA [137, 138] includes its local gradient into the exchange-correlation functional

$$E_{xc}^{GGA}[n] = \int d^3 r n(\mathbf{r}) \varepsilon_{xc}^{GGA}(n(\mathbf{r}), |\nabla n|) \tag{2.16}$$

Several different forms for ε_{xc}^{GGA}, the GGA energy density per electron, have been suggested. Moreover, over the past several years, in addition to the GGA functional, other approximations for the exchange and correlation have also been developed [139–145].

Different choices of the basis sets to express the Kohn-Sham orbitals, the solution of equation 2.5, led to the construction of different electronic structure methods. There are three major groups of methodologies practiced now-a-days: the PseudoPotential methods, the Full Potential methods and the Green's function based methods. In this thesis, we have used all three methods. In the next section, we describe these methods briefly.

2.3 Pseudopotential method

In this method, the strong core potential of an atom is replaced by a pseudopotential. It is done in such a way that the ground state wavefunction corresponding to the "Pseudo-Hamiltonian" mimics all electron valance wavefunction outsider a cut-off radius. The construction of the pseudopotentials removes the wiggles in the wave functions of the inert nuclei in the core region, resulting in a continuation of smooth valance wavefunctions there. As a result, the pseudo-wavefunctions can be represented by a reasonable number of plane waves, making the method computationally tractable. In the next subsections, we briefly describe constructions of pseudopotentials and their evolutions.

2.3.1 The Phillips-Kleinman Construction

The pseudopotential approach originated from orthogonalized planewave (OPW) [113, 146] method, where the valance wavefunctions φ_υ are expanded using a basis set containing planewaves that are orthogonalized to the core states φ_c,

$$\phi_{OPW}(\mathbf{k}+\mathbf{G}) = \phi_{PW}(\mathbf{k}+\mathbf{G}) - \sum_{\alpha,c} < \varphi_c|\phi_{PW}(\mathbf{k}+\mathbf{G}) > \varphi_{\alpha,c} \tag{2.17}$$

where ϕ_{PW} is a planewave and ϕ_{OPW} is the OPW and the summation is extended over core states (c) and atom (α). The pseudo states are defined as

$$\varphi_\upsilon^{PS} = \varphi_\upsilon + \sum_{\alpha,c} a_{\upsilon c}\varphi_{\alpha,c} \tag{2.18}$$

with $a_{\upsilon c} =< \varphi_{\alpha,c}|\varphi_\upsilon^{PS} >$

The pseudo states satisfy a Schrödinger like equation with an additional contribution V^R to the Hamiltonian,

$$V^R = \sum_{\alpha,c} a_{\upsilon c}(\varepsilon_\upsilon - \varepsilon_{\alpha,c})|\varphi_{\alpha,c} >< \varphi_{\alpha,c}| \tag{2.19}$$

Adding V^R to the original potential V leads to the Phillips-Kleinman pseudopotential V^{PK}

$$V^{PK} = V + V^R \tag{2.20}$$

Outside the cut-off radius $\mathbf{r}_c$, V^{PK} becomes equal to V since the core wavefunction vanishes.

2.3.2 Norm-Conserving Pseudopotentials (NCPP)

Since the days of Phillips-Klieinman construction, the sophistication and the efficiency of pseudopotentials have been improved to satisfy the following goals: (i) it has to be as soft as possible, (ii) it should be as transferable as possible, (iii) the pseudo-charge density should produce the valance charge density as accurately as possible. The Norm-Conserving PseudoPotentials (NCPP) are pseudopotentials constructed such that the pseudo-wavefunctions are exactly equal to the actual valance wavefunctions outside $\mathbf{r}_c$, whereas inside $\mathbf{r}_c$, the pseudo-wavefunctions differ from the true wavefunctions [147, 148]. However, the norm is being conserved, i.e.,

$$\int_0^{\mathbf{r}_c} dr\, r^2 \varphi^{PS*}(r)\varphi^{PS}(r) = \int_0^{\mathbf{r}_c} dr\, r^2 \varphi^{*}(r)\varphi(r) \tag{2.21}$$

The wavefunctions and eigenvalues are different for different angular momenta, ℓ. Pseudopotentials of these type are often called semi-local. The measure of transferability is provided by logarithmic derivatives at $\mathbf{r}_c$,

$$\frac{1}{\varphi^{PS}(r_c, E)} \frac{d\varphi^{PS}(r_c, E)}{dr} = \frac{1}{\varphi(r_c, E)} \frac{d\varphi(r_c, E)}{dr} \tag{2.22}$$

The equation holds exactly for E equal to the atomic reference energy.

2.3.3 Ultrasoft Pseudopotentials (USPP)

In 1990, Vanderbilt proposed [149–151] a new and radical idea for generating pseudopotentials, which differ significantly from the concept of Norm-conservation. Pseudo-wavefunctions generated in this way, matches to the all-electron wavefunctions outside $\mathbf{r}_c$, as prescribed within norm-conserving pseudopotentials scheme. However, inside $\mathbf{r}_c$ they are allowed to

soften as much as possible. The norm-conserving constraint is removed to accomplish this. Although this introduces some complications, but greatly reduce the number of plane waves required to construct the basis set. The three-fold complications inherent to the construction of ultrasoft pseudopotential are: (i) since the wavefunctions are not necessarily been normalized, they introduce a non-trivial overlap into the secular equation, (ii) the pseudo charge density cannot simply be obtained with just calculating $\sum \varphi^* \varphi$ as done with norm conserving pseudopotentials. Rather, a term need to be added in the core region, (iii) relaxation of the norm conservation results in a less transferable pseudopotentials. Nevertheless, usage of these pseudopotentials over the years in large scale calculations proved their reliability in condensed matter calculations and most importantly, the cost of generating these kinds of pseudopotentials is negligible compared to the cost of calculations where they are used.

2.4 Projector Augmented Wave (PAW) method

The drawback of pseudopotential method is that all the information of the full wave function close to the nuclei is lost. This can influence the calculations of certain properties, such as hyperfine parameters and electric field gradients. The second major disadvantage of this method is that one has a priori no idea of when the approximation yields reliable results in the real material environment. A more general approach is the Projector Augmented Wave (PAW) method, introduced by Blöchl in 1994 [152], as an extension of both Augmented Plane Wave (APW) [114–116] and pseudopotential methods. PAW method is categorized in a class of "all-electron" methods, in which the full information about the wavefunction is available. The basic idea of the PAW method is to divide the wavefunction into two parts: a partial wave expansion within an atom centered sphere, and an envelope function outside. The two parts are then matched smoothly at the sphere edge. In this section, we present a brief description of this formalism.

We first introduce a linear transformation $\hat{\mathcal{T}}$ which maps computationally convenient smooth wavefunctions $|\tilde{\psi}>$ to the physically relevant all-electron wavefunctions $|\psi>$

$$|\psi_n> = \hat{\mathcal{T}}|\tilde{\psi}_n> \tag{2.23}$$

where n is a quantum state label, consisting of band index, spin and **k**-vector index. The ground state smooth wave function is then obtained by solving the Kohn-Sham equations

$$\hat{\mathcal{T}}^{\dagger}\hat{\mathcal{H}}\hat{\mathcal{T}}|\tilde{\psi}_n>=\epsilon_n\hat{\mathcal{T}}^{\dagger}\hat{\mathcal{T}} \tag{2.24}$$

Since the true wave functions are already smooth at a certain distance from the core, which requires that the transformation must be unitary beyond the augmentation cut-off and a sum of atom-centered contributions inside

$$\hat{\mathcal{T}} = 1 + \sum_a \hat{\mathcal{T}}^a \tag{2.25}$$

where a is an atom index and $\hat{\mathcal{T}}^a = \hat{\mathcal{T}}^a(\mathbf{r} - \mathbf{R}^a) = 0$ for $|\mathbf{r} - \mathbf{R}^a| > r_c^a$. The cut-off radii r_c^a is chosen such that there is no overlap between augmentation spheres. Within the augmentation region, the smooth wavefunction can be expanded into smooth partial waves $\tilde{\phi}^a$

$$|\tilde{\psi}_n>=\sum_{ia} c_{ni}^a|\tilde{\phi}_i^a> \tag{2.26}$$

Similarly the all-electron counterpart can be written as

$$|\psi_n>=\sum_{ia} c_{ni}^a|\phi_i^a> \tag{2.27}$$

Now, the transformation can be fully expressed in terms of partial waves

$$|\phi_i^a>=(1+\hat{\mathcal{T}}^a)|\tilde{\phi}_i^a> \Longrightarrow \hat{\mathcal{T}}^a|\tilde{\phi}_i^a>=|\phi_i^a>-|\tilde{\phi}_i^a> \tag{2.28}$$

Hence the true wavefunction are expressed as

$$|\psi_n>=|\tilde{\psi}_n>-\sum_{ia} c_{ni}^a|\tilde{\phi}_i^a>+\sum_{ia} c_{ni}^a|\phi_i^a> \tag{2.29}$$

where the expansion coefficients are need to be determined. Since the transformation operator $\mathcal{T}$ is linear, the coefficients must be linear functionals of the smooth wavefunction

$$c_{ni}^a =< \tilde{p}_i^a|\tilde{\psi}_n >\equiv \mathcal{P}_{ni}^a \tag{2.30}$$

where $\tilde{p}_i^a$ are some smooth projector functions. The non-overlapping condition of the augmented spheres forces the one-center expansion of smooth wavefunctions $\sum_i < \tilde{p}_i^a|\tilde{\psi}_n > |\tilde{\phi}_i^a >$ to be identical with $|\tilde{\phi}_i^a >$. This is equivalent to the completeness relation

$$\sum_i |\tilde{\phi}_i^a >< \tilde{p}_i^a| = 1 \tag{2.31}$$

which in turn implies that

$$< \hat{p}_{i_1}^a|\hat{\phi}_{i_2}^a >= \delta_{i_1,i_2} \tag{2.32}$$

i.e. smooth projector functions and partial waves are mutually orthonormal within the augmentation sphere. Using equations 2.29 and 2.30, we obtain a closed form for the transformation operator

$$\hat{\mathcal{T}} = \sum_a \sum_i (|\phi_i^a > -|\tilde{\phi}_i^a >) < \tilde{p}_i^a| \tag{2.33}$$

which allows us to get the true, all-electron, Kohn-Sham wavefunction $\psi_n(\mathbf{r})= \langle \mathbf{r} \mid \psi_n \rangle$

$$\psi_n(\mathbf{r}) = \tilde{\psi}_n(\mathbf{r}) + \sum_a \sum_i (\phi_i^a(\mathbf{r}) - \tilde{\phi}_i^a(\mathbf{r})) < \tilde{p}_i^a|\tilde{\psi}_n > \tag{2.34}$$

It is generally convenient to introduce the one center expansions

$$\psi_n^a(\mathbf{r}) = \sum_i \psi_i^a(\mathbf{r}) < \tilde{p}_i^a|\phi_n > \tag{2.35}$$

$$\tilde{\psi}_n^a(\mathbf{r}) = \sum_i \tilde{\psi}_i^a(\mathbf{r}) < \tilde{p}_i^a|\phi_n > \tag{2.36}$$

which enable us to express the true wavefunction in a compact form as,

$$\psi_n(\mathbf{r}) = \tilde{\psi}_n(\mathbf{r}) + \sum_a (\psi_n^a(\mathbf{r}) - \tilde{\psi}_n^a(\mathbf{r})) \tag{2.37}$$

explicitly separating the extended-space and the atom-centered contributions.

The above expression is often exploited to obtain compact expression for various quantities in PAW method. The first term can be evaluated on an extended grid, or on a soft basis

set, while the last two terms are evaluated on fine radial grids.

2.5 Linearized Augmented Plane Wave (LAPW) method

The Linearized Augmented Plane Wave (LAPW) method originally is a modification to the Augmented Plane Wave (APW) [114–116] method. In APW method, the space is divided into two regions and two different sets of basis functions are used: radial solutions of Schrodinger's equation inside non-overlapping muffin-tin spheres centered on atoms and plane waves in the remaining interstitial regions

$$\varphi(\mathbf{r}) = \begin{cases} \Omega^{-1/2} \sum_{\mathbf{G}} c_{\mathbf{G}} e^{i(\mathbf{G}+\mathbf{k}).\mathbf{r}} & \mathbf{r} \in I \\ \sum_{\ell m} A_{\ell m} u_\ell(r) Y_{\ell m}(\hat{\mathbf{r}}) & \mathbf{r} \in S \end{cases} \tag{2.38}$$

where φ is a wavefunction, Ω is the unit cell volume and u_ℓ is the regular solution of

$$\left\{ -\frac{d^2}{dr^2} + \frac{\ell(\ell+1)}{r^2} + V(r) - E_\ell \right\} r u_\ell(r) = 0 \tag{2.39}$$

Here, $c_{\mathbf{G}}$ and $A_{\ell m}$ are expansion coefficients, E_ℓ is a parameter and V is the spherical component of the potential inside the sphere. The coefficients are related with the following matching condition at the boundary of muffin-tin sphere R,

$$A_{\ell m} = \frac{4\pi i^\ell}{\Omega^{1/2} u_\ell(R)} \sum_{\mathbf{G}} c_{\mathbf{G}} j_\ell(|\mathbf{k}+\mathbf{G}|R) Y^*_{\ell m}(\mathbf{k}+\mathbf{G}) \tag{2.40}$$

The APWs lack variational freedom to allow for changes in the wavefunctions as the band energy deviates from the reference energy E_ℓ. This means that, at a fixed $\mathbf{k}$-point, band energies cannot be obtained from a single diagonalization. Rather, one needs to solve the secular determinant as a function of energy and the determinant is recalculated for a range of energies to locate the roots. This traditional search for the APW eigenvalues is cumbersome and computationally very demanding. Another difficulty involved with APW method is that it is very hard to extend this formalism to incorporate general crystal potentials. Within this potential correction, known as non muffin-tin correction or non spherical correction, the muffin-tin potential has been complemented with a non-spherical part inside the artificial sphere. However,

in a non-spherical potential the different orbitals experience different effective potentials. This differs from the idea of spherical average that is used to determine the radial functions. Therefore, the radial functions no longer represent the exact solutions inside the sphere, whereas the potential correction does not affect the choice of basis functions in the interstitials. The task of finding APW eigenvalues becomes somewhat more troublesome due to asymptotic problem. During the process of finding energy eigenvalues, one might encounter some energies for which $u_\ell(\mathbf{r})$ becomes very small or even equal to zero at the muffin-tin sphere boundary. Inserting this in the evaluation of the APW matching condition (equation 2.40), yields a very large or infinite $A_{\ell m}$, and thus the plane waves and the radial functions decouple at muffin-tin boundary.

O. K. Andersen proposed a method in which the plane waves and their derivatives are made continuous by matching to the radial functions at fixed E_ℓ plus its derivatives with respect to E_ℓ [117]. This choice of functions as the basis set circumvents the problems arising from APW method, and provides a flexible and accurate way to the band structure calculation. This is known as the LAPW basis set.

In the interstitial region, LAPW basis functions have the identical form with the APW basis functions. Inside the muffin-tin sphere, the APW augmentation has been replaced by u_ℓ and its energy derivatives $\dot{u}_\ell$, evaluated at fixed linearization energy E_ℓ

$$\varphi(\mathbf{r}) = \begin{cases} \Omega^{-1/2} \sum_{\mathbf{G}} c_{\mathbf{G}} e^{i(\mathbf{G}+\mathbf{k}).\mathbf{r}} & \mathbf{r} \in I \\ \sum_{\ell m} [A_{\ell m} u_\ell(r) + B_{\ell m} \dot{u}_\ell(r)] Y_{\ell m}(\hat{\mathbf{r}}) & \mathbf{r} \in S \end{cases} \tag{2.41}$$

where $B_{\ell m}$ are the co-efficients for the energy derivatives analogous to $A_{\ell m}$. Inside the sphere, the LAPWs have more variational freedom than APWs. This is due to the fact that, if E_ℓ differs slightly from the band energy, ε, a linear combination would produce the APW radial function constructed at band energy

$$u_\ell(\varepsilon, r) = u_\ell(E_\ell, r) + (\varepsilon - E_\ell)\dot{u}_\ell(\varepsilon, r) + O((\varepsilon - E_\ell))^2 \tag{2.42}$$

The energy derivatives $\dot{u}_\ell$ satisfies,

$$\left\{ -\frac{d^2}{dr^2} + \frac{\ell(\ell+1)}{r^2} + V(r) - E_\ell \right\} r\dot{u}_\ell(r) = r u_\ell(r) \tag{2.43}$$

This method introduces errors of order $(\varepsilon - E_\ell)^2$ in the wavefunctions and $(\varepsilon - E_\ell)^4$ in the band energies. Because of the higher order of the errors, the LAPWs form a good basis set over a relatively large energy regions, such that all the valance band may be typically treated within a single set of E_ℓ. Moreover, in this method, at a given **k**-point, the energy bands are obtained with a single diagonalization.

2.6 Korringa, Kohn and Rostoker (KKR) Green's Function method

In 1947 Korringa [118] and in 1954 Kohn and Rostoker [119] independently proposed a Green's function based method for solving the electronic structure [153]. The method is based upon multiple scattering formalism and thus can be easily combined with techniques for performing configurational averaging in disordered systems. The most important features of these KKR Green's function based formalism are that it separates the structural part from the potential part, and Green's functions provide a natural approach to a localized description of electronic properties that can be adapted to alloys and other disordered systems.

Suppose that the system is composed of an assembly of non-overlapping spherical muffin-tin potentials centered on each lattice site of a crystal. Then, the crystal Green's function $G(\mathbf{r}, \mathbf{r}'; E)$ can be evaluated from the free space Green's function $g(\mathbf{r}, \mathbf{r}'; E)$ by

$$G(\mathbf{r}, \mathbf{r}'; E) = g(\mathbf{r}, \mathbf{r}'; E) + \int dr'' \, g(\mathbf{r}, \mathbf{r}''; E) V(\mathbf{r}'') G(\mathbf{r}'', \mathbf{r}'; E) \tag{2.44}$$

where $V(\mathbf{r}')$ denotes the assembly of muffin-tin potentials. In reality, the above equation can not be used for calculations because of convergence problem. Instead, a cell-centered angular momentum based representation is introduced. Let's first consider the cell-centered representation of $g(\mathbf{r}, \mathbf{r}'; E)$

$$g(\mathbf{r} + \mathbf{R_m}, \mathbf{r}' + \mathbf{R_n}; E) = g(\mathbf{r}, \mathbf{r}' + \mathbf{R_n} - \mathbf{R_m}; E) = -i\sqrt{E} \sum_L J_L(\mathbf{r}) H_L(\mathbf{r}' + \mathbf{R_n} - \mathbf{R_m}) \tag{2.45}$$

where H_Ls are the Hankel functions. Using the addition theorem of Hankel functions,

$$H_L(\mathbf{r}' + \mathbf{R_n} - \mathbf{R_m}; E) = \frac{i}{\sqrt{E}} \sum_{L'} g^{mn}_{LL'}(E) J_{L'}(\mathbf{r}; E) \tag{2.46}$$

and utilizing the following abbreviations

$$\begin{aligned} J_L(\mathbf{r}; E) &= j_\ell(\sqrt{E}r) Y_L(\mathbf{r}) \\ H_L(\mathbf{r}; E) &= h_\ell(\sqrt{E}r) Y_L(\mathbf{r}) \end{aligned} \tag{2.47}$$

the free electron Green's function can be expressed as

$$\begin{aligned} g(\mathbf{r} + \mathbf{R_m}, \mathbf{r}' + \mathbf{R_n}; E) &= -i\sqrt{E}\delta_{mn} \textstyle\sum_L J_L(r_<; E) H_L(r_>; E) \\ &+ \textstyle\sum_{LL'} J_L(\mathbf{r}; E) g^{mn}_{LL'} J_L(\mathbf{r}'; E) \end{aligned} \tag{2.48}$$

The structure constants are defined by

$$g^{mn}_{LL'}(E) = -4\pi i \sqrt{E}(1 - \delta_{mn}) \sum_{L''} i^{\ell - \ell' + \ell''} C^{L''}_{LL'} H_{L''}(R_m - R_n; E) \tag{2.49}$$

with the Gaunt coefficients

$$C^{L''}_{LL'} = \int d\Omega Y_{L''}(\mathbf{r}) Y_{L'}(\mathbf{r}) Y_L(\mathbf{r}) \tag{2.50}$$

Similarly, the crystal Green's function has the cell-centered representation as follows,

$$\begin{aligned} G(\mathbf{r} + \mathbf{R_m}, \mathbf{r}' + \mathbf{R_n}; E) &= -i\sqrt{E}\delta_{mn} \textstyle\sum_L \mathcal{J}_L(r_<; E) \mathcal{H}_L(r_>; E) \\ &+ \textstyle\sum_{LL'} \mathcal{J}_L(\mathbf{r}; E) G^{mn}_{LL'} \mathcal{J}_L(\mathbf{r}'; E) \end{aligned} \tag{2.51}$$

with

$$\begin{aligned} \mathcal{J}_L(\mathbf{r}; E) &= P_\ell(\sqrt{E}r) Y_L(\mathbf{r}) \\ \mathcal{H}_L(\mathbf{r}; E) &= Q_\ell(\sqrt{E}r) Y_L(\mathbf{r}) \end{aligned} \tag{2.52}$$

The second term, in equation 2.48, represents the contribution of the multiple scattering or back scattering to the Green's function and produces the band structure. The relation between $G^{mn}_{LL'}(E)$ and $g^{mn}_{LL'}(E)$ can be obtained by inserting the above expressions for the Green's

function into the integral equation

$$G^{mn}_{LL'}(E) = g^{mn}_{LL'}(E) + \sum_{L''m,} g^{mm'}_{LL'}(E) t^{m'}_{L''} G^{m'n}_{L''L'}(E) \tag{2.53}$$

where t-matrix $t^{m'}_{L''}$ is defined as

$$t^{m'}_{L''} = \int\int d\mathbf{r_m} d\mathbf{r}'_{\mathbf{m}} J_L(\mathbf{r}_{m'}; E) t^{m'}(\mathbf{r}_{m'}, \mathbf{r}'_{m'}; E) J_{L'}(\mathbf{r}'_{m'}; E) \tag{2.54}$$

When the scattering centers are aligned periodically in the crystal, $G^{mn}_{LL'}$ and $g^{mn}_{LL'}$ can be Fourier transformed as,

$$G^{mn}_{LL'}(\mathbf{R}_m - \mathbf{R}_n; E) = \frac{1}{\tau}\int_\tau G_{LL'}(\mathbf{k}, E) e^{i\mathbf{k}(\mathbf{R_m}-\mathbf{R_n})} d\mathbf{k} \tag{2.55}$$

$$g^{mn}_{LL'}(\mathbf{R}_m - \mathbf{R}_n; E) = \frac{1}{\tau}\int_\tau g_{LL'}(\mathbf{k}, E) e^{i\mathbf{k}(\mathbf{R_m}-\mathbf{R_n})} d\mathbf{k} \tag{2.56}$$

where τ is the volume of the first Brillouin zone. Substituting them into equation 2.53, one gets

$$G_{LL'}(\mathbf{k}, E) = g_{LL'}(\mathbf{k}, E) + \sum_{L''} g_{LL'}(\mathbf{k}, E) t_{L''} G_{L''L'}(\mathbf{k}, E) \tag{2.57}$$

Finally,

$$G_{LL'}(\mathbf{k}, E) = \sum_{L''} [\delta_{L''L} - g_{L''L}(\mathbf{k}, E) t_L] g_{L''L}(\mathbf{k}, E) \tag{2.58}$$

Then, the crystal Green's function is given by

$$\begin{aligned} &G(\mathbf{r} + \mathbf{R_m}, \mathbf{r}' + \mathbf{R_n}; E) = -i\sqrt{E}\delta_{mn} \textstyle\sum_L \mathcal{J}_L(r_<; E)\mathcal{H}_L(r_>; E) \\ &+\mathcal{J}_{Lm}(\mathbf{r}) \textstyle\int \frac{d\mathbf{k}}{\tau} exp(i\mathbf{k}.(\mathbf{R_m} - \mathbf{R_n})) \sum_{L''} g_{LL''}(\mathbf{k}, E)[1 - tg(\mathbf{k}, E)]^{-1}_{L''L'} \mathcal{J}_{L'n}(\mathbf{r}') \end{aligned} \tag{2.59}$$

The band structure is then calculated by finding the zeros of the determinant of the matrix appearing in equation 2.58 for each $\mathbf{k}$

$$det|\delta_{LL'} - t_L(E) g_{LL'}(\mathbf{k}; E)| = 0 \tag{2.60}$$

The procedure determines the energy eigenvalues as a function of **k** and hence, yields an energy dispersion relation $E(\mathbf{k})$. The zeros of the KKR matrix gives the poles of the Green's function; each pole corresponds to the eigenstate of the Hamiltonian.

2.7 Exact Muffin-Tin orbital (EMTO) method

The EMTO method is another Green's function based method for calculating electronic structures of materials [154–158]. It improves accuracies of calculated quantities to the degree at per with the Full-Potential (FP) methods like LAPW and removes the demerits of other similar methods based upon Atomic Sphere Approximation (ASA) [159, 160].

In this method, the space consists of overlapping muffin-tin spheres. Within the overlapping muffin-tin approximation, the effective single-electron potential is approximated by spherical potential wells $v_R(r_R) - v_0$ centered on lattice sites R plus a constant potential v_0, i.e.,

$$v(\mathbf{r}) \approx v_{mt}(\mathbf{r}) \equiv v_0 + \sum_R [v_R(r_R) - v_0] \tag{2.61}$$

By definition, $v_R(r_R)$ becomes equal to v_0 outside the potential sphere of radius s_R. For fixed potential spheres, $v_R(r_R)$ and v_0 are determined from the following functional,

$$F_v[\{v_R\}, v_0] \equiv \int v(\mathbf{r}) - v_0 - \sum_R [v_R(r_R) - v_0] d\mathbf{r} \tag{2.62}$$

Then, the minimization condition can be expressed as

$$\int_\Omega \frac{\delta F_v[\{v_R\}, v_0]}{\delta v_R(r)} d\mathbf{r} = 0 \tag{2.63}$$

and

$$\frac{\partial F_v[\{v_R\}, v_0]}{\partial v_0} = 0 \tag{2.64}$$

Here Ω is the unit cell volume. The solutions of integro-differential equations 2.63 and 2.64 give the optimal $v_R(r_R)$ and v_0 and the procedure is known as Optimized Overlapping Muffin-Tin (OOMT) potential method.

In the EMTO formalism, the single-electron Schrödinger-like equations are solved separately within the units defined around each lattice sites. The calculation of effective single-electron potential involves integrations over the real space which are carried out using Spherical Cell Approximation (SCA) [158] technique.

In this method, Schrödinger-like single-particle Kohm-Sham equation can be solved by expanding the Kohn-Sham orbital in terms of exact muffin-tin orbitals $\bar{\psi}^a_{RL}(\epsilon_i, \mathbf{r}_R)$, i.e.,

$$\phi_i(\mathbf{r}) = \sum_{RL} \bar{\psi}^a_{RL}(\epsilon_i, \mathbf{r}_R) v^a_{RL,i} \tag{2.65}$$

The expansion coefficients, $v^a_{RL,i}$ are determined from the condition that the above expansion should be solution to the equation 2.5 in the entire space. In the interstitial region, where the potential is approximated by v_0, the basis functions can be described as the solutions of the wave equation,

$$\{\nabla^2 + \kappa^2\}\psi^a_{RL}(\kappa^2, r_R) = 0 \tag{2.66}$$

where $\kappa^2 = \epsilon - v_0$, and ϵ is the energy. The functions $\psi^a_{RL}(\kappa^2, r_R)$, referred to as the screened spherical waves [155], can be expanded in terms of real harmonics $Y_{L'}(\hat{\mathrm{r}}_{R'})$ around any site R' as

$$\psi^a_{RL}(\kappa^2, \bar{r}_R) = f^a_{R\ell}(\kappa^2, r_R) Y_L(\hat{r}_R)\delta_{RR'}\delta_{LL'} + \sum_{L'} g_{R'\ell'}(\kappa^2, r_{R'}) Y_{L'}(\hat{r}_R) S_{R'L'RL}(\kappa^2) \tag{2.67}$$

the expansion coefficients $S_{R'L'RL}(\kappa^2)$ are the elements of slope matrix, and $f^a_{R\ell}(\kappa^2, r_R)$ and $g_{R'\ell'}(\kappa^2, r_{R'})$ are the head and tail function, respectively.

Inside the potential sphere, the basis set is represented by partial waves $\phi^a_{RL}(\epsilon, \mathbf{r}_R)$

$$\phi^a_{RL}(\epsilon, \mathbf{r}_R) = N^a_{R\ell}(\epsilon)\phi_{R\ell}(\epsilon, r_R) Y_L(\hat{r}_R) \tag{2.68}$$

where $N^a_{R\ell}(\epsilon)$ is the normalization function. The functions $\phi^a_{RL}(\epsilon, \mathbf{r}_R)$ are the solutions of the radial Schrödinger equation

$$\frac{\delta(r_R\phi_{RL}(\epsilon, r_R))}{\delta^2_R} = \left(\frac{\ell(\ell+1)}{r^2_R} + v_R(r_R) - \epsilon\right) r_R\phi_{RL}(\epsilon, r_R) \tag{2.69}$$

To match the functions together smoothly, auxiliary free electron solutions φ^a_{RL} are introduced in the region between the two spheres,

$$\varphi^a_{RL}(\epsilon, r_R) = f^a_{R\ell}(\kappa^2, r_R) + g^a_{R\ell}(\kappa^2, r_R) D_{R\ell}(\epsilon) \tag{2.70}$$

where $D_{R\ell}(\epsilon)$ is the logarithmic derivatives of $\varphi^a_{RL}(\epsilon, a_R)$ calculated at $r_a = a_R$. Finally, the exact muffin-tin orbitals are constructed as the superposition of the screened spherical waves, the partial waves and the free-electron solution, i.e.

$$\bar{\psi}^a_{RL} = \psi^a_{RL}(\kappa^2, \mathbf{r}_R) + N^a_{R\ell}(\varepsilon)\phi_{R\ell}(\varepsilon, r_R) Y_L(\hat{r}_R) - \varphi^a_{R\ell}(\epsilon, r_R) Y_L(\hat{r}_R) \tag{2.71}$$

With the exact muffin-tin orbitals defined in equation 2.71, the trial wave function 2.65 around site R can be expressed as

$$\begin{aligned} \phi(\mathbf{r}_R) = {} & \textstyle\sum_L N^a_{R\ell}(\epsilon)\phi_{R\ell}(\epsilon, r_R) Y_L(\hat{r}_R) v^a_{RL} + \sum_L g^a_{R\ell}(\kappa^2, r_R) Y_L(\hat{r}_R) \\ & \times \textstyle\sum_{R'L'} \left[S_{RLR'L'}(\kappa^2) - \delta_{R'R}\delta_{L'L} D^a_{R\ell}(\epsilon) \right] v^a_{R'L'} \end{aligned} \tag{2.72}$$

The trial function will be a solution of equation 2.5 for the muffin-tin potential 2.61 inside the potential sphere for $\ell \leq \ell_{max}$. A so-called "kink cancelation equation", equivalent to the KKR secular equation must hold,

$$\sum_{RL} a_{R'} \left[S^a_{R'L'RL}(\kappa^2_j) - \delta_{R'R}\delta_{L'L} D^a_{R\ell}(\epsilon_j) \right] v^a_{RL,j} = 0 \tag{2.73}$$

The difference between the slope matrix and the logarithmic derivative matrix is called the kink matrix,

$$K^a_{R'L'RL}(\epsilon_j) = a_{R'} S^a_{R'L'RL}(\kappa^2_j) - \delta_{R'R}\delta_{L'L} a_R D^a_{R\ell}(\epsilon_j) \tag{2.74}$$

The solutions of equation 2.73 are the single electron energies and wave functions. These solutions can be obtained from the poles of the path operator $g_{R''L''RL}$ defined for a complex energy z by

$$\sum_{R''L''} K^a_{R'L'R''L''}(z) g^a_{R''L''RL}(z) = \delta_{R'R}\delta_{L'L} \tag{2.75}$$

Total energy is calculated from the total charge density utilizing the Full Charge Density

(FCD) technique [161–163]. The EMTO-FCD total energy is separated into the kinetic energy, the exchange-correlation energy and the electrostatic energy. Furthermore, the latter is divided into the intra-cell and inter-cell contributions. Then, the total energy becomes,

$$E_{tot} = T_s[n] + \sum_R \left(F^R_{intra}[n_R] + E^R_{xc}[n_R] \right) + F_{inter}[n_R] \tag{2.76}$$

where the intra-cell $F^R_{intra}[n_R]$ and exchange-correlation energies $E^R_{xc}[n_R]$ depend only on the charge density within the actual cell, whereas $F_{inter}[n_R]$ depends on the charge distributions around different cells and $T_s[n]$ is a nonlocal functional of the density.

2.8 Modeling of the chemical or substitutional disorder

The calculations of desired properties using first-principles electronic structure methods are straightforward in periodic ordered materials. However, computation of those properties in low symmetry materials, such as random alloys, creates enormous problems. Particularly, the faithful representation of the randomness (disorder) in these alloys poses significant challenges to computational scientists. Ideally, the proper description of the random (disordered) alloys on a randomly generated impurity distribution requires large supercells, which render standard electronic structure methods unfeasible [164]. Therefore, to simulate the accurate random environment of disordered Mn_2NiX materials through periodic structure Coherent Potential Approximation (CPA) and Special Quasirandom Structure (SQS) methods have been used in this doctoral work.

2.8.1 Coherent Potential Approximation (CPA)

In condensed matter calculations, Coherent Potential Approximation (CPA) scheme has been in wide use to simulate the disordered environments in solids. The method was introduced simultaneously by Soven [165] in connection with disordered electronic systems and Taylor [166] in connection with the lattice dynamics of mass disordered alloys in 1967. Numerous applications over the years like calculations of lattice parameters, elastic constants, mixing enthalpy, etc., with an accuracy similar to the ordered systems, has proven the capability of CPA method as state-of-the-art technique for electronic structure calculations in disordered

alloys. The main approximation is that the disordered alloy may be replaced by an ordered effective medium, the parameters of which are determined self-consistently. The impurity problem is treated within the single-site approximation. This means that one single impurity is embedded in an effective medium and no information about the individual potential and charge density beyond the sphere or polyhedra around this impurity is provided. Let us consider a substitutional alloy $A_aB_bC_c$, . . . , where the atoms A, B, C, . . . are randomly distributed among lattice sites. Here, a, b, c . . . are the atomic fractions of the A, B, C, . . . atoms, respectively. The Green's function g and the alloy potential P_{alloy} are used to describe the above system. In a real alloy, due to the disorder in the environment, the alloy potential varies even around the same type of atoms. There are two important approximations within the CPA. First, it assumes that the local potentials around a certain type of atom from the alloy are the same, i.e., the effect of the local environment is neglected. These local potentials are described by the potential functions P_A, P_B, P_C, ... Second, the system is replaced by a monatomic set-up described by the site independent coherent potential $\tilde{P}$. In terms of Green's functions, the real Green's function g is approximated by the coherent Green's function $\tilde{g}$. For each alloy component i = A, B, C, . . . a single-site Green's function g_i is introduced. The main steps to construct the CPA effective medium are as follows. First, the coherent Green's function is calculated from the coherent potential with an electronic structure method.

$$\tilde{g} = \left[S - \tilde{P}\right]^{-1} \tag{2.77}$$

here S denotes the structure constant matrix corresponding to the underlying lattice. Next, the Green's functions of the alloy components g_is are determined by substituting the coherent potential of the CPA medium by the real atomic potential P_i, which is given by

$$g_i = \tilde{g} + \tilde{g}\left(P_i - \tilde{P}\right) g_i; i = A, B, C \tag{2.78}$$

Finally, the average of the individual Green's functions should reproduce the single-site part of the coherent Green's functions, i.e.,

$$\tilde{g} = ag_A + bg_B + cg_C + ... \tag{2.79}$$

The above three equations are solved iteratively, and the output $\tilde{g}$ and g_i's are used to determine the electronic structure, charge density and total energy of random alloys.

2.8.2 Special Quasirandom Structure (SQS)

The basic idea in developing SQS is to mimic the actual local random environment of alloys without generating large supercells and multiple supercell configurations. SQS generates a small periodic structure with target composition that best satisfies pair and multi-site correlation functions corresponding to a random alloy up to a certain distance [164]. Upon relaxation, the atoms in the structure are displaced away from their equilibrium position, creating a distribution of local environments that can be considered as representation of randomness in the original alloys. The theory of SQS has been developed based upon the assumption that the electronic interactions in the given alloys have short range character [164, 167–169].

From statistical point of view, an N-atom per unit cell periodic alloy of random environment is characterized by multi-site correlation functions $\prod_{k,m}$. Here (k, m) corresponds to the figure defined by the number of k atoms located on its vertices (k= 1, 2, 3. pairs, triangle, tetrahedral etc.), while m being the order of nearest-neighbor distance separating them (m= 1, 2 are first, second neighbors etc.). The correlation functions are averages of the products of site occupations (σ_k= ±1 for binary alloys and ±1, 0 for ternary alloys) of figure k at a distance m [167]. The optimum SQS for a given configurations are obtained when the following relation is satisfied

$$\left(\prod_{k,m}\right)_{SQS} = \left\langle \prod_{k,m} \right\rangle_R \tag{2.80}$$

Where $< \prod_{k,m} >_R$ is the ensemble-averaged correlation function of random alloy.

The structure generated by SQS method has been used successfully in the investigation of equilibrium volumes, densities of states, band gaps [167–169], etc. The method gives better results to those properties which depend on local atomic arrangements, such as formation and mixing enthalpies, charge transfer, optical properties and local lattice relaxations [164, 170–175]. The main advantage of this method over conventional supercell method is that the former utilizes the knowledge of multi-pair correlation functions to decide the position of an atom in the cell, while the latter randomly places the atoms in the cell. Thus, SQS provides a better picture of an actual random alloy [175].

2.9 Summary

In this chapter, we have briefly discussed the state-of-the-art computational techniques used in condensed matter physics, i.e., DFT based methods, to retrieve useful information from the materials I have investigated. Four different implementations of DFT, (i) Plane Wave PseudoPotential method, (ii) Full-Potential LAPW method, (iii) Full Potential Korringa Kohn Rostoker (FP-KKR) method and (iv) Exact Muffin Tin Orbital (EMTO) method, are used in this dissertation. The usage of a particular method depends on the nature of the problem. Based upon the fact that core electrons remain inert during chemical reactions, within pseudopotential approximation, wiggles in the core wavefunctions are replaced by a smooth continuation from valance wavefunctions, which reduce the computational cost immensely. More accurate representation of the crystal potential (wavefunction) were done in Full Potential based methods. In FP-LAPW method, the original crystal potential is divided into two regions, inside and outside of the Muffin-Tin spheres. The solution from these two regions are matched smoothly at the boundary of the Muffin-Tin spheres. The most important feature that makes Green's based formalism an efficient tool to calculate the disorder related properties is that they can be seamlessly integrated to the methods for computing configurations averaged quantities, a must for systems with substitutional disorder. The Extensively used method to address the chemical and magnetic disorder is CPA. Within their current implementations, FP-KKR and EMTO methods include CPA to investigate the effects of disorder, whereas pseudopotential and FP-LAPW methods modeled disordered environment with the construction of large and artificial supercells, which can be sometimes prohibitively large.

Chapter 3

Electronic structure, phase stability and possibilities of shape memory behavior in Mn_2NiX alloys* †

3.1 Introduction

Since the pioneering work of Webster *et al.* [60] there has been enormous interest in the magnetic shape memory alloys (MSMA) which undergo from the magnetic high-temperature cubic (austenite) phase to variants of tetragonally distorted phases, and show an extremely large strain in a small external field. This property has made these systems realizable as smart magnetic actuators and sensors. In spite of large magnetic field-induced strain observed in Ni_2MnGa, there are serious shortcomings in Ni_2MnGa and other materials in the Ni_2MnX series as described in chapter 1. Subsequently, the quest for new shape memory materials with desired properties led to the discovery of Mn_2NiX materials. Till now, research on full stoichiometric Mn_2NiX is rather limited. Results of first-principles theoretical calculations in these systems have started to come up only recently [108, 176–180]. However, the information obtained from such calculations are rather scattered and no systematic analysis on the trends in the structural and magnetic properties in these systems based upon their electronic

*Contents of this chapter are mostly taken from Ref. [176, 177].
†Permission from the publishers have been obtained for reprints of Ref. [176, 177].

structures is available. Such an investigation is necessary for two reasons: first, to check the usefulness's of the alloys in the series for magnetic shape memory applications, i.e., whether martensitic transformation can be realized around room temperature and the other key parameters like the magnetizations are substantial, and second, the trends, if any, with regard to their properties related to magnetic shape memory effects would throw enough light to understand the physics of these materials and subsequently help in tailoring their properties to make them functional. For example, in case of Ni_2MnX alloys, it is suggested [181, 182] that the martensitic transformation temperature is correlated with (e/a). This study will explore whether such type of correlations exists in this alloy series.

In this chapter, we present results on our systematic investigations of Mn_2NiAl, Mn_2NiGa, Mn_2NiIn and Mn_2NiSn alloys by first-principles density functional theory [109, 111] based calculations. Comparisons of their energetics related to the martensitic phase transformations, magnetic properties and details related to the electronic structures have been carried out. Role of different sp elements influencing the properties of the alloys has been thoroughly explored. Such a detailed study enables us to understand the microscopic physics of these systems and provide us with the necessary information regarding the viability of these systems as MSM applications. The chapter is organized as follows: details of computations are given in section 3.2 followed by the results and detailed discussions in section 3.3. Concluding remarks are presented in section 3.4.

3.2 Computational Details

The crystal structure of Mn_2NiX materials considered in this chapter and in the rest of the thesis is inverse Heusler with atomic arrangements as described in F 1.4. The electronic structure has been calculated using a full potential linearized augmented plane wave (FP-LAPW) method implementation in E code [183–185]. From careful convergence test with respect to Brillouin zone (BZ) sampling and the size of the basis set, we have determined that the plane wave cut-off for the basis set being $R_{MT}K_{max}= 9$, where R_{MT} is the muffin-tin radius and K_{max} is the largest reciprocal lattice vector, which leads to nearly 350 plane waves. The charge density cut-off was considered to be $G_{max}= 14$ and the angular momentum cut-off to the augmented plane wave was taken to be $\ell_{max}= 10$. The Brillouin zone (BZ) integrations were carried out with 12×12×12 **k**-mesh for the cubic phase and with 17×17×17 **k**-mesh

for the tetragonal phase, which effectively lead to 364 and 693 **k**-points in the cubic and tetragonal phase, respectively in the irreducible Brillouin zone (IBZ). Generalized Gradient Approximation (GGA) with Perdew-Burke-Ernzerhof (PBE) [186] parametrization was used for the exchange-correlation part of the Hamiltonian. For comparison of the lattice constants and total moments, calculations with two Plane wave Pseudopotential (PW-PP) methods- the UltraSoft Pseudopotential (USPP) as implemented in Q E [187] code and the PAW pseudopotential based method as implemented in V A - S P (VASP) [188–190] are done. In case of calculations with USPP, the Ultrasoft pseudopotentials [191] with nonlinear core corrections [192] were generated. Perdew-Wang (PW-91) generalized gradient approximation (GGA) functionals [193] were used for the exchange-correlation part of the Hamiltonian in this case. For calculations with PAW pseudopotentials, PBE [186] parametrization of the GGA exchange-correlation functional was used. In case of USPP based calculations, plane wave with energies up to 810 eV were used in order to describe the electronic wave functions; for calculations with PAW-PP it was 450 eV. For both the methods, the Brillouin zone integrations were performed with 15×15×15 **k**-mesh for the cubic phase, which effectively turns out to be 688 **k**-points in the irreducible Brillouin Zone (IBZ). Choices of the parameters ensured convergence in total energies to less than 1 meV per atom for all the three methods. For further comparison, calculations with two different Green's functions methods, the KKR method as implemented in the S -P R K -K -R (SPR-KKR) code [194, 195] and the EMTO method [173, 196] were done. In both the Green's function methods, the PBE parameterization was used as a part of the GGA exchange-correlation potential to solve the Kohn-Sham equation. The angular momentum cut-off to the plane wave was taken to be ℓ_{max}= 3. The Brillouin zone integrations have been carried out on a uniform 20×20×20 **k**-mesh. The Green's functions were calculated for 32 complex energy points distributed exponentially on a semicircular contour. The energy convergence criterion was set to 10^{-6} Ry for the self-consistent cycles.

3.3 Results and Discussions

3.3.1 Structural properties and energetics related to martensitic transformations

Although first-principles electronic structure calculations had been performed earlier for Mn_2NiGa, Mn_2NiAl and Mn_2NiIn [178–180], they were done either with different methods and most importantly with different approximations to the exchange-correlation functionals. For example, the calculations on Mn_2NiGa and Mn_2NiIn were done with FP-LAPW method using GGA exchange-correlation functionals, whereas Pseudopotential method with LDA exchange-correlation functional was used to calculate the electronic structures in Mn_2NiAl. Therefore, a comparative analysis of the properties of all the members of the alloy series may not be consistent

T 3.1: Equilibrium lattice constants and total moments for Mn_2NiX alloys calculated in the cubic austenite phase with FP-LAPW, PW-USPP, PAW-PP, EMTO and KKR methods.

Systems Mn_2NiX	Method	Lattice const. (Å)	M_{tot} (μ_B)
Mn_2NiGa	FP-LAPW	5.835(5.907[a])	1.177
	PW-USPP	5.850	1.17
	PAW-PP	5.90	1.22
	KKR	5.90	1.26
	EMTO	5.848	1.19
Mn_2NiAl	FP-LAPW	5.802(5.636[b])	1.231
	PW-USPP	5.803	1.20
	PAW-PP	5.805	1.25
	KKR	5.805	1.28
	EMTO	5.809	1.26
Mn_2NiIn	FP-LAPW	6.164(6.162[c])	0.390
	PW-USPP	6.162	0.51
	PAW-PP	6.167	1.03
	KKR	6.168	1.02
	EMTO	6.170	0.61
Mn_2NiSn	FP-LAPW	6.147(6.099[d])	0.432
	PW-USPP	6.150	0.52
	PAW-PP	6.153	0.66
	KKR	6.154	0.71
	EMTO	6.158	0.57

a : Ref. [104], b : Ref. [179], c : Ref. [180], d : Ref. [102]

if done with these results and systematic calculations with a single method with consistent choice of parameters are necessary to understand the trends in the properties. Therefore, we first calculated the equilibrium lattice constants and corresponding total moments in the cubic austenite phase of Mn_2NiX materials within a single implementation of a first-principles based method. To check the consistency and accuracy in the results obtained by the five different first-principles based electronic structure methods described in the previous chapter, we calculated the aforesaid quantities for all the materials using those different implementations of DFT. The results are tabulated in T 3.1. Clearly, the lattice constants and total magnetic moments calculated with five different methods are in excellent agreement with one another. As was mentioned in chapter 1, we have used all five methods, depending upon the nature of the problem we were interested in. The results in T 3.1 established that this indeed can be done for these system. The available results on the lattice constants in Mn_2NiGa, Mn_2NiIn and Mn_2NiSn [108, 178, 180] also agree well with our computed results. On the contrary, the lattice constant of for Mn_2NiAl calculated by another group differ significantly with our results. The reason is that the lattice constant calculated by the other group used LDA functional which is known to underestimate the lattice constants.

T 3.2: The converged total energies (E_{tot}) corresponding to different starting magnetic configurations between two Mn atoms in the cubic phase of Mn_2NiSn. The lowest E_{tot} is taken to be 0 meV/atom as a reference. All calculations are done with the PW-USPP method and at the lattice constant 6.02 Å. GGA functional [137] has been used for the exchange-correlation part. The converged magnetic moments are also listed [176].

Starting Mn moment (μ_B)		Converged moment (μ_B)		Converged total moment (μ_B)	Converged E_{tot} (meV/atom)
MnI	MnII	MnI	MnII		
1	-1	2.97	-3.49	-0.64	0.00
1	-3	2.97	-3.49	-0.64	0.00
-1	3	2.97	3.49	0.64	0.00
-3	3	-2.97	3.49	0.64	0.00
-3	1	-2.97	3.49	0.64	0.00
-1	-3	-0.39	-3.27	-3.99	75.55
3	3	0.39	3.27	3.99	75.55
-3	-1	-0.39	-3.27	-3.99	75.55

In what follows, the results reported in the following subsections of this chapter, are obtained by calculations with FP-LAPW method. Supporting results from PW-USPP method are reported in appropriate places. In a previous theoretical study, Barman *et al.* [197] showed that

the starting alignment of the spins on two Mn sublattices is crucial for obtaining converged ground state densities. For Mn_2NiGa, they demonstrated that a parallel alignment of the two Mn spins in the beginning of the DFT calculations produces a total energy much higher than the actual ferrimagnetic ground state along with a moment larger than the ferrimagnetic one. We have verified this for all the others materials in Mn_2NiX series. Our calculated results with different starting spin configurations of the two inequivalent Mn atoms for Mn_2NiSn are listed in T 3.2. Rest of the calculations for these materials in inverse Heusler structure is done with antiparallel but unequal starting magnetic moments of the two Mn atoms. Next, we look into the energetics of these alloys when subjected to tetragonal distortions. The motivation is to see if a tetragonally deformed phase is energetically lower than the cubic phase and if the volumes of the two phases are nearly same. Both would act as confirmatory facts that the alloys can exhibit shape memory effect. Another motivation behind the study of the energetics of each alloy in consideration is to have a comparative estimate of the temperature that could be associated with cubic to tetragonal transformation, an information that would help in understanding the feasibility of realizing a particular system for MSM applications. To this end, we perform total energy calculations for different (c/a) values, an estimate of the tetragonal deformation, for each alloy system.

T 3.3: The structural parameters in the cubic and the tetragonal phases and δE, the energy differences between the cubic and the nonmodulated tetragonal phases for Mn_2NiX alloys calculated with FP-LAPW and PW-USPP electronic structure methods [177].

Systems Mn_2NiX	Method	Lattice const. (Å)	(c/a) local	(c/a) global	δE (meV/atom)
Mn_2NiGa	FP-LAPW	5.835(5.907[a])	0.93	1.28	29.291
	PW-USPP	5.850	0.92	1.28	30.213
Mn_2NiAl	FP-LAPW	5.802(5.636[b])	0.95	1.26	20.596
	PW-USPP	5.803	0.95	1.25	16.933
Mn_2NiIn	FP-LAPW	6.164(6.162[c])	0.98	1.25	5.869
	PW-USPP	6.162	none	1.22	2.489
Mn_2NiSn	FP-LAPW	6.147(6.099[d])	0.94	1.24	7.734
	PW-USPP	6.150	0.94	1.18	3.83

a : Ref. [104], b : Ref. [179], c : Ref. [180], d : Ref. [102]

After performing energy minimizations with respect to a and (c/a), we find that in all four systems, the differences between the volumes of the tetragonal phases and that of the cubic phases are less than 1%, which imply that the phase transformation is nearly volume conserving. The energy surfaces calculated by the FP-LAPW method (F 3.1(a)) show that

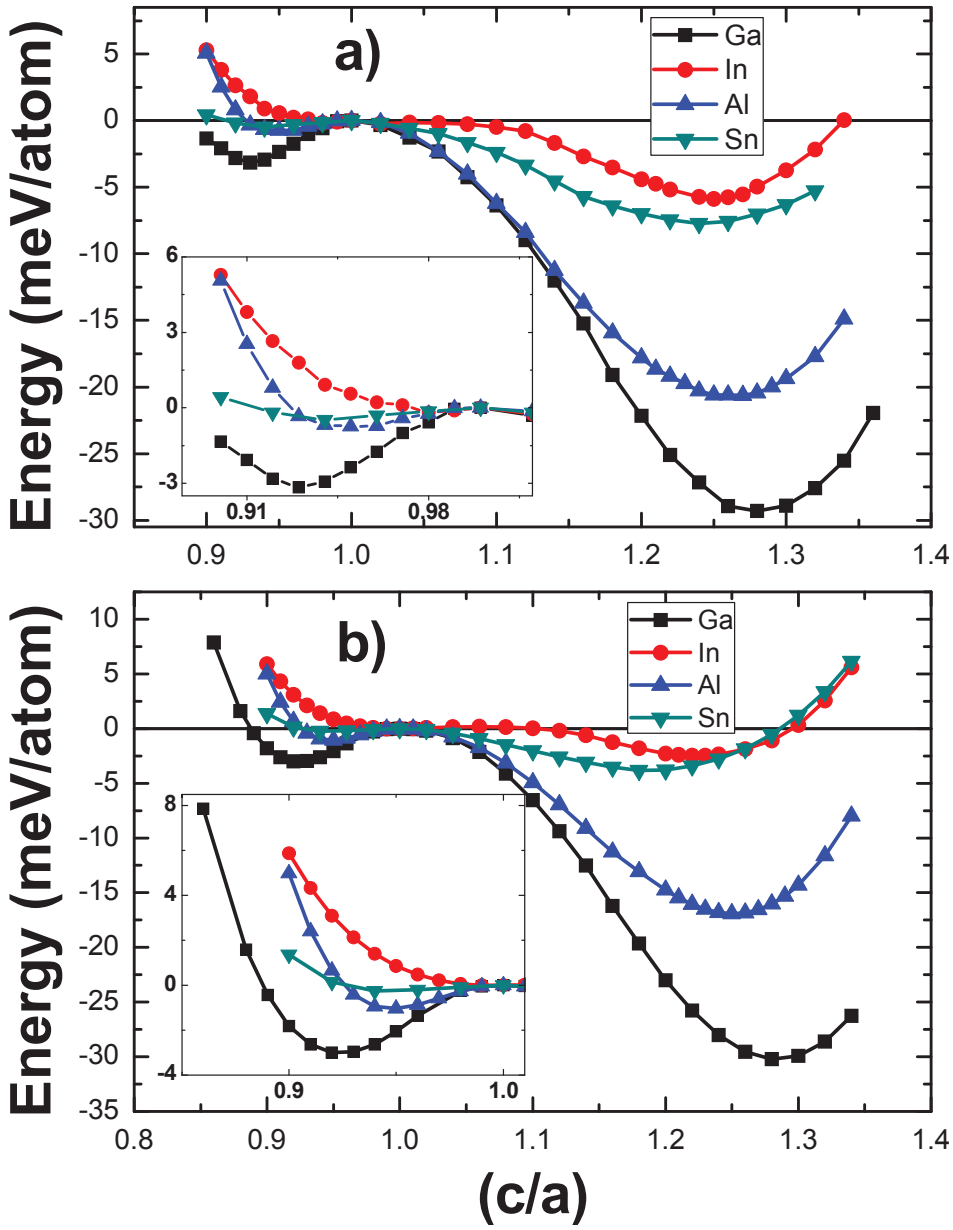

F 3.1: Total energy as a function of tetragonal deformations (c/a) for Mn_2NiX alloys. The energies calculated by the a) FP-LAPW method and b) PW-USPP method are plotted with reference to the energy of the cubic phase (c/a)= 1. The insets show the regions with (c/a)< 1 in a magnified scale [177].

for all the alloys, the energy surfaces are identical in features with a nonmodulated tetragonal phase for $(c/a)> 1$ being the lowest in energy. Along with these global minima, all curves show a metastable minima for $(c/a)< 1$. While these metastable minima are pronounced for Mn_2NiGa, Mn_2NiAl and Mn_2NiSn, it is not in case of Mn_2NiIn. It is to be noted here that the previous available result on the structural stability of Mn_2NiIn had predicted a stable tetragonal phase with $(c/a)\sim0.97$ [180]. Our results are in complete contradiction to this. Being isoelectronic with Al and Ga and having only one electron less than Sn, there would not be any obvious physical reason why only a -3% deformation in the cubic phase stabilizes the tetragonal phase in Mn_2NiIn, when a deformation of more than 20% is required to stabilize the tetragonal phases in the three other alloys. The energy surfaces in F 3.1(a) show that the minima at $(c/a)< 1$ are energetically very close to the cubic phase with maximum difference being ~3 meV per atom in case of Mn_2NiGa. For the other three systems, the differences are less than 1 meV per atom. The energy difference between the tetragonal phase with $(c/a)> 1$ and the cubic phase is maximum in case of Mn_2NiGa as is seen in T 3.3. The difference is of the same order in case of Mn_2NiAl while it is one order less in case of the other two alloys with the lowest one being about 6 meV per atom in case of Mn_2NiIn.

Analyzing the energy surfaces calculated by the PW-USPP method (F 3.1(b)), we find that the positions of the global and the local minima are nearly identical with the ones calculated by the FP-LAPW method for Mn_2NiGa and Mn_2NiAl, while there are some discrepancies in the other two cases. The global minima in the energy surface for Mn_2NiSn is at $(c/a)= 1.24$ in the FP-LAPW calculations while it is at $(c/a)= 1.18$ in the PW-USPP calculations. For Mn_2NiIn, no local minima for $(c/a)< 1$ is obtained in the PW-USPP calculations. These differences could be due to the fact that the FP-LAPW calculations, being more accurate, reveal certain subtle features which the USPP based calculations do not as is seen in case of Mn_2NiIn. The differences in results in case of Mn_2NiSn could be attributed to the particular choice of pseudopotential. Nevertheless, these differences do not affect the qualitative trends we are trying to explore. The energy differences between the tetragonal $(c/a)> 1$ phase and the cubic phase as computed by the PW-USPP method show identical trend as that obtained with results of the FP-LAPW calculations.

Comparison between the results using two different electronic structure methods show that the qualitative features of the energy surfaces and the trends in the energy differences between the austenitic and the martensitic phases are identical irrespective of the method of calculations. This validates the usage of the more accurate FP-LAPW method to study the energetics

of these systems. The following inferences can, therefore, be drawn: first, all the four alloys exhibit shape memory behavior characterized by a stable nonmodulated tetragonal phase with the phase transformation being volume conserving, second, trends in the T_M can be estimated from the energetics. Barman *et al.* had shown [197] that the energy difference between the nonmodulated tetragonal phase and the cubic phase can be considered as a measure of the martensitic transformation temperature. Thus, if one considers the energy difference of ∼30 meV per atom for Mn_2NiGa equivalent to the experimentally observed martensitic transformation temperature of 270 K , the transformation temperature for Mn_2NiAl would be ∼200 K while for the other two alloys it is one order less. Therefore, except Mn_2NiGa, other alloys are not suitable for shape memory applications in their stoichiometric compositions, third, a metastable minima for $(c/a)< 1$ is present in all alloys, although the available experiments on Mn_2NiGa [104] did not observe this. This feature is similar to the one observed in Ni_2MnGa, where the origin of this was shown to be an artifact of periodic modulations on the austenitic phase [198]. The other origins of such minima could be chemical disorder or noncollinearity in the magnetic structure, but since these factors are not considered in our calculations, the appearance of the metastable minima could be indicative of the possibility that these systems transform to the nonmodulated tetragonal state through a metastable modulated state as it was in case of Ni_2MnGa. The discrepancy between the results of Ref. [180] and our calculations in case of Mn_2NiIn is more startling as the distortions required for the martensitic transformation are substantially different. However, the small distortion obtained in Ref. [180] could be due to the fact that the energy surface being rather flat, the calculations converged to one of the two energetically close minima which, in fact, is not the global minima.

3.3.2 Magnetic moments

The total and partial magnetic moments, calculated by the FP-LAPW method, for the systems under consideration are given in T 3.4. For all the alloys, MnI and MnII atoms are seen to couple antiferromagnetically with each other producing a ferrimagnetic ground state. A clear trend in the magnetic moments across the alloy series, identical for both phases, emerges. The net moment is maximum for Mn_2NiAl and it decreases in the sequence $Mn_2NiAl \rightarrow Mn_2NiGa \rightarrow Mn_2NiSn \rightarrow Mn_2NiIn$. While the moments for Mn_2NiAl and Mn_2NiGa are greater than 1 μ_B per formula unit, Mn_2NiSn and Mn_2NiIn have substantially smaller moments ($< 0.5\ \mu_B$). An inspection of the partial moments suggest that in case of the later two alloys, the moments

T 3.4: The total (M_{tot}) magnetic moments of Mn_2NiX materials and partial (M_i) magnetic moments of the constituting atoms calculated by FP-LAPW method [177].

Systems	Cubic					Tetragonal				
Mn_2NiX	M_{tot} (μ_B/f.u.)	M_{MnI} (μ_B)	M_{MnII} (μ_B)	M_{Ni} (μ_B)	M_X (μ_B)	M_{tot} (μ_B/f.u.)	M_{MnI} (μ_B)	M_{MnII} (μ_B)	M_{Ni} (μ_B)	M_X (μ_B)
Mn_2NiGa	1.177	-2.336	3.123	0.328	0.013	1.017	-2.311	3.009	0.273	0.009
Mn_2NiAl	1.231	-2.007	2.887	0.319	0.000	1.038	-2.067	2.801	0.280	0.002
Mn_2NiIn	0.390	-3.518	3.753	0.104	0.003	0.254	-3.559	3.717	0.056	0.003
Mn_2NiSn	0.432	-3.314	3.610	0.100	0.014	0.231	-3.362	3.551	0.010	0.000

on the two Mn sites are stable and nearly compensate each other along with a significantly smaller moment on Ni sites in comparison to that in case of former two alloys, thus, producing a smaller net moment. In the martensitic phases, the total moment of each alloy is reduced in comparison to its moment in the austenitic phase. Results presented in T 3.4 suggest that a overall weakening of the ferromagnetic (FM) interactions manifested in lowering of MnII and Ni moments compared to those in the austenitic phases are responsible for this. Quantitatively, the total and partial moments for Mn_2NiGa calculated in this work agree well with the values obtained in Ref. [178]. For Mn_2NiAl, our calculated total and partial moments differ by about 15% with Ref. [179]. The reason, again, could be because of using local density approximation in Ref. [179]. For Mn_2NiIn, the trends of moments between the austenitic and martensitic phases obtained in our calculations are exactly opposite to that obtained in Ref. [180]. However, their moments in the martensitic phase are for (c/a)= 0.97 and the values are very close to those obtained in austenitic phase. This is understandable as no substantial changes in the inter-atomic distances between magnetic atoms in the martensitic phase with respect to those in the austenitic phase could be obtained with such a small distortion, the moments in their tetragonal phase are expected to change only a little. Our results, on the other hand, are consistent with the trends obtained in the other alloys.

Although it is tempting to correlate the trends in the moments across the alloy series with the trends in the lattice constants and thus to explain the trend of decreasing moments from Mn_2NiAl to Mn_2NiIn in terms of increasing lattice constants, the detailed explanation of results such as a substantial drop in the Ni moments for Mn_2NiSn and Mn_2NiIn, stable and near compensating Mn moments on crystallographically inequivalent sites for these two alloys and not for the other two require in-depth analysis in terms of the electronic structure.

The explanation of the trends in the energy surfaces for the alloy series also can be done by analyzing the differences in the electronic structures of the alloys. We present such analysis in the next subsection.

3.3.3 Electronic structures and analysis of the trends in phase stabilities and magnetic properties

In what follows, the spin-projected total (DOS) and atom-projected (PDOS) densities of states for Mn_2NiGa, Mn_2NiAl, Mn_2NiIn and Mn_2NiSn are presented in F 3.2- 3.5, respectively. For each alloy, the DOS and the PDOS in the cubic phase (c/a= 1), the metastable phase ((c/a)< 1) and the stable tetragonal phase ((c/a)> 1) are presented. The PDOS are the total contributions from the *s*, *p* and *d* orbitals, but the *d* orbitals dominate the envelopes. A comparison of the DOSs show that the electronic structures of Mn_2NiGa and Mn_2NiAl systems have similarities among themselves and that their electronic structures are very different than those of the other two alloys in the series. The other two alloys, Mn_2NiIn and Mn_2NiSn, too have similarities in their electronic structures.

F 3.2 and 3.3 show that in the cubic phase, the majority spin DOS at the Fermi levels are substantial for Mn_2NiGa and Mn_2NiAl implying an instability of the phase. The structures in the majority and minority spin DOS near the Fermi levels are due to the contributions from Ni and Mn atoms of both symmetries. The bonding majority peaks at around -0.1 eV and the anti-bonding majority peaks at around 0.4 eV have contributions from Ni, MnI and MnII *d* electrons in case of both alloys. Similarly, the contributions towards the states in the minority bands near the Fermi levels come uniformly from the *d* electrons of the three magnetic components. The majority anti-bonding peaks at ~1.3 eV for Mn_2NiGa and at ~1.2 eV for Mn_2NiAl, are, however, mostly due to the MnI atoms. Similarly, the minority anti-bonding peaks at ~0.7 eV are mainly due to the MnII atoms. The structures in the majority spin bonding DOS, away from the Fermi levels, are due to the strong hybridizations between the Ni and the MnII *d* electrons while the minority spin bonding DOS, away from the Fermi levels, are due to the hybridizations between the Ni and the MnI *d* states. Another noteworthy feature of the majority spin DOS in the cubic structures for both alloys is the presence of a deep valley between -1.2 eV and -0.35 eV. A similar valley around -0.4 eV is observed in the Mn_2NiAl minority spin band. A large tetragonal distortion ((c/a)> 1.25) breaks the

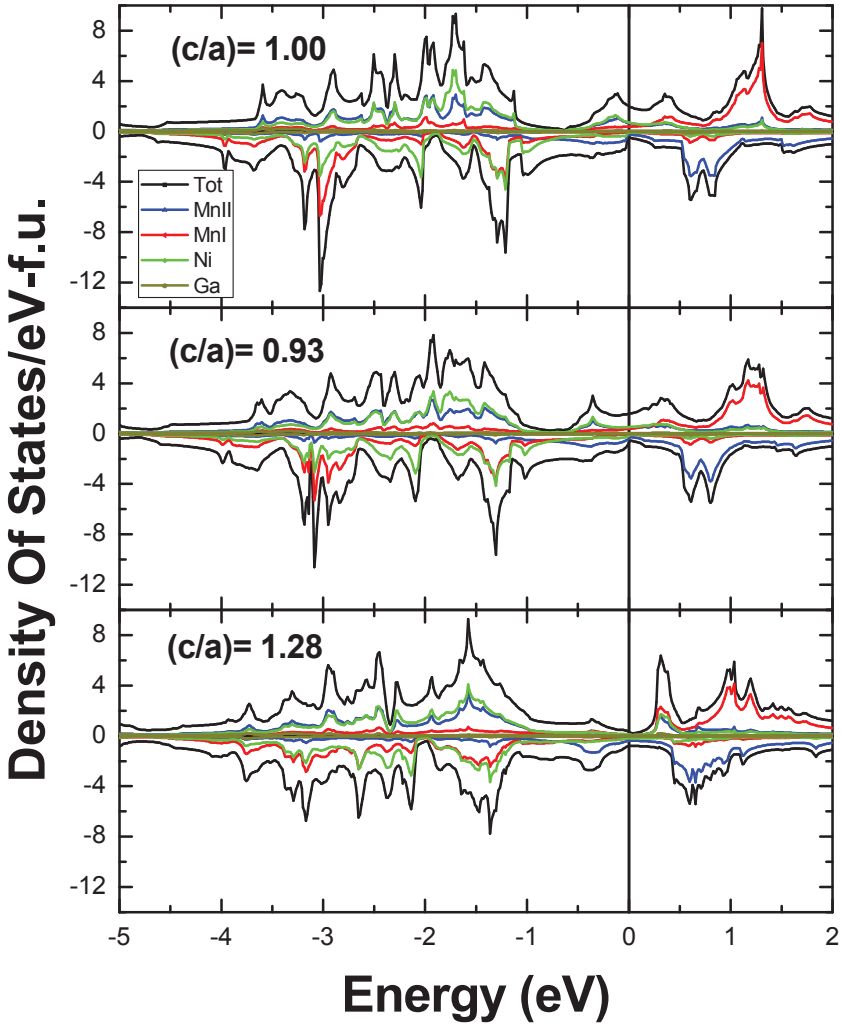

F 3.2: Spin-polarized total and atom-projected densities of states of Mn_2NiGa calculated at the cubic phase (c/a)= 1, at the metastable martensitic phase (c/a)= 0.93 and at the stable martensitic phase (c/a)= 1.28. The Fermi energy is considered as zero [177].

symmetries of the *d* orbitals resulting in transforming the majority spin peaks near 1.3 eV (for Mn_2NiGa) and 1.2 eV (for Mn_2NiAl) into multiple peaks with reduced intensities and an overall shift of states towards lower energies. Due to such migrations of states, the valleys in the majority spin bands get filled. Lowering of symmetry, similarly, splits the single peaks at

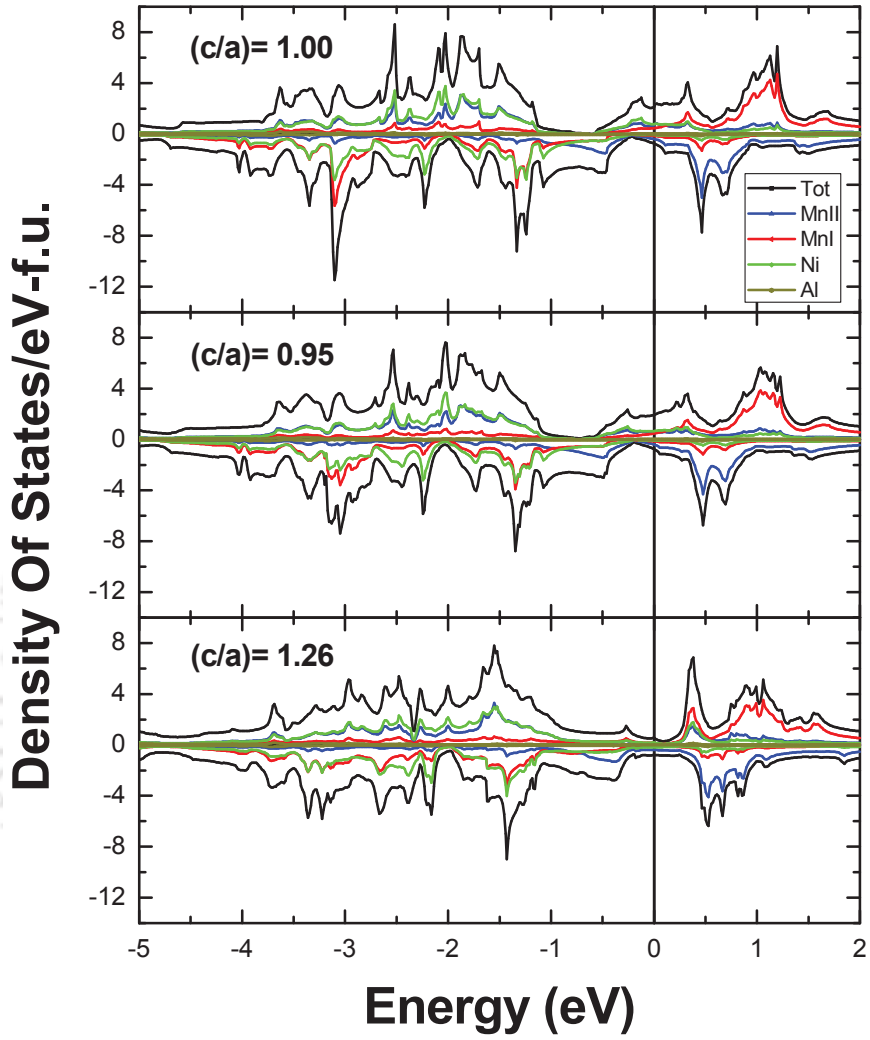

F 3.3: Spin-polarized total and atom-projected densities of states of Mn_2NiAl calculated at the cubic phase (c/a)= 1, at the metastable martensitic phase (c/a)= 0.95 and at the stable martensitic phase (c/a)= 1.26. The Fermi energy is considered as zero [177].

~0.7 eV in the minority bands of the cubic structures into multiple peaks.

The electrons are pushed towards lower energies, filling the valley in case of Mn_2NiAl and producing a small peak in the Mn_2NiGa DOS, both at around -0.4 eV. These migrations

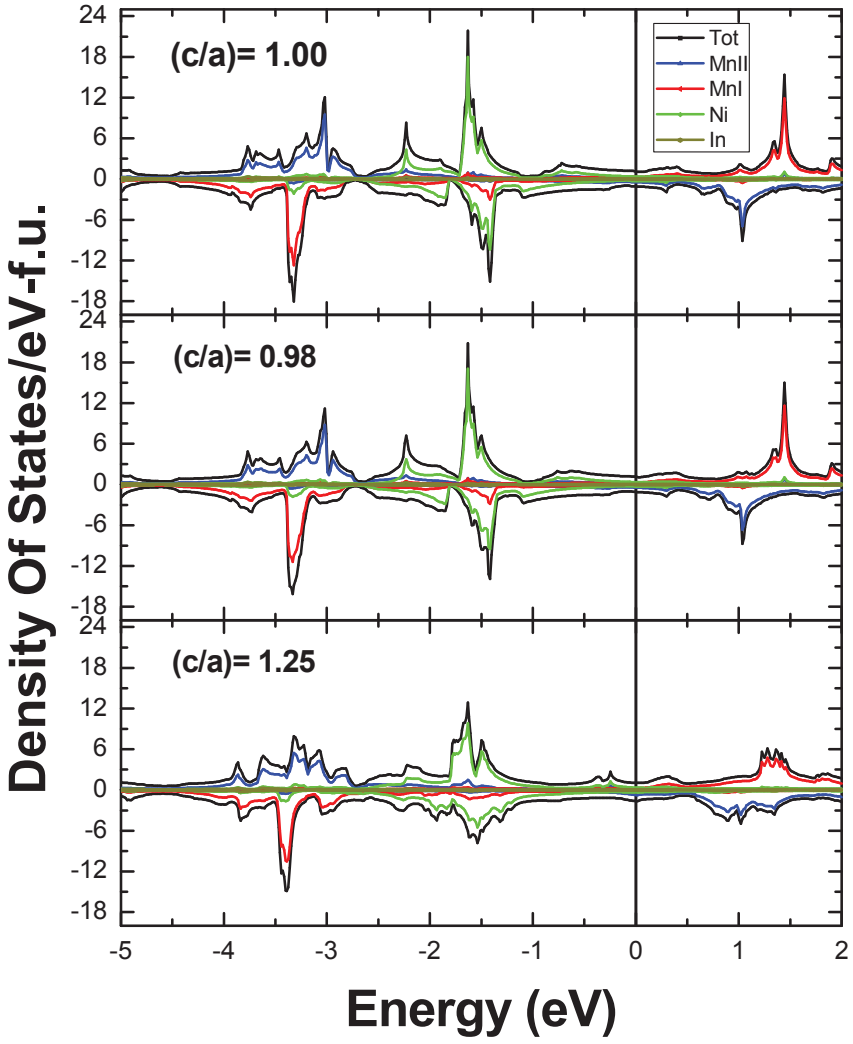

F 3.4: Spin-polarized total and atom-projected densities of states of Mn_2NiIn calculated at the cubic phase (c/a)= 1, at the metastable martensitic phase (c/a)= 0.98 and at the stable martensitic phase (c/a)= 1.25. The Fermi energy is considered as zero [177].

of electronic states towards lower energies stabilize the tetragonal phases ((c/a)> 1.25) over their cubic phases. Inspection of the DOS for the metastable tetragonal structures ((c/a)< 1) for these alloys indicate better stabilities with respect to the cubic phases due to migrations of states towards lower energies exemplified by the shift of the minority peaks at -0.1 eV in the

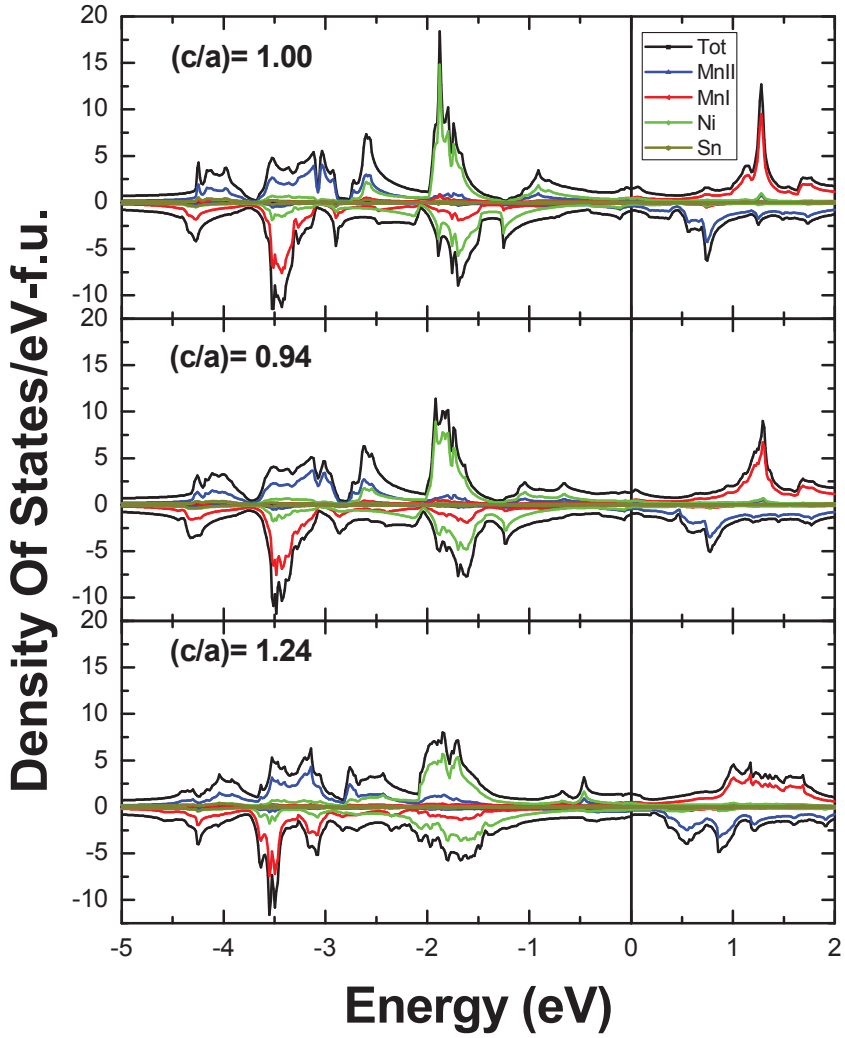

F 3.5: Spin-polarized total and atom-projected densities of states of Mn_2NiSn calculated at the cubic phase (c/a)= 1, at the metastable martensitic phase (c/a)= 0.94 and at the stable martensitic phase (c/a)= 1.24. The Fermi energy is considered as zero [177].

cubic structures towards lower energies in the tetragonal structure, but, the overall structures of the DOS do not change significantly as compared to those in cubic phases. This explains why the (c/a)< 1 tetragonal phases are metastable and energetically marginally lower than the cubic phases.

Comparison of F 3.4 and 3.5 with F 3.2 and 3.3 suggest that the DOS of Mn_2NiSn and Mn_2NiIn are markedly different. The DOS at the Fermi levels in the cubic phases are much smaller in comparison to those in Mn_2NiAl and Mn_2NiGa, implying a greater stability of the cubic phases in case of Mn_2NiIn and Mn_2NiSn, although the two peak structures close to the Fermi levels in the majority spin band with one peak from bonding states and the other from anti-bonding states as were observed in case of the Mn_2NiAl and Mn_2NiGa prevail. However, the bonding peak now lies much deeper in energy at ~-1 eV for both the alloys. The anti-bonding peak in the majority band appears at ~0.5 eV in Mn_2NiIn while the same in Mn_2NiSn appears much closer to the Fermi level. Thus the valleys in the majority bonding states below the peaks at -1 eV are shallower in comparison to the other two alloys. Overall, there are fewer structures in the DOS of Mn_2NiIn and Mn_2NiSn in comparison to the other two alloys. The appearance of less structures in the DOS is due to weak hybridizations between the Ni and the Mn atoms. The majority anti-bonding states in these two systems are overwhelmingly populated by the MnI atoms while the minority anti-bonding ones are dominated by the MnII atoms alone. The structures near the Fermi level for both bonding and anti-bonding states though have contributions from all components but the intensities are quite small. The PDOS contributions for the bonding states away from the Fermi levels show that there are little hybridizations between the Ni and the Mn atoms of both types. The nature of hybridizations do not change in the tetragonal phases ($(c/a)> 1$). A large tetragonal distortion ($(c/a)> 1.25$) breaks the symmetries of the *d* states producing multiple peaks in both majority and minority anti-bonding states and pushes the electrons towards lower energies. These can be understood from the increased intensities of the anti-bonding states at lower energies, the filling up of the valleys around -1 eV in the majority bands and the appearance of double peaks in the majority bands at around -0.25 eV for Mn_2NiIn and at around -0.5 eV for Mn_2NiSn. However, weak hybridizations between the Ni and Mn states do not produce effects as significant as were observed for the other two alloys as one goes from cubic to tetragonal phases. One indicator of this is the relative changes in the DOS at the Fermi levels upon phase transformation. While the DOS at Fermi level reduced substantially in the tetragonal phases in comparison to that in cubic phases for Mn_2NiAl and for Mn_2NiGa, such reductions in cases of the other two alloys are minuscule. All these observations provide a possible explanation to the relative differences in the magnitudes of energies associated with the martensitic transformations among the systems investigated. It appears that in cases of Mn_2NiSn and Mn_2NiIn, the relatively better stability of the cubic phases do

not push the states towards lower energies substantially upon lowering symmetry in comparison to the other two alloys. From the preceding discussions, it is clear that the degree of hybridizations among Ni and Mn atoms are responsible for such differences. This, in turn, may be related to the inter-atomic distances between the magnetic atoms. T 3.5 shows the inter-atomic distances for all systems considered here. The results suggest that the weaker hybridizations between the Ni and Mn states for Mn_2NiIn and Mn_2NiSn are an artifact of larger inter-atomic distances between the magnetic atoms in comparison to those in other two alloys. Since the inter-atomic distances change only slightly upon transformation from cubic to tetragonal phases, the hybridizations do not get affected considerably. The DOS for the metastable states for both alloys hardly show any differences with those in the cubic phases. Though some differences,such as the splitting of peaks in the majority bands at -1 eV and at -2 eV and in the minority bands between -1.5 eV and -2 eV are observed between the electronic structures in the cubic and the metastable phases of Mn_2NiSn, no such visible differences are present in case of Mn_2NiIn. This explains why an extremely shallow metastable minimum is obtained in the energy surface of Mn_2NiIn.

T 3.5: The inter-atomic distances (in Å) between the magnetic atoms for Mn_2NiX systems [177].

Systems	Cubic			Tetragonal		
Mn_2NiX	MnI-MnII	Ni-MnI	Ni-MnII	MnI-MnII	Ni-MnI	Ni-MnII
Mn_2NiGa	2.56	2.95	2.56	2.59	2.72	2.59
Mn_2NiAl	2.51	2.90	2.51	2.54	2.69	2.54
Mn_2NiIn	2.67	3.08	2.67	2.70	2.86	2.70
Mn_2NiSn	2.64	3.04	2.64	2.67	2.84	2.67

The trends in the magnetic properties presented in T 3.4 can also be explained from the electronic structures. The antiferromagnetic alignments between the Mn atoms occupying lattice points of different symmetries are due to the shorter Mn-Mn inter-atomic distances in the Hg_2CuTi structures compared to the Heusler structure in which the Ni_2MnX alloys crystallize. It was shown earlier that for Mn-excess alloys like $Ni_2Mn_{1+x}Ga_{1-x}$ [199], $Ni_{2-x}Mn_{1+x}Ga$ [200] and $Ni_2Mn_{1+x}Al_{1-x}$ [98, 201] alloys in the family of Ni_2MnX systems, the Mn atoms occupying Ga,Ni and Al anti-sites respectively, align anti-parallelly with the Mn atoms at the original Mn sub-lattice due to the shorter Mn-Mn distances. The same argument is valid here. The reason that a ferrimagnetic order with uncompensated Mn moments are obtained for the Mn_2NiX systems, in spite of two Mn atoms per formula unit, is that the hybridizations

between the spin majority Ni and Mn-II 3*d* states are stronger than those between the spin minority Ni and Mn-I states. This, in turn, is related to the larger Ni-MnI distances relative to the Ni-MnII distances in both phases (T 3.5). The hybridization patterns presented in F 3.2- 3.5 also explain the trends in the atom projected moments for these systems. For Mn_2NiGa and Mn_2NiAl, a larger Ni moment and a larger unbalanced moment on the Mn sites are an artifact of strong hybridizations between the Ni and Mn atoms as discussed above. However, the near compensations of the Mn moments and small Ni moments in case of Mn_2NiSn and Mn_2NiIn are due to the weak hybridizations between the Ni and the Mn atoms. This is obvious from the appearances of the well separated partial contributions from Ni and Mn atoms in the PDOS. Also, the reason behind the near-compensations of the MnI and MnII moments for these two alloys can be understood from the nearly same PDOS in both majority and minority bands of these two atoms. The majority and minority DOS for Ni atoms also appear to be nearly equal, thus, explaining the small amount of Ni moments in these two alloys. The decrease in the moments in the tetragonal phases ($(c/a)> 1$) are due to a larger reduction in MnII and Ni moments. The slight increase in the Ni-MnII distances in the tetragonal phase in comparison to those in the cubic phases, and subsequent weakening of the hybridizations are the reasons behind such reductions in the partial and total moments.

3.4 Summary

Using first-principles based electronic structure methods, the prospect of shape memory effect has been investigated in all the Mn_2NiX systems. We observe a volume conserving structural phase transformation from cubic to nonmodulated tetragonal phases for all the materials we consider. Energy surfaces of all the materials reveal that the daughter phases (tetragonal), characterized with tetragonal deformation (c/a)> 1, are energetically favorable than the parent phases (cubic). Additionally, all the above materials also have shallow minima in their energy landscapes with (c/a)< 1, signifying the existence of modulated structure, which is precursor to the martensitic phase. From the energy difference between the cubic and the martensitic phase, we conclude that only Mn_2NiGa and Mn_2NiAl would be suitable for practical applications, since their T_M would lie close to the room temperature. The trends in the energetics are explained with the hybridizations between Ni and the two crystallographically

inequivalent Mn atoms. Relatively weaker hybridizations between those magnetic atoms result into nearly stable cubic phase for Mn_2NiIn and Mn_2NiSn. Since the main contributor to net magnetization is Mn atoms and their ferrimagnetic alignment produce smaller moments compared to Ni_2MnX systems. The net moments of Mn_2NiIn and Mn_2NiSn are smaller than the other two materials by at least a factor of two, which can be explain by the weak hybridizations between the magnetic atoms occur basically due to larger distances between magnetic atoms. The *sp* elements play the role of modifying the inter-atomic distance and thus influencing the hybridizations between the magnetic constituents. Therefore, the physical properties of these materials are influenced by the relative sizes of the *sp* elements.

Chapter 4

Understanding the origin of the martensitic transformation in Mn_2NiX alloys from their lattice dynamics* †

4.1 Introduction

The theory of lattice dynamics is considered as one of the pillars on which the modern day condensed matter physics stands. Many important achievements would not have been accomplished in modern solid state physics without a strong contribution from the investigations of lattice vibrations. The studies on lattice vibrations are used to explain specific heats, thermal expansion, heat conduction, the resistivity of metals, superconductivity and the temperature dependencies of optical spectra etc. Thus, the research on phonon excitations in solids offers interesting perspectives regarding materials properties and behavior. Useful insight about the ordering behavior, phase stability and elastic properties can be obtained from the phonon dispersion relations of solids. Phonon excitations play an important role in materials undergoing martensitic transformations.

*Contents of this chapter are mostly taken from Ref. [202].

†Permission from the publisher has been obtained for reprints of Ref. [202].

As has been stated in chapter 1, the martensitic transformation is merely a consequence of the reshuffling of atomic planes, which is often mediated through different periodically modulated metastable structures called premartensitic structure. Very often, the microscopic origin behind the martensitic phase transformation can be explained by softening of some phonon modes, related to the softness in elastic stiffness constants, caused by the nesting topology between parallel Fermi surfaces due to intense electron-phonon coupling. This has been the case for almost all the ternary MSMAs crystallizing in Heusler structure. The structural instability of Ni_2MnGa in the high temperature phase has been linked with an anomalous phonon softening of transverse acoustic TA_2 branch along [$\xi\xi$0] direction. The softening occurs at a fractional wave vector ξ= (0.33,0.33,0) and it becomes more prominent as one approaches towards the martensitic phase with decreasing temperature [92, 203]. The phonon softening has been found to correlate with the premartensitic phase, which is anticipated by the precursor phonon softening at that wave vector. Inelastic neutron scattering experiments and elastic constants measurements on the high temperature phase corroborated the theoretical calculations of softening of acoustic branch. A complete softening of the acoustic TA_2 branch with imaginary frequencies along [$\xi\xi$0] direction has been reported Ni_2MnAl [204]. The neutron scattering experiments performed by Moya *et al.* on this system verify the softening in TA_2 mode between the wave vector ξ= 0.25 and ξ= 0.4, but the phonon frequencies remain finite at any wave vector even at the lowest temperatures [205]. This could be related to the fact that the composition needed for the martensitic phase transformation to occur in Ni_2MnAl is slightly off-stoichiometric [98]. The phonon dispersion curves for Ni_2MnIn determined from inelastic neutron scattering showed the features typical of BCC materials that undergo martensitic transformations, i.e., low energies of the phonons of the transverse TA_2 [$\xi\xi$0] branch and a wiggle at ξ= 0.33. Later, Ağduk calculated the phonon dispersion spectra, which are in excellent agreement with the experimental results [206]. They also studied the vibrational properties of Ni_2MnSn and Ni_2MnSb from first-principles electronic structure method. The softening of Ni_2MnSn system is relatively weak compared to Ni_2MnSb, so that the phonon frequencies remain finite at any wavevector along [$\xi\xi$0]. The softening occurs at ξ= 0.35 and ξ= 0.40 wave vectors for Ni_2MnSn and Ni_2MnSb, respectively. On the other hand, a remarkable vibrational instability is observed in TA_2 branch of Ni_2MnSb which consists of negative vibration frequencies between ξ = 0.55 and ξ = 0.85 [207].

In the previous chapter, we established that all the Mn_2Ni*X* materials undergo martensitic transformations. Thus, in order to understand the origin of these martensitic transformations,

it is only natural to explore the lattice dynamics. In this chapter, we compute the vibrational properties of the four Mn_2NiX materials in a systematic way. We compute the phonon dispersions, the vibrational density of states, the elastic constants and the Fermi surfaces in order to ascertain the mechanisms driving the martensitic transformations.

4.2 Computational details

The electronic structures of the systems considered were calculated using the UltraSoft Pseudopotential (PW-USPP) formalism of the Density Functional Theory (DFT), as implemented in Q E [187] code. The phonon spectra were obtained by Density Functional Perturbation Theory (DFPT) method. DFPT [127] is a DFT [109, 111] based linear response method to obtain the lattice dynamical properties in condensed matter systems. The inter-atomic force constants required to calculate the phonon frequencies are derived via the linear response of the electronic subsystems. The Hellmann-Feynman theorem [208, 209] is used to calculate the elements of the force constant matrices.

$$C_{\mathbf{R}_I\mathbf{R}_J} = \frac{-\partial \mathbf{F}_I}{\partial \mathbf{R}_J} = \int \frac{\partial n_{\mathbf{R}}(\mathbf{r})}{\partial \mathbf{R}_J} \frac{\partial V_{\mathbf{R}}(\mathbf{r})}{\partial \mathbf{R}_I} d\mathbf{r} + \int n_{\mathbf{R}}(\mathbf{r}) \frac{\partial^2 V_{\mathbf{R}}(\mathbf{r})}{\partial \mathbf{R}_I \partial \mathbf{R}_J} + \frac{\partial^2 E_N(\mathbf{R})}{\partial \mathbf{R}_I \partial \mathbf{R}_J} \tag{4.1}$$

$\mathbf{R}_I, \mathbf{R}_J$ are the ionic positions, $\mathbf{F}_I$ is the Hellmann-Feynman force on the I-th nucleus, $n_{\mathbf{R}}(\mathbf{r})$ is the ground state electronic charge density corresponding to the nuclear configuration $\mathbf{R}$, $V_{\mathbf{R}}(\mathbf{r})$ is the electron-nucleus interaction and E_N is the ion-ion interaction energy. From equation 4.1, it is clear that the inter-atomic force constants are determined from the ground state charge density and its linear response to a distortion in the ionic configuration. In the DFPT, these quantities are calculated within the DFT framework.

We assume that the external potential acting on the electrons is a differentiable function of a set of parameters, $\lambda \equiv \{\lambda_i\}$ ($\lambda_i \equiv \mathbf{R}_I$ in the case of lattice dynamics). According to the Hellmann-Feynman theorem, the first and second derivatives of the ground state energy are

$$\frac{\partial E}{\partial \lambda_i} = \int \frac{\partial V_\lambda(\mathbf{r})}{\partial \lambda_i} n_\lambda(\mathbf{r}) d\mathbf{r} \tag{4.2}$$

$$\frac{\partial^2 E}{\partial\lambda_i\partial\lambda_j} = \int \frac{\partial^2 V_\lambda(\mathbf{r})}{\partial\lambda_i\partial\lambda_j} n_\lambda(\mathbf{r}) d\mathbf{r} + \int \frac{\partial n_\lambda(\mathbf{r})}{\partial\lambda_i}\frac{\partial V_\lambda(\mathbf{r})}{\partial\lambda_j} d\mathbf{r} \tag{4.3}$$

Linearization of charge density equation in DFT leads to

$$\Delta n(\mathbf{r}) = 4\ \mathrm{Re}\sum_{n=1}^{N/2} \psi_n^*(\mathbf{r})\,\Delta\psi_n(\mathbf{r}) \tag{4.4}$$

where the finite difference operator Δ^λ is defined as

$$\Delta^\lambda F = \sum_i \frac{\partial F_\lambda}{\partial\lambda_i}\Delta\lambda_i \tag{4.5}$$

The superscript λ has been omitted in equation 4.4 as well as in any subsequent formulae without the loss of generality. The variation of the Kohn-Sham orbitals, $\Delta\psi_n(\mathbf{r})$ is obtained by standard first order perturbation theory [210]:

$$(H_{SCF} - \epsilon_n)\,|\Delta\psi_n\rangle = -(\Delta V_{SCF} - \Delta\epsilon_n)\,|\psi_n\rangle, \tag{4.6}$$

where,

$$H_{SCF} = -\frac{\hbar^2}{2m}\frac{\partial^2}{\partial\mathbf{r}^2} + V_{SCF}(\mathbf{r}) \tag{4.7}$$

is the unperturbed Kohn-Sham Hamiltonian,

$$\Delta V_{SCF}(\mathbf{r}) = \Delta V(\mathbf{r}) + e^2\int \frac{\Delta n(\mathbf{r}')}{|\mathbf{r}-\mathbf{r}'|}d\mathbf{r}' + \left.\frac{dv_{xc}(n)}{dn}\right|_{n=n(\mathbf{r})}\Delta n(\mathbf{r}) \tag{4.8}$$

is the first order correction to the self consistent-potential and $\Delta\epsilon_n = \langle\psi_n|\Delta V_{SCF}|\psi_n\rangle$ is the first order variation of the Kohn-Sham eigenvalue, ϵ_n.

equations 4.4-4.8 form a set of self-consistent equations for the perturbed system completely analogous to the Kohn-Sham equations in the unperturbed case. The problem will arise due to the linear operator appearing in the left-side of equation 4.6 which has a null eigenvalue. However, the response of the system to an external perturbation only depends on the component of the perturbation that couples the manifold of occupied states with that of the empty states. The projection onto the empty-state manifold of the first order correction to occupied orbitals can be obtained from equation 4.6 by replacing its right-hand side with $-P_c\Delta V_{SCF}|\psi_n\rangle$, where P_c is the projector onto the empty-state manifold, and by adding to the linear operator on its left-hand side $H_{SCF} - \epsilon_n$, a multiple of the projector onto the

occupied-state manifold, P_v, so as to make it nonsingular:

$$(H_{SCF} - \alpha P_v - \epsilon_n)\,|\Delta\psi_n\rangle = -P_c \Delta V_{SCF} |\psi_n\rangle \tag{4.9}$$

The basic algorithm for DFPT consists of solving the set of linear equation 4.9 for $\Delta\psi_n$ and expression 4.8 for ΔV_{SCF} in terms of Δn, which is given by Since Δn is a function of the set of occupied $\Delta\psi_n$, this forms a self-consistent set of equations which can be solved by any efficient iterative method. In the next two paragraphs, we describe the computational details for the calculation of electronic and dynamical properties for Mn_2NiX materials, respectively.

UltraSoft PseudoPotentials (USPP) [191] were used to accurately calculate the electronic ground states. Spin polarized Generalized Gradient Approximation (GGA) scheme was used as the exchange-correlation part of the potential with Perdew-Wang 91 parameterizations (PW91) [138]. Plane waves with energies up to 544 eV were used to describe electronic wave functions. Fourier component of the augmented charge density with cut-off energy up to 6530 eV was taken after convergence tests. The Brillouin zone integrations were carried out with finite temperature Methfessel-Paxton smearing [211] method using 12×12×12 uniform **k**-mesh, which effectively leads to 364 **k**-points in the irreducible wedge of the Brillouin zone. The value of the smearing parameter was taken as 0.27 eV. Such choices of the parameters ensure the convergence of phonon frequencies within 5%.

The energy threshold value for convergence was 10^{-16} Ry in phonon calculations. Dynamical matrices were conveniently calculated in reciprocal space from the ground state charge density and from its linear response to the distortion in the ionic configurations. Fourier transform was employed thereafter to obtain the real space force constants. The dynamical matrices were calculated in a 4×4×4 **q**-point grid for all the structures. Convergence of phonon frequencies within 1-2% was ensured by comparing frequencies calculated directly and frequencies obtained by the Fourier transform of the dynamical matrices. Such convergence tests ensured accuracies in elastic constants as they are calculated from the slopes of the phonon dispersion curves. The Fermi surfaces were calculated on $24 \times 24 \times 24$ highly dense uniform **k**-point grid. It may be noted that the strength of the phonon anomaly is extremely sensitive to temperature. An increase in temperature can reduce the nesting features of Fermi surfaces and thus weaken the anomaly. In DFT based calculations, the smearing parameter σ plays the role of fictitious electronic temperature. Therefore, to reduce the effect of finite temperature in the calculations of Fermi surfaces, we kept σ= 0.01 eV all along.

4.3 Results and Discussions

4.3.1 Phonon dispersion

In absence of experimental information on the lattice constants of Mn_2NiAl and Mn_2NiIn, we have used the DFT calculated lattice constants presented in T 3.1 of chapter 3 for all the four alloys. Since, the experimental lattice constants agree well with our calculated ones for Mn_2NiGa and Mn_2NiSn, we consider the DFT calculated lattice constants as good representations of the experimental ones. The phonon dispersion spectra calculated at these lattice constants along [$\xi\xi$0] highly symmetric direction in the irreducible segment of the Brillouin zone (IBZ) are shown in F 6.5.

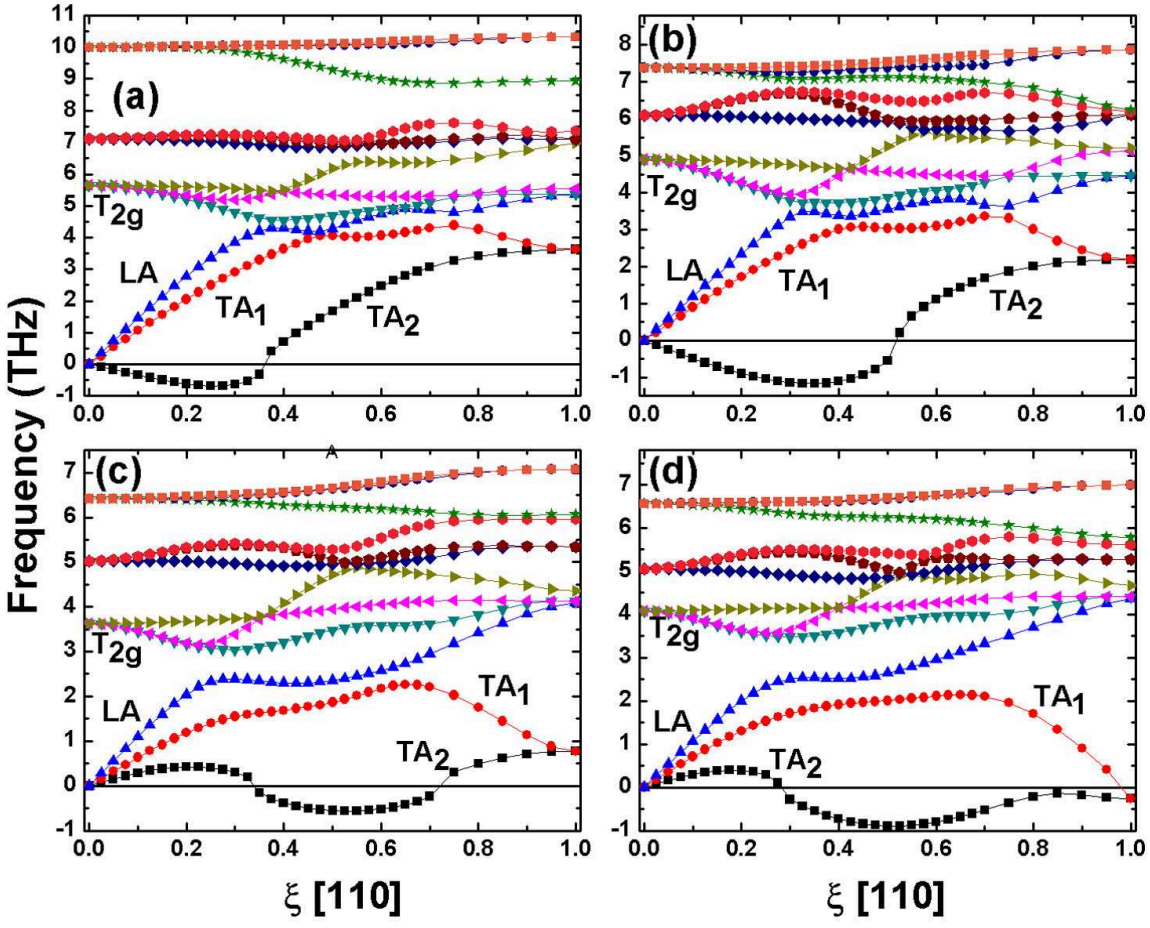

F 4.1: Phonon dispersion spectra of (a) Mn_2NiAl, (b) Mn_2NiGa, (c) Mn_2NiIn and (d) Mn_2NiSn along [$\xi\xi$0] highly symmetric direction of the Brillouin zone. The phonon wave vector ξ is expressed in units of ($\frac{2\pi}{a}$) [202].

Our main interest lies in the transverse acoustic TA_2 branch, which exists due to the atomic displacements $[\xi\bar{\xi}0]$ perpendicular to the propagation direction $[\xi\xi0]$. For all Heusler systems exhibiting martensitic transformation, this branch shows an anomalous behavior. Therefore, our aim is to investigate the behavior of acoustic TA_2 branch along $[\xi\xi0]$ direction. The most important features in the dispersion curves are the anomalous dips of the acoustic TA_2 branches where the phonon frequencies become imaginary, suggesting instabilities in the cubic austenite structures leading to stable martensitic phases through phase transformations in all the four materials. In Mn_2NiGa and Mn_2NiAl, the acoustic TA_2 branches have negative slopes at Γ point, indicating a pure elastic instability in their parent structures. The range of this instability extends up to ξ= 0.50 for Mn_2NiGa and up to ξ= 0.35 for Mn_2NiAl. The maxima of the dips in the TA_2 occur at wave vectors ξ= 0.35 and ξ= 0.25 for Mn_2NiGa and Mn_2NiAl, respectively. For Mn_2NiIn, the instability of TA_2 branch starts from ξ= 0.3 producing maximum of the dip at wave vector ξ= 0.50. For Mn_2NiSn, unlike the other materials, the softening extends up to the wedge of the Brillouin zone with the maximum of the dip at ξ= 0.50.

In previous studies of lattice dynamics on ternary MSMAs with Heusler structures, phonon anomalies of TA_2 were correlated with the precursor phenomenon prior to the martensitic phases when the systems are cooled from high temperatures. The wave vectors corresponding to the imaginary phonon frequencies indicated shuffling of atomic planes which stabilize the $(c/a)< 1$ phases compared to the parent phase ($(c/a)= 1$). The occurrence of 3M, 5M and 7M modulated structures and even incommensurate structures were confirmed experimentally. Possibilities of such modulated structures can be inferred from the anomalies in our calculated dispersion relations for Mn_2NiX systems. A modulated structure with a periodicity of 8 atomic planes (2M structure) can be associated with an instability at ξ= 0.25, one with a periodicity of 6 atomic planes (3M structure) can be associated with an instability at ξ= 0.33 and one with a shuffling of 14 atomic planes (7M structure) can be associated with an instability at ξ= 0.29. For Mn_2NiAl, the unstable mode occurs between ξ= 0.0 and ξ= 0.35 with the maximum of the dip at ξ= 0.25. This suggests the possibilities of occurrence of several modulated phases. The commensurate wave vector closest to the maximum of the dip in the TA_2 branch of Mn_2NiGa occurs at ξ= 0.33 which can be related to the occurrence of the 3M structure. Since, in Mn_2NiGa, the imaginary frequencies extends up to ξ= 0.50, in addition to aforementioned modulated structures 5M, modulation can also be observed at ξ= 0.43 which stabilizes with the shuffling of 10 atomic planes. In cases of Mn_2NiIn and Mn_2NiSn, the

maxima in the dip of the TA_2 branch occur at ξ= 0.5, which although cannot be connected to the known modulated structures mentioned above, but the extent of the instabilities in these systems can be connected to the 3M and 5M modulations. These suggest possibilities of occurrence of new kinds of modulations leading to precursor phenomena in these materials or that there may be more complicated structures with co-existence of multiple modulated phases. Signatures of 7M modulated phases have been observed experimentally [105, 106] in Mn_2NiGa, but the occurrences of these were either dependent on the amount of stress in the system [106] or on the sublattice occupancies [105]. Thus, no definite conclusion on the kind of modulation in this system and the resulting pre-martensitic structures can be made from the available experimental results. Detailed systematic calculations on the non-cubic variants for these systems are to be carried out in order to settle the issue. However, this is beyond the aim and scope of the present study.

Energetically lowest optical T_{2g} branch is Raman active in nature with [$\xi\bar{\xi}$0] polarization and the other optical branches are infrared active with T_{1u} symmetry. It is known that phonon branches with same symmetry would repel each other. Since, acoustic TA_2 branch also has same state of polarization; it would be repelled by the T_{2g} branches. In a previous theoretical study, Zayak *et al.* [212] argued that due to this repulsion the TA_2 branch is pushed downward and becomes unstable. To prove this, they compared the position of T_{2g} branches at Γ point of some stable Heusler alloys at cubic phase like Co_2MnGa and Co_2MnGe to unstable systems like Ni_2MnX (*X*= Ga, Ge, In, Al) and illustrated that energetically lowered T_{2g} branches in the unstable alloys compared to those alloys with stable cubic phases, produce the necessary repulsive thrust to the lowest vibrational branch. The results in F 6.5 suggest the same explanation for the phonon instabilities in Mn_2NiX. The repulsion due to the already low lying T_{2g} modes at the Γ point for all four materials push the TA_2 frequencies down setting up the unstable modes. In Reference [212], the authors attributed the occurrence of anomalous unstable modes in Ni_2MnGa to the inversion of modes of Ni and Ga. They showed that the contributions to the T_{2g} branches come from the dynamics of Ni atoms and due to the inversion of optical modes, the Ni atoms vibrate at lower frequencies making the frequencies of the T_{2g} mode lower. The repulsion of TA_2 modes by these T_{2g} modes pull the frequencies of the former down making them imaginary. For the materials investigated here, an analysis of the vibrational amplitudes show that the T_{2g} modes are dominated by the vibrations from Ni and MnI atoms who occupy crystallographically equivalent sites, and in fact the same ones as the two equivalent Ni atoms in Ni_2MnGa. Therefore, it would be interesting to examine

whether such an inversion of optical mode is also happening for these materials. In the next subsection, we explore this by looking at the vibrational densities of states (VDOS).

4.3.2 Vibrational Density of States (VDOS)

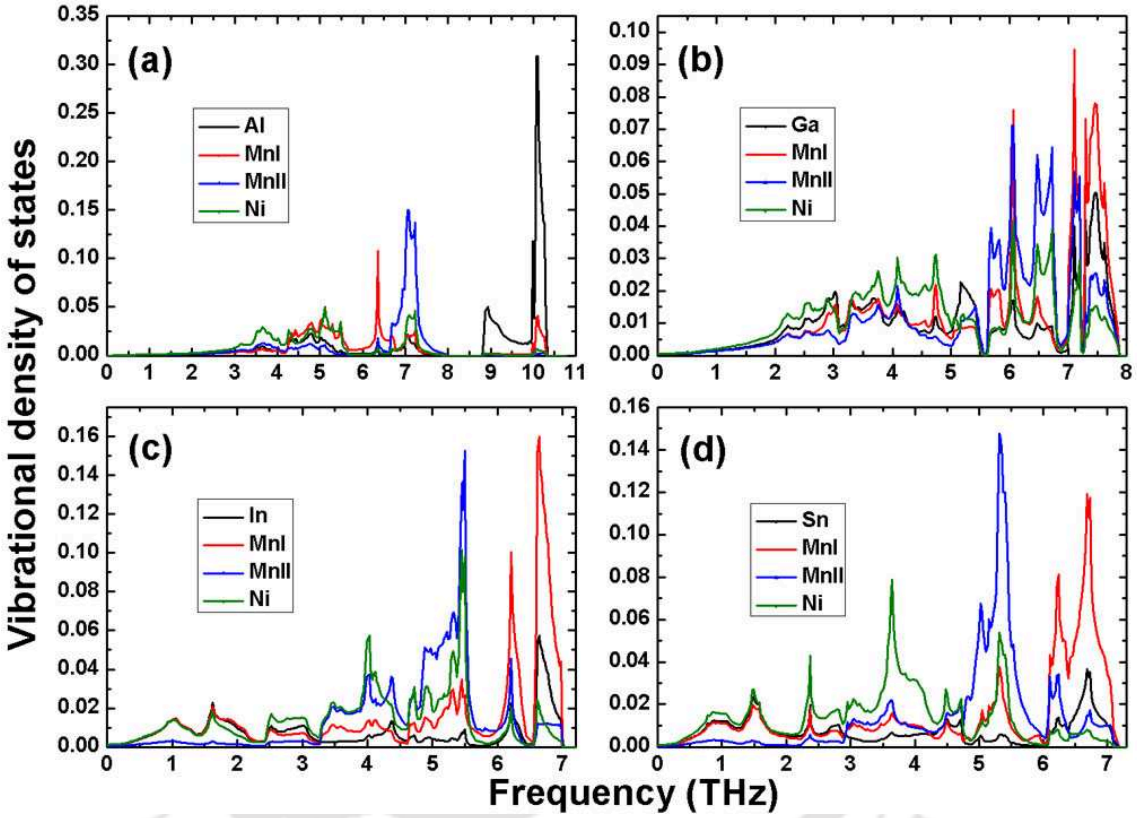

F 4.2: Atom projected vibrational density of states (VDOS) showing contributions from different constituent atoms for (a) Mn_2NiAl, (b) Mn_2NiGa, (c) Mn_2NiIn and (d) Mn_2NiSn over the frequency range [202].

In what follows, the atom projected VDOS for Mn_2NiAl, Mn_2NiGa, Mn_2NiIn and Mn_2NiSn are presented in F 4.2. It is observed that the vibrational contributions from two Mn atoms occupy different frequency regions in the VDOS plots. This occurs mainly because of the following reasons: the two Mn atoms have different crystallographic symmetry; the atom occupying (0,0,0) sublattice, labeled as MnI, have tetrahedral symmetry and the other one at (0.25,0.25,0.25), labeled as MnII, sublattice have octahedral symmetry; as a consequence of this their nearest neighbor environments are different leading to different bond stiffnesses (force constants) for the bonds connected to the Mn atoms. A comparison of all the VDOSs

show that the VDOSs of Mn_2NiIn and Mn_2NiSn materials are quite similar and are very different from the VDOSs of the other two materials in the series. F 4.2 suggests that for Mn_2NiIn and Mn_2NiSn, vibrations of MnI atoms are prominent between 6 THz to 7 THz, whereas contributions from MnII atoms are predominantly lie between 4.5 THz to 6 THz. Due to the slightly larger atomic mass than Mn atom, Ni vibrations occur mostly between 2.5 THz to 4.5 THz. As expected, the lower frequency regions are dominated by In and Sn because they have larger atomic masses than Ni and Mn. For Mn_2NiGa, vibrations in the range 7 THz to 8 THz are mainly dominated by MnI atoms, while vibrations from 5.5 THz to 7 THz have contributions from MnII atoms. A strong peak originating from MnI vibrations coinciding with a peak originating from vibrations of MnII atoms is also observed at 6 THz. In the frequency range 3 THz to 5 THz, vibrations of Ni atoms are predominant and the lowermost part of the spectrum is dominated by the vibrations of the Ga atoms. The features in the VDOS of Mn_2NiAl are different than the other three. The modes due to the vibrations of Al atoms occur at around 10 THz due to extremely light mass of Al. The Ni modes also occur at lower frequencies, similar to the cases of the other three. The vibrations of MnI and MnII atoms dominate the middle of the spectrum with their respective peaks at 6.25 THz and 7.3 THz. In case of Ni_2MnGa, Zayak *et al.* [212] showed that the positions of Ga and Ni contributions to the VDOS were "inverted", that is, the vibrations of the lighter Ni atoms were at frequencies lower than those of heavier Ga atoms. They connected this anomalous mode inversion to the instability of the TA_2 modes of Ni_2MnGa. In case of the systems studied here, the overall features in the VDOSs of all four materials suggest that there is no signature of inversion of Ni (MnI) modes with those of the modes from the element *X*. Thus the occurrence of unstable TA_2 modes cannot be associated to this.

4.3.3 Inter-atomic force constants

In order to understand the features in the VDOS, we analyze the behavior of the real space interatomic force constants. In F 4.3, we plot the longitudinal component of nearest neighbor force constants of Mn_2Ni*X* systems. The transverse components of force constants are not shown in the plot, since; their contributions compared to the longitudinal ones are negligible. The force constants between any pair of nearest neighbor atoms are nearly equal for Mn_2NiAl with Mn_2NiGa. Same is true for Mn_2NiIn with Mn_2NiSn. However, substantial changes in the force-constants between any pairs are observed as one move from Mn_2NiGa to

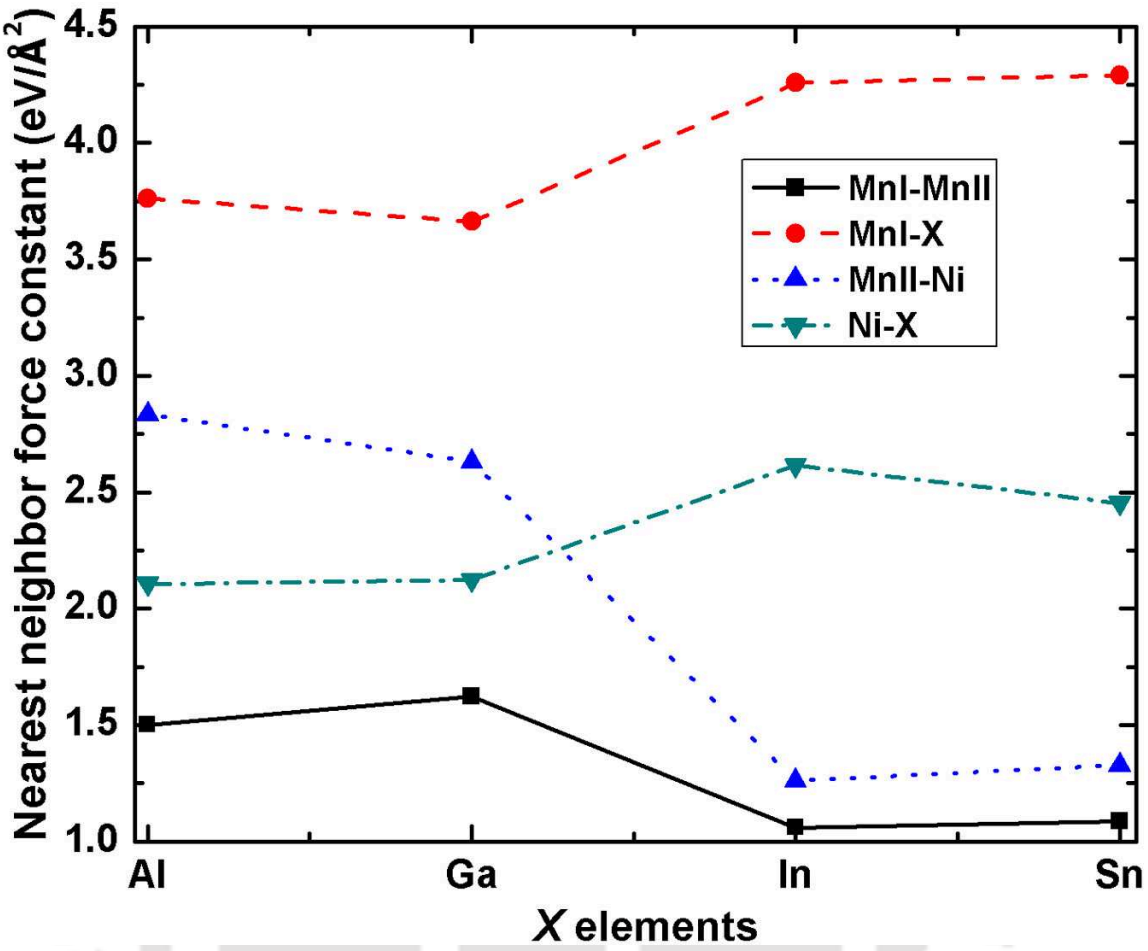

F 4.3: Longitudinal component of nearest neighbor inter-atomic force constants between MnI, MnII, Ni and *X* atoms of Mn_2Ni*X* materials [202].

Mn_2NiIn. Due to the increase in the inter-atomic distances, as a result of expansion in their equilibrium lattice constants from 5.850 Å to 6.162 Å, the MnI-MnII and MnII-Ni longitudinal force constants become softer in Mn_2NiIn and Mn_2NiSn in comparison to Mn_2NiGa. On the other hand, the force constants related to *X* elements, i.e., MnI-*X* and Ni-*X* become harder in Mn_2NiIn and Mn_2NiSn as compared to those in Mn_2NiGa and Mn_2NiAl. This opposite behavior is observed since the sizes of the *X* elements for the former two alloys are larger than those in the later two, and thus are able to overcome the expansion of the inter-atomic distances occurring in the former two as compared to the later two. The nearest neighbor force constants associated to MnII atom, the MnII-Ni and the MnII-MnI, become softer as one moves from Mn_2NiGa to Mn_2NiIn and Mn_2NiSn. Therefore, vibration frequencies corresponding to MnII atoms would be lower in the later two materials, which agree with the features in the VDOS. In Mn_2NiGa, vibrations of MnII extend from 5.5 THz to 7 THz, which

in case of Mn_2NiIn and Mn_2NiSn shift to lower frequencies, around 5.5 THz. The dynamical behavior of MnI and Ni atoms are more complicated. For both of the atoms, two sets of inter-atomic force constants behave opposite to one another. For Ni, the Ni-*X* nearest neighbor force constants hardens, as one goes from Ga to In and Sn. This should force Ni atoms to vibrate at higher frequencies as one goes from Mn_2NiGa to Mn_2NiIn and Mn_2NiSn. However, the vibrations of Ni atom remain more or less around the same frequency for all the materials, since the previous effect is compensated by increasing softening of the MnII-Ni bonds as one goes from Mn_2NiGa to Mn_2NiIn and Mn_2NiSn. Similarly, hardening of MnI-*X* force constant does not affect MnI vibrations, as this is compensated by the softening of MnI-MnII inter-atomic force constants.

4.3.4 Fermi surfaces

Previous first-principles studies in Ni_2MnX relate the martensitic instability of those materials with Fermi surface nesting [212–216]. The anomalies in the phonon branch mainly depend on the shape of the Fermi surfaces and the electron-phonon matrix elements via the phonon wave vector ξ [214, 215]. This phenomenon occurs due to strong attraction between two flat-parallel Fermi surfaces connected by a nesting vector q, at the expense of atomic displacements and at the wave vector where the maximum dip of the acoustic phonon branch is observed. However, this cannot be generalized for all ternary alloys showing martensitic instabilities. For Co_2NiGa, a newly found shape memory alloy, Siewart *et al.* [217] observed that softening in TA_2 phonon branch was absent as a result of nonappearance of nesting features in the Fermi surfaces of Co_2NiGa.

Here, we present Fermi surfaces corresponding to the spin-minority bands only, since most prominent features are observed in this spin channel as the systems undergo martensitic transitions [177]. The three dimensional Fermi surfaces of Mn_2NiGa for 18th and 19th spin-minority bands are shown in F 5.4. The figure clearly exhibits flat portions of both the minority bands. However, to examine the Fermi surfaces in details, to obtain clues about the nesting between different parallel Fermi surfaces and hence, to relate this novel feature to observed phonon anomaly, two dimensional (2D) projections are necessary. In F 4.6, we show two different cross-sections of Fermi surfaces for Mn_2NiX alloys. The cross-sections for Mn_2NiGa, Mn_2NiAl and Mn_2NiSn bear close resemblances while that of the Mn_2NiSn is

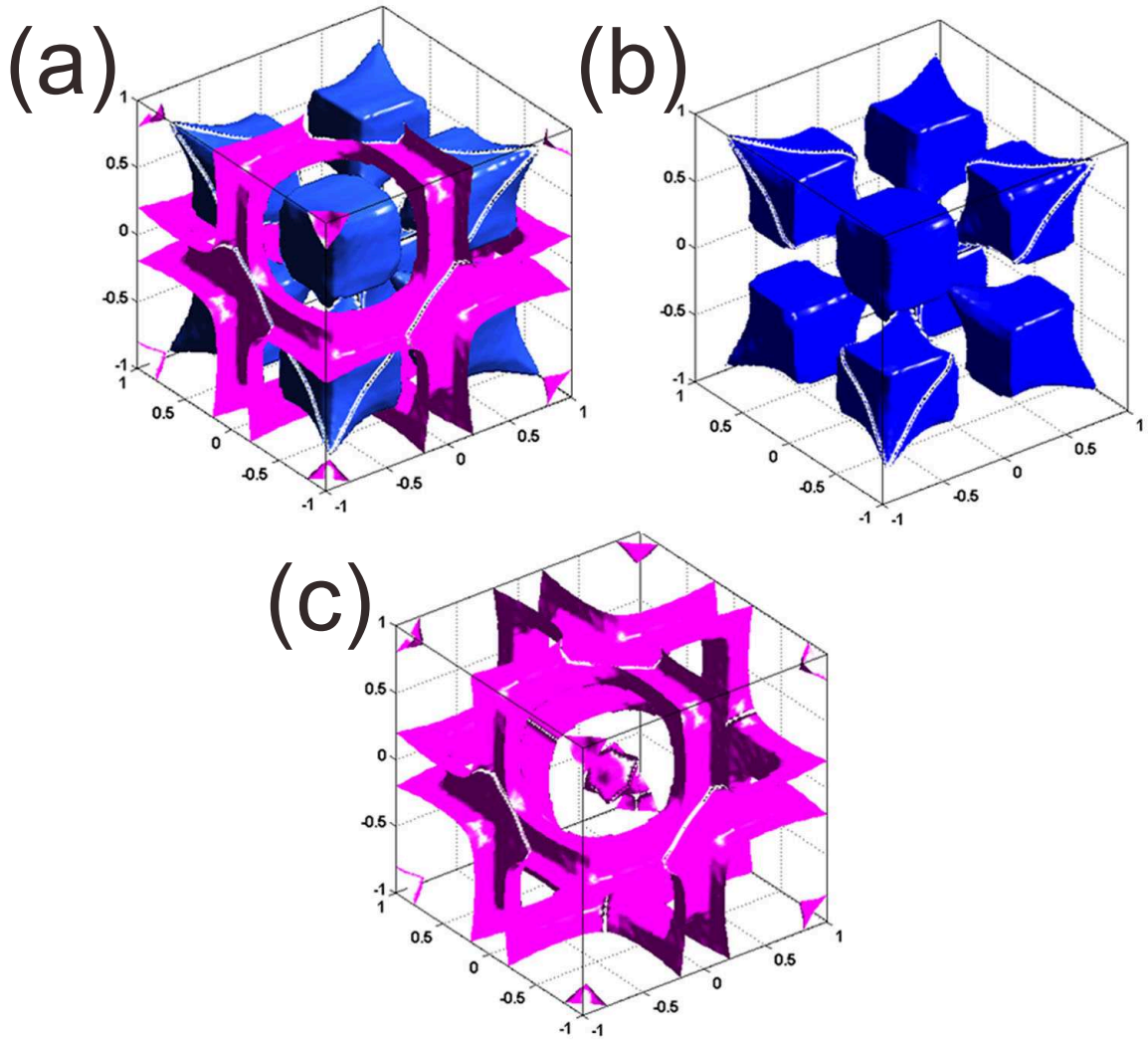

F 4.4: (a) Topology of 3D Fermi surfaces for Mn_2NiGa. The blue and magenta surfaces represent 18^{th} and 19^{th} spin-minority bands, respectively. Panel (b) and (c) illustrate those spin-minority 18^{th} and 19^{th} bands separately [202].

somewhat different. In spite of this difference, the nesting vectors (indicated by red arrows in Fermi surfaces plots) are consistent with the wave vectors at which the phonon anomalies are observed in our phonon dispersion curves. Thus, we can conclusively associate the occurrences of unstable modes in the Mn_2NiX alloys with the Fermi surface nesting. We refrain from further discussions on the differences in shapes of Fermi surfaces between materials with the element X belonging to different columns in the periodic table because it is not necessary in the present discussion where the focus is on to establish the nesting features in the Fermi surfaces and their relations to the martensitic instabilities found in these systems.

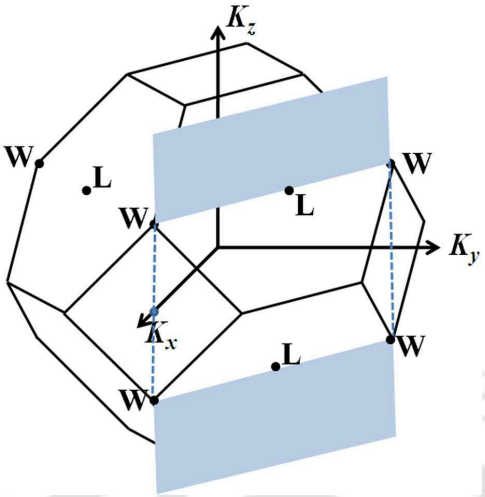

F 4.5: Illustration of the 110 cross section (k_x+k_y= 1) in FCC irreducible Brillouin zone (IBZ) [202].

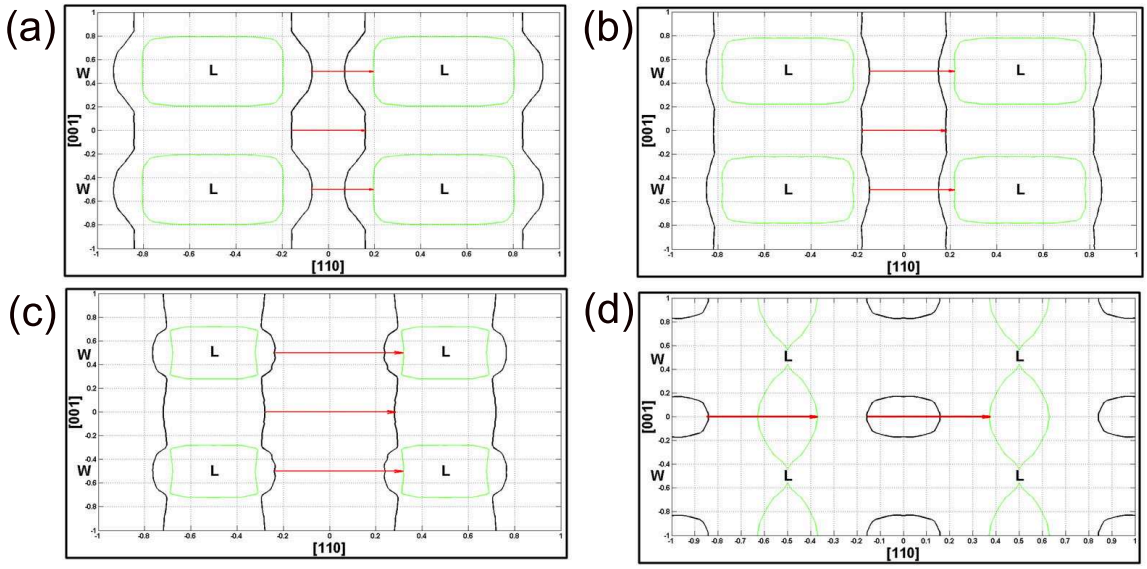

F 4.6: 2D cross section of the Fermi surfaces with the (110) plane k_x+k_y= 1 for (a) Mn_2NiAl, (b) Mn_2NiGa, (c) Mn_2NiIn and (d) Mn_2NiSn. The green and black lines indicate spin minority bands. The red arrows indicate nesting vectors **q**= 0.25(110) for Mn_2NiAl, **q**= 0.35(110) for Mn_2NiGa and **q**= 0.50(110) for Mn_2NiIn and Mn_2NiSn [202].

Barman *et al.* [178] also computed the Fermi surfaces of Mn_2NiGa. They observed nesting in the majority spin Fermi surfaces along (001) and (110) direction in the martensitic phase. They attributed this to the possible instabilities in the TA_2 phonon mode. However, they did not substantiate this by computations of the phonon spectra. Our results are qualitatively different from theirs as we found nesting along (110) direction in the austenite phase.

Moreover, our results are consistent as the Fermi surface nesting along (110) could be related to the computed instabilities in the TA_2 phonon mode along (110) with the nesting vector computed from the Fermi surfaces agree with the wave vector at which the maximum of the instability occurs.

4.3.5 Elastic constants

T 4.1: Calculated elastic constants and elastic anisotropy ratio for Mn_2NiX materials. Experimental elastic constants are only available for Mn_2NiGa and shown in brackets [202].

Systems	c′ (GPa)	c_{11} (GPa)	c_{12} (GPa)	c_{44} (GPa)	A (=c_{44}/c')
Mn_2NiAl	-33.13	100.35	127.19	131.66	-3.97
Mn_2NiGa	-13.42	58.91 (90.55)*	125.17 (128.00)*	111.00 (124.42)*	-8.27
Mn_2NiIn	16.44	118.64	85.76	41.47	4.96
Mn_2NiSn	15.43	146.05	115.19	64.27	4.17

*ref. [218]

The dynamical stability of crystalline phase implies that the strain energy changes be positive definite against all possible small deformations. This condition imposes restrictions on elastic constants. The stability criteria for cubic crystals requires [219]

$$c_{44} > 0, c_{11} > |c_{12}|, c_{11} + 2c_{12} > 0 \tag{4.10}$$

Therefore to introspect the kinds of instabilities present in the materials considered here and to validate our calculated phonon dispersion results, we compute the elastic constants for all the four materials from the initial slope ($\xi \to 0$) of phonon dispersion plots along [$\xi\xi$0] direction. The elastic constants c_{44}, c′ (=$\frac{1}{2}(c_{11}-c_{12})$) and c_L (=$\frac{1}{2}(c_{11}+c_{12}+2c_{44})$) are related to TA_1, TA_2 and LA acoustic modes [219]. These elastic constants are connected to ultrasound velocity via $c_{ij}=\rho v^2$ relation [219] where ρ is the mass density. The three independent elastic constants of cubic crystal are tabulated in T 4.1. Our computed c_{12} and c_{44} agree quite well with the experimental results available only for Mn_2NiGa, whereas in our calculation, c_{11} is underestimated [218]. Overall the agreement with experiment is good for Mn_2NiGa. This, in effect, is an indirect indication to the accuracy of calculated phonon spectra. The results show that the equation 4.10 is satisfied by Mn_2NiIn and Mn_2NiSn only. This indicates that Mn_2NiAl

and Mn_2NiGa are unstable in the cubic structure. We gain further insight into the nature of stabilities of these materials by looking at the other two parameters listed in T 4.1, the shear constant and the elastic anisotropy ratio. Since acoustic TA_2 branch is related to shear constant (c′), hence, negative c′ for Mn_2NiAl and Mn_2NiGa is an indication of pure elastic instability which stabilizes though shear deformation across ($\xi\xi 0$) planes in [$\xi\bar{\xi}0$] direction. The same is not true for the other two materials. Although they satisfy equation 4.10 and have sizable c′, their anisotropy ratios A are high enough to effect a martensitic transformation [220]. The elastic anisotropy ratio A (=c_{44}/c') is an important quantity to measure of stability of cubic structures under stress across ($\xi\xi 0$) planes [86]. Larger the value it acquires, more unstable the structure becomes. For systems undergoing martensitic transformations, the value of A varies from 2 onwards [207, 220–224]. In cases of Mn_2NiIn and Mn_2NiSn, the values of A lie well within the limits observed in shape memory alloys. The origin of this could be rather small value of the shear modulus c′. Additionally, we find that c_{44} in cases of Mn_2NiIn and Mn_2NiSn are much softer than those for the other two materials. The comparative softening in c_{44} for Mn_2NiIn and Mn_2NiSn as compared to Mn_2NiGa and Mn_2NiAl, indicate that the cubic Mn_2NiIn and Mn_2NiSn will transform to different martensitic phases compared to the other two where the transformations would be driven by softening in c′ as has been observed in cases of other shape memory alloys [220]. The results on elastic constants therefore corroborate the inferences drawn from the differences in dispersion relations for the materials studied.

The vibrational and elastic properties discussed in this work show a clear trend. Mn_2NiGa and Mn_2NiAl are quite similar in their behaviors; same goes for Mn_2NiIn and Mn_2NiSn. The vibrational and elastic properties among these two groups are significantly different. The origin of such differences can be traced back to the differences in their electronic structures [177]. The signatures of mechanical instability were reflected in electronic structures of Mn_2NiGa and Mn_2NiAl, where high densities of states, as compared to Mn_2NiIn and Mn_2NiSn, were found at the Fermi level. The origin of this was larger hybridizations between the Mn and Ni atoms at the octahedral positions for the former two systems. For the latter two systems, rather small densities of states at Fermi level, due to smaller hybridizations between the magnetic atoms at octahedral positions, originating from larger distances between those magnetic atoms (due to the atoms sitting in a larger lattice compared to the former two which happens as In and Sn have larger sizes than Ga and Al), signified that it would take external influences to induce instabilities into these systems.

4.4 Summary

In this chapter, we have investigated the lattice dynamics of Mn_2NiX (X= Al, Ga, In, Sn) MSMAs in their austenite phase. The calculated phonon spectra show anomalous behavior of the acoustic TA_2 branch along [$\xi\xi$0] direction for all the four materials indicating structural instability. Instabilities in the said acoustic mode can be related to the repulsion by the optical T_{2g} mode posing the same symmetry as the TA_2 mode. Unlike Ni_2MnGa, no inversion of optical modes could be observed, thus ruling this out as one of the possible mechanisms behind the anomalous features in phonon spectra. The features in the vibrational densities of states can be explained from the qualitative variations of the interatomic force constants across the materials. The calculated elastic constants corroborate the structural instabilities inferred from phonon dispersion relations. Negative shear constants for Mn_2NiAl and Mn_2NiGa indicate pure elastic instabilities in these materials. Finally, the nesting features in the Fermi surfaces confirm that the observed phonon anomalies are associated with them. The wave vectors at which the maximum anomaly occur indicate the possibility of formation of pre-martensitic modulated phases which are yet to be confirmed by experiments. The results also indicate that these modulated pre-martensitic phases could be quite complex and further investigations into this aspect is necessary.

Chapter 5

Investigation of the magnetic structure of Mn_2NiX materials from the study of noncollinear magnetism* †

5.1 Introduction

The total magnetic moments calculated in chapter 3 for Mn_2NiX materials are based upon the assumption that the magnetic structure is collinear. Till now, no theoretical and experimental investigations have been made to study the possibility of observing noncollinear structures as magnetic ground states in these materials. Contrast to the collinear spin structure, in non-collinear spin configuration, the spin quantization direction rotates from one atomic plane to another in bulk materials, thus forming a periodic helix like structure. In 1988, Y. Tsunada first observed the noncollinear spin spiral structure and explained his neutron diffraction results on FCC $Fe_{97}Co_3$ alloy precipitate in Cu [226] based upon the observation. This experimental finding stimulated many first-principles based spin spiral studies mainly in bulk materials. In the early 90's, the existences of spin spiral structures are theoretically investigated in the context of high-T_c superconductors, using the framework of Hubbard model, where the stabilizations of the spin spiral states are realized within a wide range of the parameters of the

*Contents of this chapter are mostly taken from Ref. [225].

†Permission from the publisher has been obtained for reprints of Ref. [225].

model [227–231]. Materials exhibiting complex magnetic exchange interactions, for example, in spin glasses [232–237], substitutional alloys [238–243] and systems with geometrical frustrations such as α and β phase of Mn, can have stable spin spirals structures as their ground states [244–248]. The appearances of noncollinear magnetic states, either in ambient condition or under external influences, such as under pressure, have given rise to interesting properties in these materials. For example, Iron, the most common ferromagnet, orders ferromagnetically at ambient condition in BCC structure. Under external pressure it undergoes a phase transformation to HCP structure which is believed to be nonmagnetic. Lizaárraga *et al.* had studied the later structure under high-pressure and showed that two different antiferromagnetic structures along with a nonsymmetric spin spiral structure coexist in the ground state [249]. A transition to noncollinear magnetic state under pressure has been shown to be the driving mechanism behind the inver properties of Pd_3Fe under external pressure [250]. Similarly, an Fe(110) monolayer undergoes a phase transition from collinear to a noncollinear spin spiral state under an in-plane strain [251]. Pressure driven noncollinear magnetism was also discussed for MnAs in a zinc-blende structure [252]. Based on the study of $NdNiO_3$ and other rare earth nickelates, Prosandeev *et al.*, predicted that a phase transformation between insulating spin-density wave (SDW) and metallic spin spiral states can be induced by epitaxial strain [253]. These results demonstrate that it is important to investigate the ground state magnetic structure of new functional materials which are supposed to be useful in applications involving magnetic degrees of freedom.

Any evidence of occurrences of noncollinear magnetic structure is not reported for Ni_2MnX MSMAs. To understand the magnetic interactions deeply and their influences on the properties related to MSME, Enkovaara *et al.* [254] calculated the energies of the noncollinear spin spirals in Ni_2MnAl and Ni_2MnGa within the framework of DFT. Their calculations conclusively showed that the ground state magnetic structures in these two materials are ferromagnetic. References [244–248] and [252] have shown that the prominent presence of Mn can drive noncollinear magnetic structure. Since the systems studied in this thesis have more Mn than the other magnetic constituent, and that the Mn atoms are crystallographically inequivalent, it becomes important to explore whether such a chemical composition can lead to magnetic structures other than simple collinear types. It also becomes important to explore the role of the crystal structure, i.e., whether a particular arrangement of magnetic atoms plays a role in sustaining noncollinear magnetic states. Also the role of external factors like pressure on the magnetic ground state is to be looked into. In this chapter, we try to find out answers

to these questions by computing the relative stabilities of noncollinear states (planar spin spirals) for the four Mn_2NiX materials. We explain our results in terms of the band structures, the Fermi surfaces and the magnetic exchange interactions.

5.2 Computational Details

Total energies and band structures of the collinear and the spin-spiral states are calculated by the first-principles Full-Potential Linearized Augmented Plane Wave (FP-LAPW) method as implemented in E code [183–185]. To calculate the energies of various noncollinear states as accurately as the collinear states, the symmetry of the helical spin structure along the *z*-axis with the spiral wave vector **q** has to be incorporated. However, the parallel spins within two consecutive planes rotate around an angle ϕ= **q.R** along the spiral axis. Since we are only interested on the transverse component of spin wave, the angle θ, representing the deviation of spin quantization direction with the wave vector **q**, is considered to be 90° which gives minimum contribution to the total energy. Since noncollinearity breaks the translation symmetry of the material, periodic Bloch boundary conditions are no longer valid. In this situation, large supercell can be constructed to replicate the spin spiral waves within the material, where large computational facility would be involved. One way to circumvent this problem is to introduce a generalized translation which would preserve translation symmetry in real space and rotational symmetry in spin space, leaving the magnetic density invariant as

$$m(\mathbf{r} + \mathbf{R}) = D(\mathbf{q}.\mathbf{R})m(\mathbf{r}) \tag{5.1}$$

where **R** is a Bravis lattice vector and D**(q.R)** is a matrix which rotates the in-plane component of m by an angle **q.R** along the *z*-direction. Therefore, the Blöch spinor can be written as

$$\psi_k(\boldsymbol{r}) = e^{i\boldsymbol{k}.\boldsymbol{r}} \begin{pmatrix} e^{-i\boldsymbol{q}.\boldsymbol{r}/2} u_k(\boldsymbol{r}) \\ e^{+i\boldsymbol{q}.\boldsymbol{r}/2} d_k(\boldsymbol{r}) \end{pmatrix} \tag{5.2}$$

where ***k*** is a vector in the Brillouin zone (BZ) and u_k***(r)*** and d_k***(r)*** are the periodic Blöch functions for spin-up and spin-down components, respectively. Due to this generalized prescription, the spin spirals can be calculated within the chemical cell instead of supercell.

From careful convergence test with respect to Brillouin zone (BZ) sampling and the size of the basis set, we have determined that the plane wave cut-off for the basis set being $R_{MT}K_{max}$= 9, where R_{MT} is the muffin-tin radius and K_{max} is the largest reciprocal lattice vector, which amounts to nearly 350 plane waves. The charge density cut-off was considered to be G_{max}= 14 and the angular momentum cut-off to the augmented plane wave was taken to be ℓ_{max}= 10. The Brillouin zone (BZ) integrations have been carried out with a **k**-mesh of $11 \times 11 \times 11$ along [00**q**] and [**qq**0] directions and with $15 \times 15 \times 15$ along [**qqq**] direction which effectively result into 726 **k**-points and 680 **k**-points, respectively in irreducible Brillouin zone (BZ). Such choices of parameters ensure the convergence in self-consistent total energy with less than 0.1meV per atom.

The magnetic pair exchange interactions have been calculated within multiple scattering Green function formalism as implemented in EMTO code [154–158]. Spin fluctuation theories for metals map the complicated itinerant electron systems onto an effective Heisenberg Hamiltonian having the classical spins as

$$H_{eff} = -\sum_{\mu,\nu}\sum_{i,j} J_{ij}^{\mu\nu}\mathbf{e}_i^{\mu}.\mathbf{e}_j^{\nu} \tag{5.3}$$

The indices μ and ν represent different sublattices, i and j denote the atomic positions and $\mathbf{e}_i^{\mu}$ is the unit vector along the direction of magnetic moments at site i belonging to sublattice μ. The size of the magnetic moments are included in the exchange interaction parameter $J_{ij}^{\mu\nu}$. The exchange parameters are computed from energy difference due to the small orientation of a pair of spins result a perturbation in spin-density which within the formulation of Lichtenstein *et al.* [255, 256] based on magnetic force theorem [257] takes the following form

$$J_{ij}^{\mu\nu} = \frac{1}{4\pi}\int_{-\infty}^{E_F} d\epsilon \Im \mathrm{Tr}(\Delta_i \hat{T}_{\sigma}^{ij}\Delta_j \hat{T}_{\sigma'}^{ji}) \tag{5.4}$$

where $\Delta_i = \hat{t}_{i\sigma}^{-1} - \hat{t}_{i\sigma'}^{-1}$, σ is the spin index, $\hat{t}$ is the single site scattering matrix and $\hat{T}$ is the scattering path operator related to the off-diagonal elements of the Green function. Tr is the trace over the orbital indices of the scattering matrix. Positive (negative) values for $J_{ij}^{\mu\nu}$ indicate ferromagnetic (antiferromagnetic) coupling between atoms i and j.

For the calculations of $J_{ij}^{\mu\nu}$ in the EMTO method, the Green's function is calculated for 32 complex points distributed exponentially on the semi-circular contour with a diameter of 2.5

Ryd. The Brillouin zone is sampled by a uniform **k**-point mesh of $24\times24\times24$, which ensured convergence of the total energy to less than 0.1 meV per atom.

5.3 Results and Discussions

5.3.1 Spin wave spectra of Mn_2NiX materials in inverse Heusler structure

T 5.1: Lattice parameters of Mn_2NiX systems calculated with LDA and GGA functionals and used in this work. The numbers in the parenthesis indicate the experimental values whenever available. All the calculations are done with FP-LAPW method.

Systems	LDA Equilibrium lattice constant (Å)	GGA Equilibrium lattice constant (Å)
Mn_2NiAl	5.613	5.802
Mn_2NiGa	5.631	5.835(5.907)
Mn_2NiIn	5.919	6.164
Mn_2NiSn	5.924	6.147(6.099)

In this work, we first focus our attentions on the possibilities of noncollinear ground states under the influence of pressure. Therefore, the choices of lattice constants are important. We consider the lattice constants calculated using FP-LAPW method within the GGA exchange-correlation functional and presented in chapter 3 as the good representations of the experimental structures. In order to investigate the effects of pressure on the spin spirals in these materials, we calculate the equilibrium lattice constants with LDA exchange-correlation functional, which are smaller than by about 3.5% than the GGA calculated ones. The choices of the LDA lattice constants make sense as the compressions obtained are such that these can be achieved by standard experiments. The lattice constants used in this work are presented in T 5.1.

In F 5.1, we present the total energies of spin spirals relative to **q**= 0 collinear ferrimagnetic state as a function of the spin spiral vectors **q** in different symmetry directions of the Brillouin zone. The panels represent the energies in different symmetry directions in the inverse Heusler structure. The energies of the spin spirals are calculated at LDA lattice constants, i.e., at compressed lattice constants. The results show that in a compressed lattice, spin

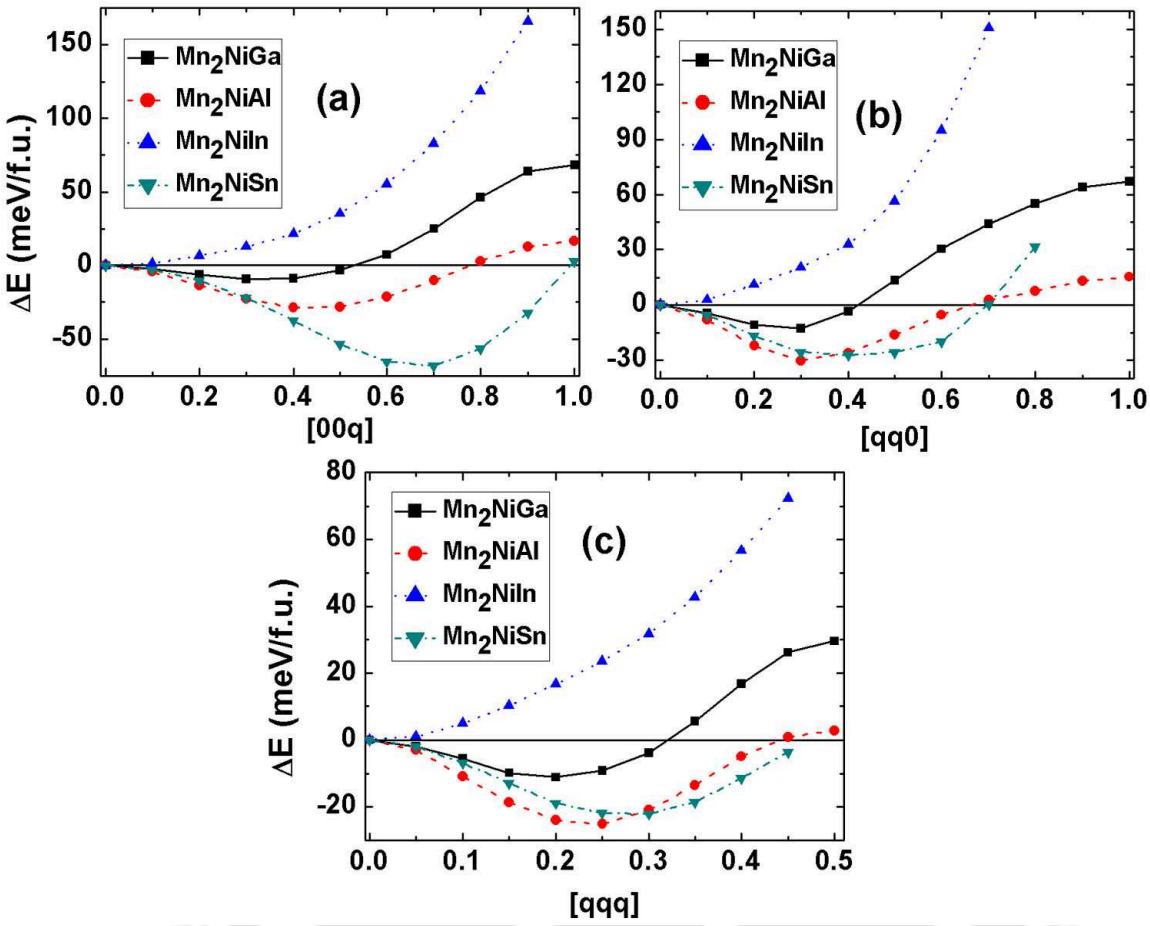

F 5.1: Total energies of Mn_2NiX systems as a function of spin spiral vectors **q** in the inverse Heusler phases. All calculations are done at compressed lattice constants [225].

spiral states are more stable than the collinear ones for Mn_2NiAl, Mn_2NiGa and Mn_2NiSn. Surprisingly, Mn_2NiIn has the **q**= 0 collinear state as the stable one. A careful inspection reveals that the relative stability of the spiral magnetic state with respect to the collinear one decreases as $Mn_2NiAl \rightarrow Mn_2NiGa \rightarrow Mn_2NiIn$ implying that as one goes down the column of *X* elements in the periodic table, the relative stability of the spiral magnetic state decreases. The larger stability of the Mn_2NiSn which has one more electron than Mn_2NiIn suggests that this extra electron has some role in stabilization of the spiral magnetic state.

After calculating the spin spirals at compressed lattice constants, we, now, compute their energies at the GGA lattice constants, i.e., at lattice constants close to the experimental ones. The results are shown in F 5.2. The results clearly suggest that the spiral magnetic states are de-stabilized leading to a collinear state upon increasing the volume, bringing them

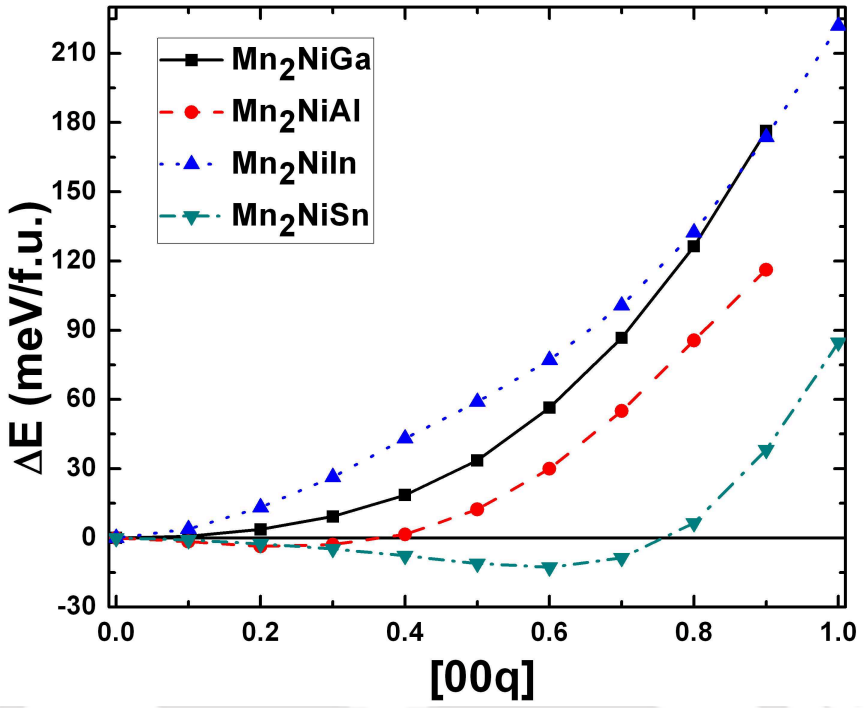

F 5.2: Total energies of Mn_2NiX systems as a function of spin spiral vectors **q** in the inverse Heusler phases. All calculations are done at equilibrium lattice constants [225].

closer to the experimental results. In case of Mn_2NiAl and Mn_2NiSn, although the energies at $\mathbf{q} \neq 0$ are lower than that at $\mathbf{q}= 0$, the energy curves are rather flat and very close to that of the energy zero line, implying that the spiral states are nearly de-stabilized. The results of F 5.2 are in perfect agreement with experiments in case of Mn_2NiGa and Mn_2NiSn where the possibility of a noncollinear magnetic state was never reported. F 5.1 and F 5.2, thus establish that a noncollinear spin spiral state can be observed in Mn_2NiGa, Mn_2NiAl and Mn_2NiSn upon compressing the lattice constant by about 3.5%. In the next two subsections, the origin of sustaining the spin spirals at compressed volumes of the three systems and consequently the reason behind the absence of spin spirals in one of the materials which is isoelectronic with two others are explained from their band structures.

5.3.2 Band Structures and Fermi Surfaces

Based upon their studies on ferromagnets, Lizárraga *et al.* [258] have proposed a mechanism by which a noncollinear structure can be favored in metallic systems. They showed that a noncollinear magnetic state could be stabilized if the two spin channels hybridize, opening up

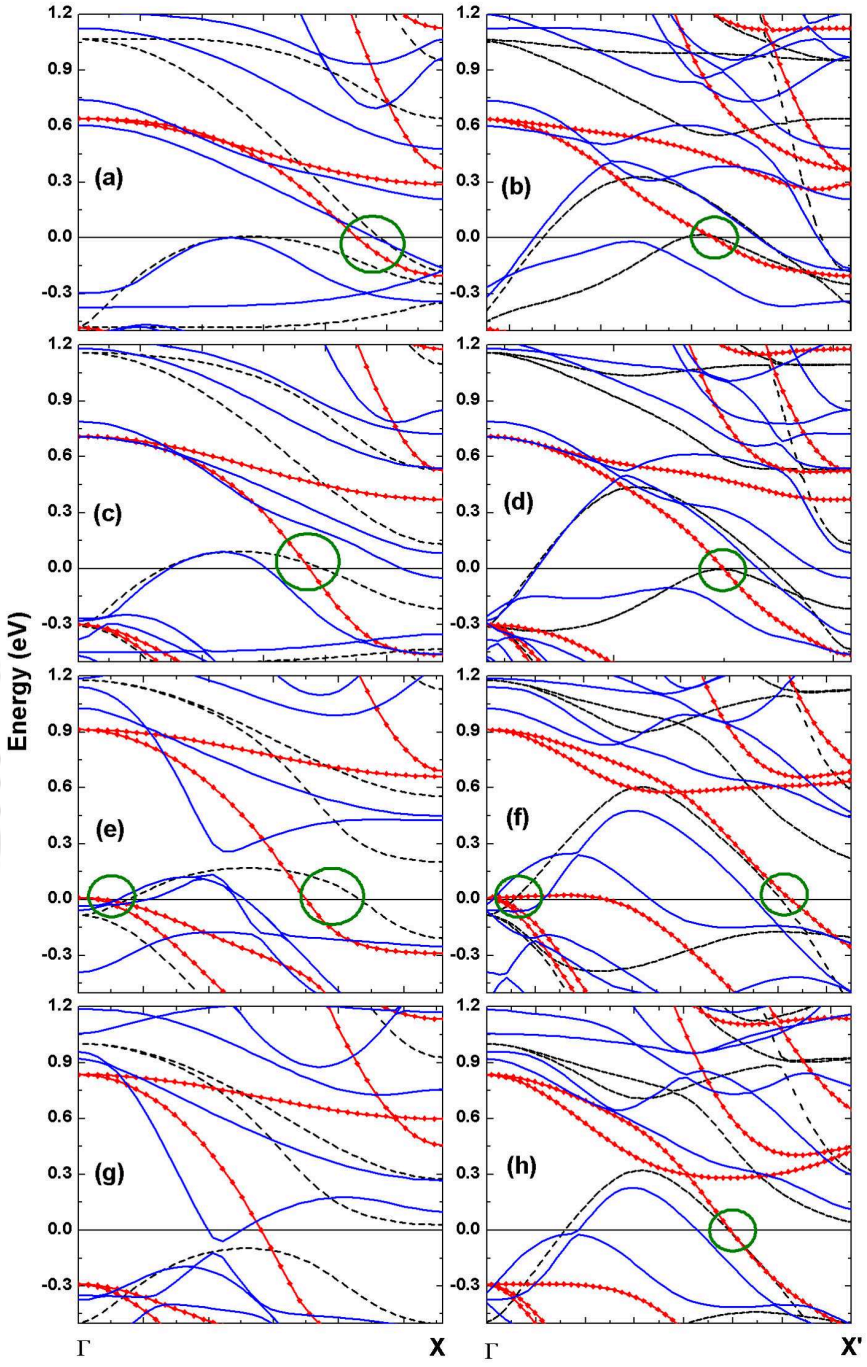

F 5.3: Band structures of (a)-(b) Mn_2NiAl at q= (0, 0, 0.40), (c)-(d) Mn_2NiGa at q= (0, 0, 0.30), (e)-(f) Mn_2NiIn at q= (0, 0, 0.70) and (g)-(h) Mn_2NiSn at q= (0, 0, 0.70) along $\Gamma \rightarrow X$ and $\Gamma \rightarrow X'$ directions, indicated in blue lines. The black and red lines indicate spin majority and spin minority band structure in the collinear (q= 0) state respectively. All the calculations are done at compressed lattice constants.

a hybridization gap at the Fermi level, thus pushing one band up into the unoccupied region and pushing the other band down, lowering the total energy. The criteria required for this mechanism are (i) the Fermi level needs to cut through both the spin states and (ii) nesting features between spin-up and spin-down states in the Fermi surface are formed implying that via a rigid shift in **k**-space, large areas of spin-up Fermi surface can be made to coincide with the spin-down Fermi surface.

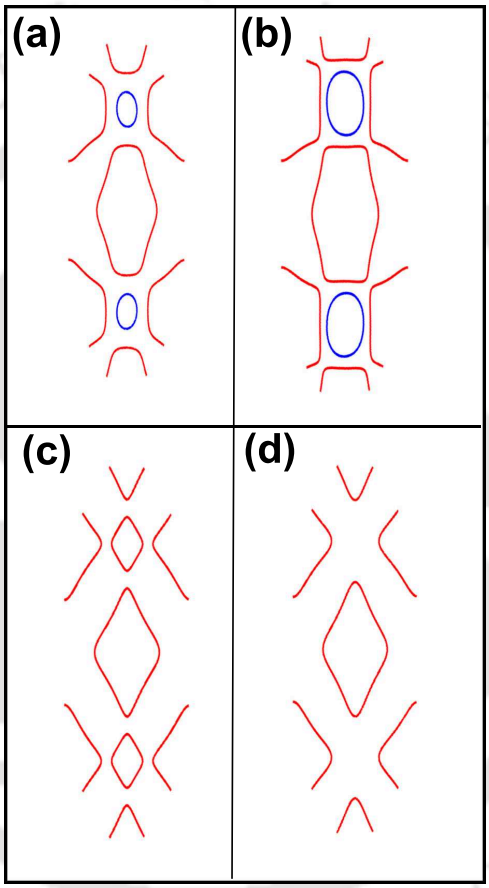

F 5.4: Cross sections of Fermi surfaces in the (001) plane for (a) Mn_2NiGa, (b) Mn_2NiAl, (c) Mn_2NiIn and (d) Mn_2NiGa. Figures (a)-(c) are calculated at compressed volumes of T 5.1, (d) Mn_2NiGa, calculated at GGA volume of T 5.1. The red and blue colors indicate contributions from spin-majority and spin-minority bands, respectively [225].

In F 5.3, we showed the band structures of Mn_2NiAl, Mn_2NiGa, Mn_2NiIn and Mn_2NiSn along $\Gamma - X$ and $\Gamma - X'$ direction calculated at compressed volumes. The band structures of the noncollinear spin spiral states corresponding to the ground state **q** vector along (00**q**) are plotted along with the band structure at **q**= 0 collinear state for Mn_2NiGa,

Mn_2NiAl and Mn_2NiSn. In the case of Mn_2NiIn, an arbitrary **q** value along the same direction is chosen as the spin spiral is not stable at any nonzero wave vector. The circled areas in panels indicate the regions where the Fermi levels cut through both spin-up and spin-down bands. For Mn_2NiSn, in panel (g), we observe that the spin-up band never cuts through the Fermi level. In all the panels, except (g), the hybridizations between spin-up and spin-down bands open gaps, pushing the bands in opposite directions, thereby lowering the energies of spin spirals compared to the collinear state. To see if this mechanism is sustainable, in F 5.4(a)-(c),we present the projections of the Fermi surfaces of Mn_2NiGa, Mn_2NiAl and Mn_2NiIn in the [001] plane calculated at compressed lattice constants. The results show nesting features for Mn_2NiGa, Mn_2NiAl and Mn_2NiSn where sheets of parallel spin-up and spin-down bands are present. Panel (c) shows the case of Mn_2NiIn at its compressed lattice constant. No sign of overlap of different spin channels is observed. Panel (d) represents the Fermi surfaces of Mn_2NiGa computed at GGA lattice constant. For this case also, the spin-up and spin-down Fermi surfaces do not overlap. Therefore, one can immediately conclude that the Fermi surfaces of Mn_2NiGa are modified significantly as the volume is expanded and the nesting features are destroyed as a result of volume expansion. The results of F 5.4 thus suggest that the nesting of spin-up and spin-down bands is a necessary condition for the stabilization of a noncollinear spin spiral state and that the features in the band structure, together with the topologies of the Fermi surfaces, can explain the observed trends in the Mn_2Ni*X* series.

5.3.3 Exchange interactions

In this section, we investigate the more fundamental issue, i.e., the role of the Mn atoms towards the stabilization of the noncollinear spin spiral states. To this end, we calculate the variations of inter-atomic magnetic exchange parameters using Lichtenstein's formula as a function of lattice constants. We observe that the largest contributions come from MnI-MnII inter-sublattice interactions, where MnI is the sublattice with tetrahedral symmetry and MnII is the sublattice with octahedral symmetry. The other inter-sublattice interactions such as the Ni-Mn ones also contribute substantially. However, the reasons behind a stabilized spin spiral magnetic state at a lower volume and its subsequent destruction at a higher volume, as has been observed for three alloys studied along with the nonoccurrence of any spin spiral state despite compression in the case of Mn_2NiIn cannot be explained from the inter-sublattice

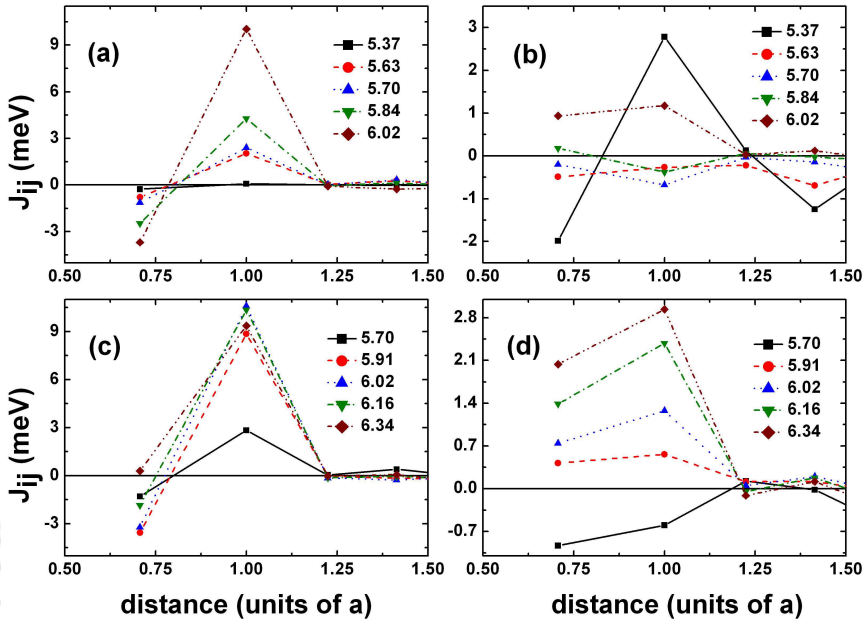

F 5.5: Interatomic intra-sublattice exchange interaction parameters for MnI (left panels) and MnII sublattices (right panels) calculated at different volumes (lattice constants shown in Å). The top panels ((a) and (b)) are for Mn_2NiGa and the bottom ((c) and (d)) panels are for Mn_2NiIn [225].

exchange parameters, as their variations with the volumes are identical across the materials. Significant deviations in behavior are, however, observed in the cases of intra-sublattice interactions associated with the two Mn sublattices. In F 5.5, we present the MnI-MnI and MnII-MnII exchange parameters as functions of lattice constants for Mn_2NiGa and Mn_2NiIn. Panels (a) and (c) show the intra-sublattice exchange parameters for MnI sublattice in the cases of Mn_2NiGa and Mn_2NiIn respectively and there is little difference in qualitative variations with lattice constants for these two alloys. Panels (b) and (d) present the same information, but for the case of the MnII sublattices. The occurrence of a noncollinear state is expected when there is magnetic frustration in the sublattice concerned. In the case of Mn_2NiIn (panel (d)), one sees that, for lattice constants starting with 5.91 Å and higher, the MnII intra-sublattice interactions are all ferromagnetic. This explains why a noncollinear spiral state is not observed at all, even after about a 3.5% compression of the lattice constant. On the other hand, the results for lattice constants starting with 5.63 Å and higher in panel (b) suggests that, until about 5.70 Å, the first few MnII-MnII neighbors are antiferromagnetically coupled, which introduces frustrations in this sublattice. Moreover, the strengths of the

interactions are of comparable magnitude and thus introduce a noncollinear state. For an enhanced lattice constant of 5.84 Å, this frustration is released as the nearest-neighbor exchange interactions become ferromagnetic, while the next nearest-neighbor interactions remain antiferromagnetic, explaining the reason behind the destruction of the spin spiral states at a larger volume. Another interesting observation in panel (d) is that upon further compression of the Mn_2NiIn system, the MnII-MnII exchange interactions all become antiferromagnetic, thus setting in a magnetic frustration, which opens up the possibility of a transformation to a noncollinear magnetic state. Thus, a possible answer to the puzzle is why Mn_2NiIn did not stabilize in a noncollinear state upon compression of the same magnitude as the three other systems could be traced to the exchange interactions of MnII sublattices.

5.3.4 The role of chemical composition and crystal structure

We now look into the effects of chemical compositions and crystal structures on the stabilizations of spin spiral ground states in the context of the Heusler and inverse Heusler structures. We perform systematic investigations in the following way:

(i) We compute the energies of spiral magnetic states as a function of **q** for Ni_2MnX materials at the compressed volumes used for Mn_2NiX materials as presented in T 5.1. Since Enkovaara *et al.* had already found that the collinear structures are the magnetic ground states for Ni_2MnAl and Ni_2MnGa at their respective equilibrium volumes, computations of the same at compressed volumes would provide us the effect of pressure on the stabilizations of noncollinear states.

(ii) We repeat the same calculations for Ni_2MnX materials, but by arranging the atoms in an inverse Heusler structure.

(iii) We do the same calculations for Mn_2NiX materials, but by arranging the atoms in a Heusler structure.

The results of these calculations would certainly whether reveal the chemical composition and/or the crystal structures have any role in the stabilizations of noncollinear spin spiral states in Ni-Mn-*X* systems.

F 5.6 show the energies of the spin spirals along [00**q**] direction for Ni_2MnX materials in the Heusler structure calculated at compressed lattice constants of T 5.1. Since

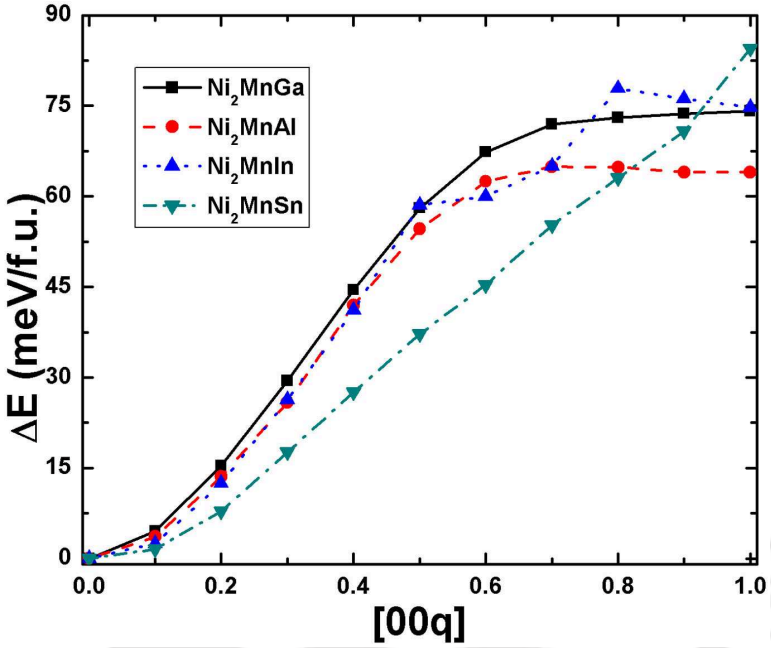

F 5.6: Total energies of Ni_2MnX systems as a function of spin spiral vectors **q** in the usual Heusler structure. All the calculations are done at compressed lattice constants of T - 5.1 [225].

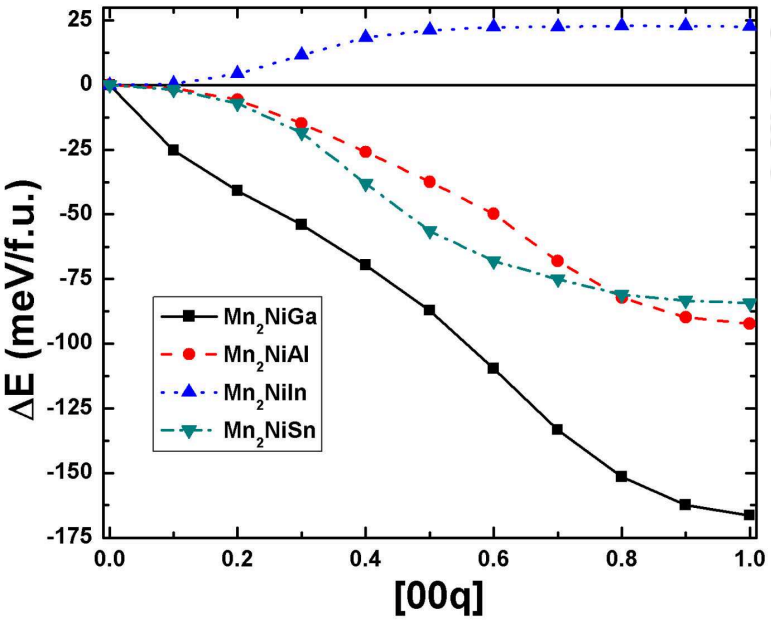

F 5.7: Total energies of Mn_2NiX systems as a function of spin spiral vectors **q** in the usual Heusler structure. All the calculations are done at compressed lattice constants of T - 5.1.

equilibrium lattice constants of Ni_2MnX and Mn_2NiX are close to each other, the use of compressed lattice constants of the later, generate same amount of compressions on those of Mn_2NiX counterparts. The results demonstrated that even at compressed volumes, possibilities of realizing a noncollinear spiral state in any of these Ni_2MnX materials are not observed. Thus, unlike Mn_2NiX systems, effect of pressure does not play any role in affecting the magnetic ground state of Ni_2MnX systems. These results compel us to suspect that the absence of a noncollinear ground state is an artifact of the crystal structure. To check whether this is indeed the case, we compute the energies of Mn_2NiX materials in the Heusler structure calculated at compressed volumes. The results are presented in F 5.7. We find that the ground states for all the materials except Mn_2NiIn, are at $\mathbf{q}= (\frac{\pi}{a})$, another collinear state. For Mn_2niIn, similar to F 5.1, we find that the magnetic ground state is collinear. The results, therefore, suggest that the noncollinear states cannot be realized even by changing the chemical compositions in Ni-Mn-*X* systems, and by applying pressure, as long as the crystal structure remains Heusler. For further confirmation of this inference, we explore the phase stabilities of spiral magnetic structures in Ni_2MnX by arranging the constituents in an inverse Heusler structure. The results are shown in F 5.8. Here too, we observe that collinear configuration is the magnetic ground state for all the Ni_2MnX materials. Analyzing all these

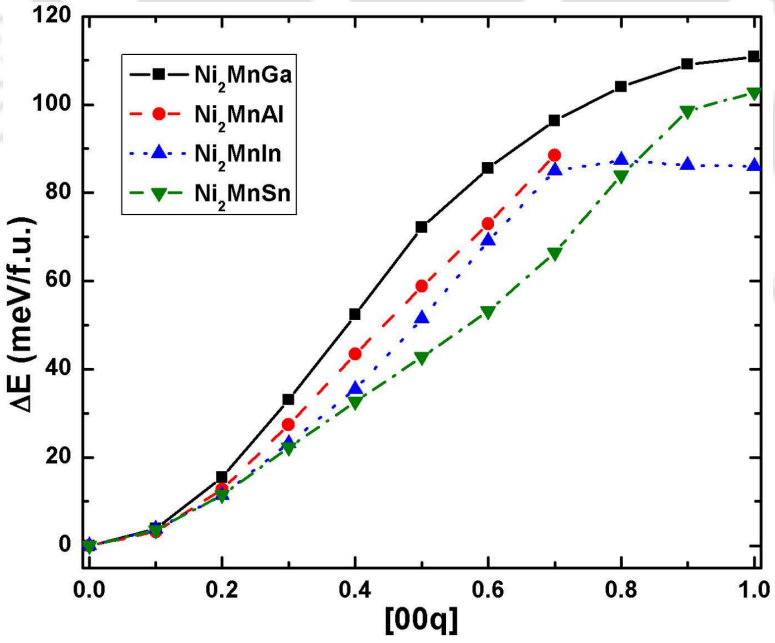

F 5.8: Total energies of Ni_2MnX systems as a function of spin spiral vectors **q** in the inverse Heusler structure. All the calculations are done at compressed lattice constants of T 5.1.

results, we, therefore, conclude that the both crystal structure and chemical constituent are important in stabilizing a noncollinear spin spiral state in Ni-Mn-*X* materials. The inverse Heusler structure and antiparallel coupling between the inequivalent Mn atoms in Mn_2NiX materials is crucial for stabilization of noncollinear state.

5.4 Summary

In this chapter, we investigated the actual ground state magnetic structure of Mn_2NiX materials with a focus on finding stable noncollinear spin spiral states. Our first-principles based calculations show that under pressure, which can be produced by compressing the lattice constant about 3.5%, the collinear phases of Mn_2NiX materials can phase transform into complex combinations of spiral magnetic phases. However, this amount of pressure does not affect the collinear state of Mn_2NiIn, where more compressions are necessary for this material to observe the same effect. This magnetic phase transformation can be correlated to magnetic barocaloric effect, an added functionality for these materials. Analysis of the electronic structures point out towards the following two mechanisms- (i) opening of a gap at the Fermi level as a consequence of the hybridization between spin-up and spin-down bands in the noncollinear phases; (ii) nesting between spin-up and spin-down Fermi sheets are possible for realizations of spiral magnetic structures as ground states. We also find that intra-atomic exchange interactions of Mn atom at octahedral sublattice stabilize the spin spirals by introducing frustrations into the materials. Comparisons between usual Heusler and inverse Heusler structures in stabilizing spin spiral revel that both the crystal structure and the chemical composition are important to obtain stable spin spirals in Ni-Mn-*X* materials.

Chapter 6

Anti-site disorder driven improvements in the functionalities of Mn_2NiX materials* †

6.1 Introduction

In the earlier chapters, we have stated that few experimental results on the total moments in the austenite phase are available for Mn_2NiGa [103–107] and Mn_2NiSn [102]. The only experimental result [102] available on the later material suggests that the magnetizations in this material can be quite large, as opposed to the conventional wisdom that the magnetizations in Mn_2NiX are significantly smaller than the Ni_2MnX materials due to antiparallel alignments of the two crystallographically inequivalent Mn atoms in the former. Helmholdt *et al.* [102] and later Luo *et al.* [108] found that the measured magnetizations in Mn_2NiSn are as large as 2.48 μ_B/f.u. and 2.95 μ_B/f.u. On the other hand, our calculated total moments (~0.6 μ_B/f.u.) for this material are an order of magnitude smaller. Helmholdt *et al.* [102] had proposed a model of sublattice occupancy to explain their large experimentally obtained moments. The model suggests that the tetrahedral sublattices (0,0,0) and (0.50,0.50,0.50) are occupied by both MnI and Ni atoms, whereas the other two octahedral sublattice (0.25,0.25,0.25) and (0.75,0.75,0.75) are fully occupied by single species, i.e., by MnII and Sn atoms, respectively. Considering site occupation of the tetrahedral sublattices as adjustable parameter, they computed the site occupancies and partial magnetic moments of Mn atoms. The results showed that the magnetic

*Contents of this chapter are mostly taken from Ref. [259, 260].
†Permission from the publishers have been obtained for reprints of Ref. [259, 260].

moments of Mn atom at octahedral position do not change much. On the contrary, the moments of Mn atom at two tetrahedral positions change significantly as compared to the ordered inverse Heusler structure. The partial moments of MnI atom at the tetrahedral position and MnII atom at the octahedral positions, as calculated with the model, were 2 μ_B and 4 μ_B, respectively, explaining the large moments observed experimentally. Later, detail investigations on the site occupation in the cubic phase of Mn_2NiGa from high resolution Neutron diffraction data [106] and first-principles based calculations [261] also showed the existence of Mn_xNi_{1-x} binary alloying in the two tetrahedral sublattices. It, thus, appears that the anti-site disorder at the tetrahedral sublattices of Mn_2NiX is inherent and can result in large magnetizations. Taking clues from this, our primary interest is to investigate whether the anti-site disorder is indeed inherent in all the four materials and whether the chemical disorder at selected sites can induce a large magnetizations differences ΔM between the austenite and the martensitic phases in these materials. The magnitude as well as sign of ΔM is important for the improvements in the functional properties for these materials. For example, Zeeman energy plays a crucial role in realizing the martensitic transformation in magnetic shape memory alloys. An externally applied magnetic field performs two different tasks inside MSMAs. Firstly, if the direction of the applied field is different from the easy magnetic axis of the material, the field tries to rotate the magnetization direction along it against the force associated with magnetic anisotropy. Secondly, the field generates driving force across the twin boundaries between martensitic variants and the associated energy is known as Zeeman energy. Since the energy required to move martensitic domains is lower than the magnetocrystalline anisotropy energy in MSMAs, the pressure created by Zeeman energy increases the volume fraction of favorably oriented martensitic variants and lowers the energy of the product phase. It has been found that a large ΔM between the two phases in the presence of moderate external magnetic field H, i.e., the Zeeman term ΔM.H, drives the motions of the martensitic domains facilitating the martensitic transformation [56]. On the other hand, the sign of ΔM is related to the conventional or inverse magnetocaloric effect [56]. In case of the former, a magnetic field will cause a decrease in entropy when applied isothermally and an increase in temperature when applied adiabatically. In case of the later, an increase in entropy will effect a decrease of temperature leading to magnetic cooling, a phenomenon which can be exploited for green technology in refrigeration. For the inverse magnetocaloric effect, the magnetization in the martensitic phase has to be lower than that in the austenite phase. Recently, using first-principles calculations, D'Souza *et al.* [261] proposed that Mn_2NiGa would exhibit inverse magnetocaloric effect.

Inspired by the above facts, in this chapter, we have investigated the properties of the four Mn_2NiX alloys which are potential MSMAs, in crystal structures relevant to the austenite and the martensite phases, with and without anti-site disorder. We specifically looked at the trends in ΔM across the series and commented on the implications on functional properties. We have computed the electronic densities of states and inter-atomic exchange interactions of the magnetic atoms to explain the results on magnetizations as one goes from one configuration to other in both the austenite and the martensitic phases of these materials.

6.2 Computational Details

The electronic structures of the materials concerned have been calculated using Full-potential based Spin-Polarized Relativistic Korringa-Kohn-Rostoker (SPR-KKR) Green's function method [194, 195]. The Local Spin Density Approximation (LSDA) as parameterized by Vosko-Wilk-Nusair (VWN) was used as the exchange-correlation part of the potential to solve the Kohn-Sham equation [262]. The angular momentum cut-off to the plane wave was taken to be ℓ_{max}= 3. The Brillouin zone integrations have been carried out on a uniform 24×24×24 **k**-mesh. The Green's function was calculated for 30 complex energy points distributed exponentially on a semicircular contour. The energy convergence criterion was set to 10^{-6} Ry for the self-consistent cycles. The Coherent Potential Approximation (CPA) was used to incorporate the effects of disorder [165].

T 6.1: Sublattice occupancies corresponding to the configurations used. The details are described in the text [260].

Configuration	Sublattice			
	(000)	$(\frac{1}{2}\frac{1}{2}\frac{1}{2})$	$(\frac{1}{4}\frac{1}{4}\frac{1}{4})$	$(\frac{3}{4}\frac{3}{4}\frac{3}{4})$
OC	MnI	Ni	MnII	Sn
50-50 (**DC**)	$(MnI_{0.5})Ni_{0.5}$	$(MnI_{0.5})Ni_{0.5}$	MnII	Sn
60-40 (**DC**)	$(MnI_{0.6})Ni_{0.4}$	$(MnI_{0.4})Ni_{0.6}$	MnII	Sn
70-30 (**DC**)	$(MnI_{0.7})Ni_{0.3}$	$(MnI_{0.3})Ni_{0.7}$	MnII	Sn
DT	$(MnI_{0.5})Ni_{0.5}$	$(MnI_{0.5})Ni_{0.5}$	MnII	Sn

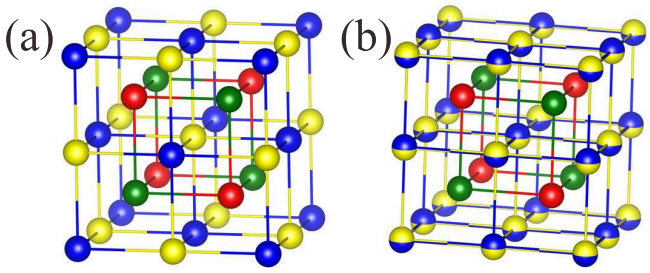

F 6.1: The crystal structure of Mn_2NiX in (a) **OC** and in (b) **DC** configurations. The blue, green, yellow and red spheres represent MnI, MnII, Ni and *X* atoms, respectively. The two-toned spheres (blue and yellow) represent sublattices with Ni-MnI alloys [260].

T 6.1 shows different configurations used in this work. Space group $Fm\bar{3}m$ has been used for the cubic austenite phase and *Fmmm* for the tetragonal martensitic phase. The configurations without anti-site disorder, i.e., ones corresponding to the perfect inverse Heusler arrangement have been referred to as **OC** (Ordered Cubic) and **OT** (Ordered Tetragonal), while the ones with anti-site disorder have been referred to as **DC** (Disordered Cubic) and **DT** (Disordered Tetragonal). In cases of **OC** and **OT**, the sublattices with octahedral symmetries are occupied by the *X* element and one of the Mn atoms (referred to as MnII), while the sublattices with tetrahedral symmetries are occupied by Ni and the other Mn atom (referred to as MnI). In cases of **DC** and **DT**, the tetrahedral sublattices have anti-site disorder and hence they consist of binary alloys of MnI and Ni, MnI_xNi_{1-x}. The three partially disordered (50-05, 60-40 and 70-30) configurations have been named according to the Mn compositions in (0,0,0) and (0.50,0.50,0.50) sublattices. The reason for choosing only 50-50 configuration to study the tetragonal phase is described later.

In materials with chemical disorder, particularly in systems where constituents have large size differences such as Mn_2NiIn and Mn_2NiSn, there can be substantial relaxations of the local bonds. Since incorporation of the relaxations is not possible within the framework of the KKR-CPA method, we relaxed all the systems by VASP, a plane wave code employing the Projector Augmented Wave approach [188–190], keeping the volume fixed. In order to mimic the chemical disorder for "anti-site disordered" configurations, we consider supercells of 64 atoms with MnI and Ni atoms occupying the sites with tetrahedral symmetry randomly. We also construct a 64 atom "Special Quasi-random Structure" (SQS) [167] which simulates the environments around an atom in a chemically disordered alloy better as the SQS is generated by matching the maximum number of correlation functions to their exact values in the real disordered alloy. The SQS structures used in this work are generated with the 'Alloy

Theory Automated Toolkit' (ATAT) package [263]. 50 pairs and 30 triplets having correlation functions exactly equal to those for a real disordered alloy with the same composition were chosen to construct the SQS. The total energies were calculated with both the supercell and the SQS structure. A large basis was used with a plane wave cut-off of 450 eV. The exchange-correlation functional used was the same as that used in SPR-KKR calculations. Convergences of the electronic structures were assumed when changes between two consecutive steps were less than 10^{-5} eV. Atomic relaxations were carried out until all the forces were less than 10^{-3} eV/Å. A **k**-point mesh consisting of at least 9 **k** points in the irreducible part of the Brillouin Zone was considered and was sufficient for convergences of total energies and forces.

6.3 Results and Discussions

6.3.1 Understanding the origin of discrepancy between theory and experiment for Mn_2NiSn

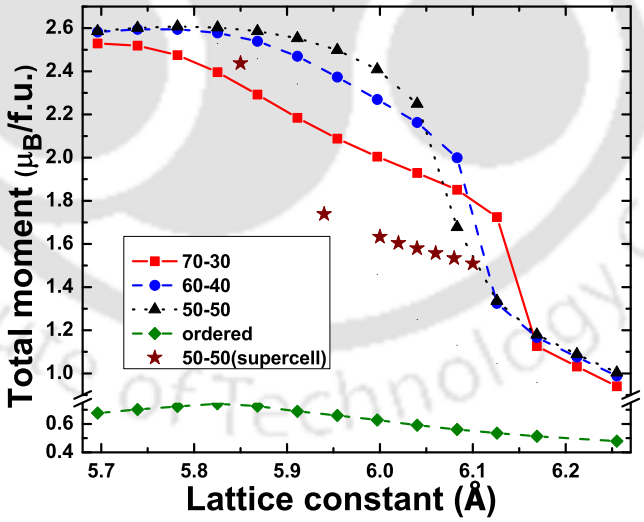

F 6.2: Total magnetic moments as a function of lattice constants for various **DC** configurations computed with KKR-CPA method. The results of ordered structure (**OC**) and supercell calculations for the 50-50 **DC** configuration are also presented for comparison [259].

To understand the origin of the discrepancy between theoretical and experimental results, as mentioned in the introduction and to validate the anti-site disorder model proposed by

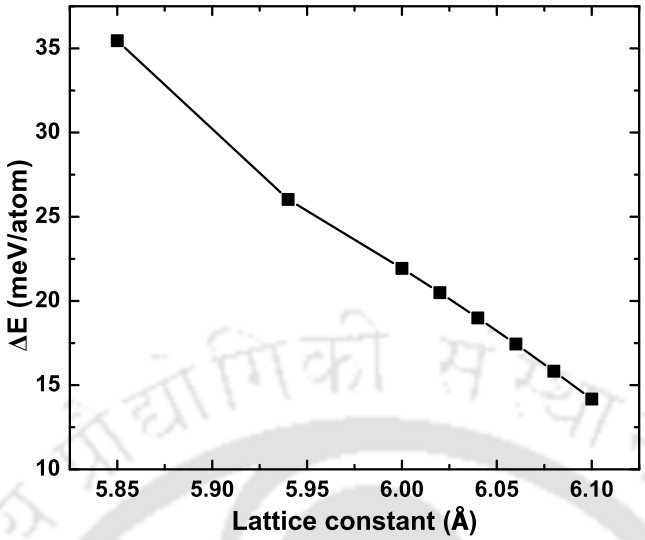

F 6.3: Total energy difference between the ordered and the 50-50 partially **DC** configuration as a function of volume obtained from PAW-PP supercell calculations. A positive value of ΔE implies that the total energy of the 50-50 **DC** configuration is lower than **OC** configuration [259].

Helmholdt *et al.* [102], we calculate the variations of the total magnetic moments as a function of volume for Mn_2NiSn in the cubic phase (F 6.2). The moments are calculated for **OC** and 50-50, 60-40 and 70-30 **DC** configurations. The results from the supercell calculations for the 50-50 **DC** configuration are also provided to estimate the effects of relaxation. The results of the SPR-KKR-CPA calculations reveal that a high magnetic moment as observed in the experiments can be obtained only if the sites with tetrahedral symmetry are occupied with a binary NiMn alloy. These results also suggest that the reason behind low magnetic moments when calculations are performed with larger lattice constants. The total moments of the **OC** phase are very low compared to the **DC** phases throughout the range of lattice constants. In order to make sure that a **DC** phase is the stable state, we computed ΔE, the energy difference between the **OC** and the 50-50 **DC** configurations, as a function of volume by the PAW-supercell method as implemented in VASP code. The results are shown in F 6.3 . A positive value of ΔE implies the stability of the **DC** configuration over the **OC** configuration. The results suggest that the 50-50 **DC** configuration is energetically lower than the **OC** configuration at all the volumes considered. Thus the stability of a partially ordered configuration is validated. In the course of the calculations, we found that unless one relaxes the atomic positions, the 50-50 **DC** configuration would not be the lower energy state at all volumes. Thus, the presence of Sn, a much bigger atom than the Ni and the Mn, introduces

local relaxations and the **DC** configuration is stabilized by such relaxations. It is expected that the same qualitative features will be observed for other **DC** configurations. We have repeated the calculations with a GGA exchange-correlation functional as well. The results are qualitatively same as the LDA ones.

6.3.2 Energetics of different configurations in Mn_2NiX materials

Among the three partially **DC** configurations, we tend to choose the 50-50 configuration for the calculations of magnetic moments, density of states and inter-atomic exchange interactions between the magnetic atoms in all the four materials. The reasons are as follows: (i) in F 6.2, the qualitative behavior of the magnetic moments for the three **DC** configurations are identical. (ii) the Neutron diffraction results in Mn_2NiGa suggested that the occupancies of sublattices in the inverse Heusler structure would be like the 50-50 **DC** configuration [106]. Although for Mn_2NiSn, the concentration suggested by the experiment is slightly different [102], our first-principles based calculations (F 6.1) showed that with this configuration, we can produce the experimental results. This also justifies the choice of that particular concentration for the calculation of magnetic moments for this and other materials. (iii) the choice of 50-50 concentration maximizes the anti-site disorder on the tetrahedral sites. For example, $(MnI_{0.40}Ni_{0.60})$ configuration at (0,0,0) sublattice would produce the same configuration at (0.50,0.50,0.50) sublattice, since MnI and Ni atoms occupy the crystallographically equivalent sites. Moreover, 50% MnI concentration at any of the two sites produces a configuration closer to the ordered (**OC** or **OT**) one. Therefore, for the above reasons we have chosen the 50-50 **DC** configuration for rest of the study and for the sake of consistency in investigations, tetragonal phase with 50-50 configuration for all the materials in Mn_2NiX series are considered, which is denoted as **DT** in T . 6.1.

In T 6.2, we tabulate the structural parameters used in this work. We have used the experimental lattice parameters of Mn_2NiGa in both phases and of Mn_2NiSn in the cubic phase. The lattice parameters for the other two alloys in both phases (cubic and tetragonal) and for Mn_2NiSn in tetragonal phase were calculated by KKR method. The results obtained for **OC** and **OT** configurations using SPR-KKR and VASP codes were nearly identical, with a maximum difference less than 1%. The same set of lattice parameters have been used for

T 6.2: The lattice parameters for Mn_2NiX systems used for rest of the work. a_{cubic} and a_{tet} are the lattice constants in the cubic and tetragonal phases respectively, $(c/a)_{tet}$ is the global minima in the tetragonal phase [260].

Systems	lattice constant a_{cubic}(Å)	lattice constant a_{tet}(Å)	$(c/a)_{tet}$
Mn_2NiAl	5.57	3.71	1.20
Mn_2NiGa	5.90	3.92	1.21
Mn_2NiIn	5.96	3.91	1.26
Mn_2NiSn	6.10	4.06	1.20

"ordered" and "disordered" configurations since it was found out that they hardly change from one configuration to another.

Before proceeding to calculate the total moments and electronic structures in cubic and tetragonal phases with the 50-50 configuration, one must make sure that

$$F_{DC} < F_{OC} \qquad F_{DT} < F_{OT} \tag{6.1}$$

Here F_{DC}, F_{OC}, F_{DT} and F_{OT} refer to the free energies in the four configurations respectively. These inequalities make sure that the "anti-site disordered" configurations are the thermodynamically favorable ones over the "ordered" ones, thus, making the justifications for analyzing results obtained with the "anti-site disordered" configurations any further. On top of this, one also has to make sure that the energy of the tetragonal phase in the "anti-site disordered" configuration is lower than that of the cubic phase in the same configuration, for each of these systems. Unless this occurs, further investigations into the systems exploring improved functionalities, based upon magnetizations in the austenite and in the martensite phases, would be useless.

Therefore, we compute the following quantities

$$\Delta E_{str}^{O/D} = E_{tet}^{O/D} - E_{cub}^{O/D} \tag{6.2}$$

$$\Delta F_{ord}^{C} = F_{OC} - F_{DC} \tag{6.3}$$

$$\Delta F_{ord}^{T} = F_{OT} - F_{DT} \tag{6.4}$$

ΔE_{str}^{O} and ΔE_{str}^{D} refer to the energies required for structural transition from the cubic to the tetragonal phase when the system is in "ordered" configuration **O** and in "anti-site disordered"

configuration **D**, respectively. A negative value of $E_{str}^{O/D}$ means that the tetragonal phase is energetically lower than the cubic phase in the **O/D** configuration and that the martensitic transformation is possible. ΔF_{ord}^{C} and ΔF_{ord}^{T} are the free energies of the configuration **O** with reference to those of the configuration **D** in the cubic (C) and in the tetragonal (T) phases, respectively. The free energy expression considered here is,

$$F = E + \frac{k_B T}{N} \sum_i x_i ln x_i + (1 - x_i)\, ln\,(1 - x_i) \tag{6.5}$$

E is the electronic energy per atom, k_B is the Boltzmann constant, T is the temperature, N is the number of atoms, i is the sublattice index and x_i is the concentration of sublattice i. Here we have considered only the contribution of the configurational part to the entropy and neglected the effects of the lattice vibrations and electronic temperatures. At ambient conditions, the effect of the electronic temperature is negligible. The contribution from lattice vibration to the free-energy difference for alloys with different site-occupation configurations can be estimated approximately from the high temperature expansion of the phonon free energy ΔF_{ph}~3 kT ($\Delta\Theta/\Theta$) [264]. In the simplest approximation, the Debye temperatures Θ are proportional to $\sqrt{r}B$ [265], where r is the Wigner-Seitz radius and B is the bulk modulus. For the systems considered here, the lattice constants and hence the Wigner-Seitz radii differ only slightly between the **O** and the **D** configurations; same happens for Bulk moduli. Consequently, the contributions from vibrational part to the entropy are orders of magnitude smaller than the electronic contributions. In this chapter, we have calculated the contributions from configurational entropy to the free energies only at T= 300 K.

T 6.3: $\Delta E_{str}^{O/D}$, ΔF_{ord}^{C}, ΔF_{ord}^{D} in Mn_2NiX materials calculated for 64 atom supercell and 64 atom SQS. Calculations are done with PAW-PP method [260].

	64 atom supercell				64 atom SQS			
Systems	ΔF_{ord}^{C} (meV/ atom)	ΔF_{ord}^{T} (meV/ atom)	ΔE_{str}^{O} (meV/ atom)	ΔE_{str}^{D} (meV/ atom)	ΔF_{ord}^{C} (meV/ atom)	ΔF_{ord}^{T} (meV/ atom)	ΔE_{str}^{O} (meV/ atom)	ΔE_{str}^{D} (meV/ atom)
Mn_2NiAl	32	9.7	-8.11	14.6	37	8.9	-8.2	19.9
Mn_2NiGa	10.0	3.5	-22.4	-15.8	9	3.6	-21.6	-16.8
Mn_2NiIn	31	11.4	-20.6	-1.5	28.6	12.1	-19.9	-3.4
Mn_2NiSn	30	27.7	-5.83	-3.2	32.4	37.4	-4.2	-2.2

Our calculated results on $\Delta E_{str}^{O/D}$, ΔF_{ord}^{C} and ΔF_{ord}^{T}, obtained after relaxations of atomic positions in the supercell and in the SQS structure calculated with the VASP code are shown in T 6.3. We note that apart from qualitative agreement on the trends, the quantitative agreement is also close between the two different supercells simulating the "anti-site disordered" configurations. We find that $\Delta E_{str}^{D} > 0$ for Mn_2NiAl implying that in the "anti-site disordered " configuration, the martensitic transformation does not take place. Therefore, this system in the disordered configuration would not be suitable for the functionalities related to martensitic phase transformations and thus, we exclude this system from the rest of our discussions. For the other three systems, $\Delta E_{str}^{D} < 0$ along with $\Delta F_{ord}^{C/T} < 0$ implying that the "anti-site disordered" configuration (**D**) is thermodynamically favorable over the ordered configuration (**C**) for each of these systems irrespective of the crystal structure, and that the martensitic transformation takes place in all of them with the configuration **D**.

6.3.3 Dependence of the magnetic moments of Mn_2NiX on configurations

After validating that the 50-50 **D** configurations are energetically lower than the **O** configurations, we compute the magnetic moments, the electronic structures, the exchange interactions and the Curie temperatures for Mn_2NiGa, Mn_2NiIn and Mn_2NiSn in **OC**, **OT**, **DC** and **DT** configurations using the KKR-CPA method. The starting spin configurations between two nearest neighbor Mn atoms in all three configurations considered are kept antiparallel. In the **DC** and **DT** configurations, the MnI atoms occupying the sublattices with tetrahedral symmetry are considered to be parallel in the beginning as they are not the nearest neighbors. These starting configurations lead to the lowest energy states. The calculated total and partial magnetic moments of Mn_2NiX materials, excluding Mn_2NiAl, in all three configurations are summarized in T 6.4.

The central quantity related to multi-functionalities in the present context, ΔM is defined as $\Delta M = M_{tot}^{martensite} - M_{tot}^{austenite}$, the total moment in the martensite phase with respect to that in the austenite phase for a given occupancy of the sublattices. Calculated values of ΔM are also presented in T 6.4. The results show the following trends:

T 6.4: Total (M_{tot}) and partial (M_i) moments of the constituent atoms for Mn_2NiX materials in four different configurations. ΔM represents the total moment in martensite phase with respect to that in the austenite phase for a given sublattice occupancy (either **O** or **D**) [260].

Systems	Conf.	M_{tot} (μ_B)	M_{MnI} (μ_B)	M_{MnII} (μ_B)	M_{Ni} (μ_B)	M_X (μ_B)	Conf.	M_{tot} (μ_B)	M_{MnI} (μ_B)	M_{MnII} (μ_B)	M_{Ni} (μ_B)	M_X (μ_B)	ΔM (μ_B)
Mn_2NiGa	**OC**	1.26	-2.27	3.17	0.35	0.01	**OT**	1.12	-2.27	3.05	0.33	0.01	-0.01
	DC	2.13	-1.42	3.15	0.40	0.00	**DT**	1.42	-2.02	3.07	0.36	0.01	-0.71
Mn_2NiIn	**OC**	1.02	-2.42	3.17	0.27	-0.00	**OT**	1.00	-2.30	3.02	0.28	0.00	-0.02
	DC	2.09	-1.40	3.15	0.35	-0.01	**DT**	1.22	-2.10	3.01	0.31	0.00	-0.86
Mn_2NiSn	**OC**	0.71	-2.74	3.33	0.11	0.01	**OT**	0.38	-2.84	3.19	0.04	-0.01	-0.33
	DC	2.38	-1.26	3.40	0.23	0.01	**DT**	1.68	-1.96	3.34	0.29	0.02	-0.70

T 6.5: The inter-atomic distances (in Å) between the magnetic atoms for Mn_2NiX systems in cubic and tetragonal phases [260].

Systems	Cubic			Tetragonal		
Mn_2NiX	MnI-MnII	Ni-MnI	MnII-Ni	MnI-MnII	Ni-MnI	MnII-Ni
Mn_2NiGa	2.56	2.95	2.56	2.58	2.77	2.58
Mn_2NiIn	2.58	2.98	2.58	2.61	2.76	2.61
Mn_2NiSn	2.64	3.05	2.64	2.66	2.87	2.66

(i) The magnetic moments in the martensitic phase is lower than that in the austenite phase for both "ordered" and "disordered" configurations and for all three alloys under consideration, making $\Delta M < 0$.

(ii) For the "disordered" configurations, i.e., both **DC** and **DT**, the magnetic moments are substantially higher than their "ordered" counterparts, i.e., **OC** and **OT** respectively. The increment is significantly greater in austenite phases than that in the martensitic phases. The total moment increases by 69%, 104% and 235% for Mn_2NiGa, Mn_2NiIn and Mn_2NiSn respectively as configuration changes from **OC** to **DC**. In the martensitic phases, the increase in moments as configuration changes from **OT** to **DT** are 27%, 22% and 342% for Mn_2NiGa, Mn_2NiIn and Mn_2NiSn respectively. These results show huge gain in ΔM in the "anti-site disordered" configurations over that in the "ordered" configurations.

The behavior of the magnetic moments across crystal structures, configurations and materials, are driven by the crystallographically inequivalent Mn atoms. The results suggest that the ferrimagnetic ground states are achieved due to the anti-parallel alignments of the MnI

and MnII atoms. In the "ordered" configurations, the magnitude of the moments compensates each other substantially resulting in relatively low moments. Drastic changes are observed in cases of anti-site disorder. The substantially high moments in **DC** and **DT** configurations are driven by considerable quenching of Mn moments at the sites where they form alloys with Ni. The moments of the other Mn atom remain nearly unaltered. The Ni moments, on the other hand, increases significantly, bringing in an increase in the net moments. The changes are more dramatic in the austenites where the MnI moment changes between 37-54% as compared to changes between 8-30% in the martensites.

The significant changes in the MnI moments driven by the anti-site disorder coupled with a substantially larger change in the total moments in the austenites lead to larger ΔM when anti-site disorder affects the sublattices with tetrahedral symmetry in the inverse Heusler structure. This is a significant result as it shows that all three Mn_2NiX alloys may exhibit inverse magneto-caloric effects and a large Zeeman energy can be achieved with relatively small magnetic field making them attractive from the point of view of shape memory applications. It may be noted that the prototype MSMA Ni_2MnGa has $\Delta M > 0$ and the magnitude of ΔM is only ~0.2 μ_B [99]. Thus, Mn_2NiX alloys turn out to be MSMAs with better functional parameters even with the stoichiometric composition of 2:1:1. In the next two subsections, we explore the origin of these magnetic properties by discussing results on electronic structures and magnetic exchange interactions.

6.3.4 Electronic structure of Mn_2NiX and dependencies on configurations

A comprehensive comparative presentation of the densities of states in various configurations for the three systems considered are shown in F 6.4- 6.6. In each figures, panels (a)-(d) show comparisons of total and partial densities of states (of magnetic components) for **OC** and **DC** configurations. Panels (e)-(h) of each figure show comparisons of same quantities for **DC** and **DT** configurations. The comparisons between **OC** and **OT** configurations for these systems had already been done in chapter 3.

The densities of states of all three alloys in the **OC** configuration show certain common features: the MnI densities of states have characteristic unfilled majority bands as can be inferred by the presence of substantial states in the unoccupied part, while MnII have same

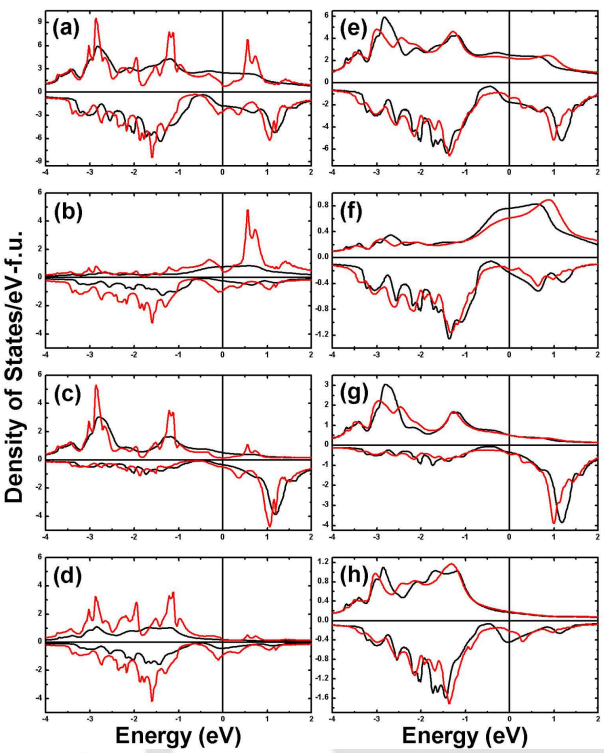

F 6.4: Total and partial densities of states for Mn_2NiGa. In panels (a)-(d) black curves stand for **DC** configuration and red curves stand for **OC** configuration. In panels (e)-(h), black curves denote the **DC** configuration and red curves denote the **DT** configuration. (a)-(d) and (e)-(h) panels display total, MnI, MnII and Ni densities of states, respectively [260].

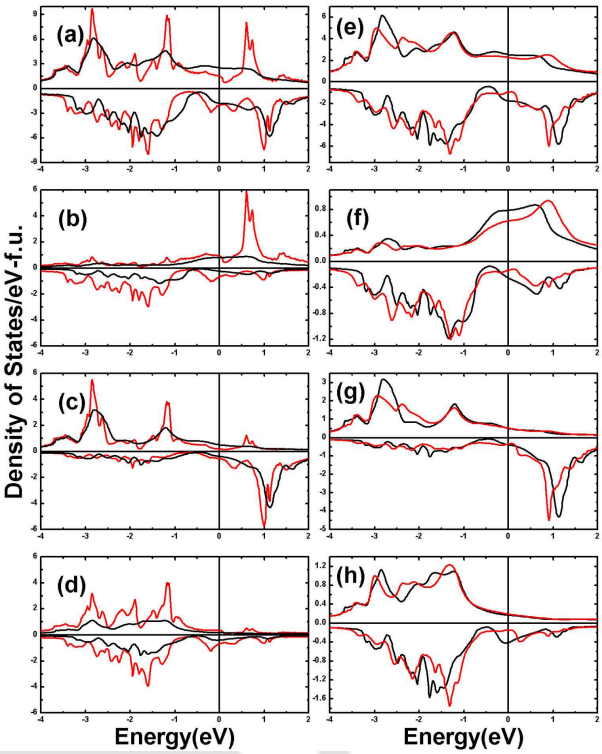

F 6.5: Total and partial densities of states for Mn_2NiIn. In panels (a)-(d) black curves stand for **DC** configuration and red curves stand for **OC** configuration. In panels (e)-(h), black curves denote the **DC** configuration and red curves denote the **DT** configuration. (a)-(d) and (e)-(h) panels display total, MnI, MnII and Ni densities of states, respectively [260].

characteristics associated with their minority bands. This explains the reasons for getting substantial compensation of Mn moments leading to rather small total moments. The features in the minority bands near the Fermi level emerge due to hybridizations between MnI and Ni 3*d* states. For Mn_2NiGa and Mn_2NiIn, such hybridizations give rise to a small peak around -0.25 eV in the minority bands, while for Mn_2NiSn, a prominent peak around -0.5 eV emerges. The prominent peaks in the occupied part of the minority bands such as the ones between -1 eV and -2 eV also arise from the hybridizations of same states. The majority bands for all three systems too have common characteristics; the features in the occupied parts arise due to hybridizations between Ni and MnII states.

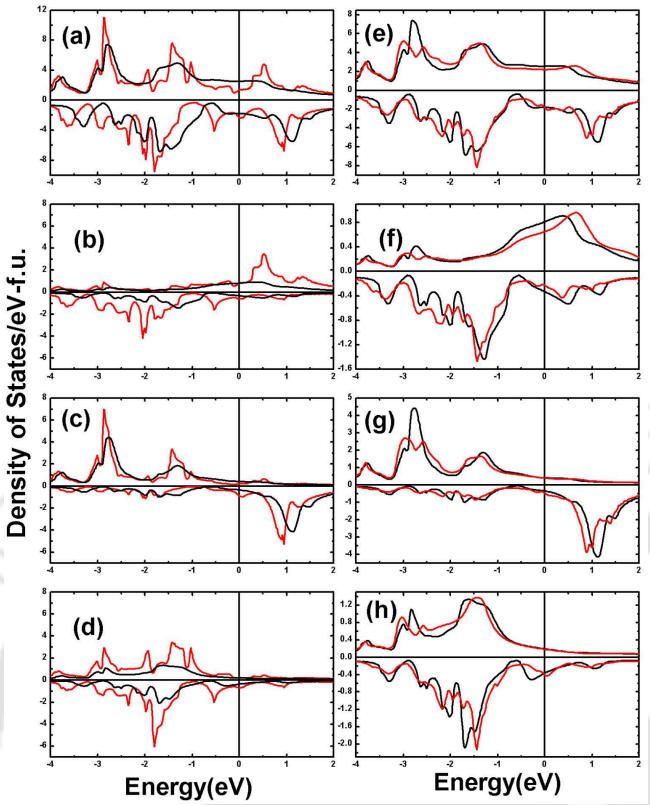

F 6.6: Total and partial densities of states for Mn_2NiSn. IIn panels (a)-(d) black curves stand for **DC** configuration and red curves stand for **OC** configuration. In panels (e)-(h), black curves stand for **DC** configuration and red curves stand for **DT** configuration. (a)-(d) and (e)-(h) panels display total, MnI, MnII and Ni densities of states, respectively [260].

Significant modifications to the densities of states in the **DC** configurations occur due to anti-site disorder between MnI and Ni sites. Expectedly, major changes in the electronic structure come from the MnI and the Ni densities of states. The total densities of states in the majority spin channel become rather featureless and flat in the **DC** configurations. The densities of states in the minority bands, although still retain some of the structures, but become smooth in general. For example, the peaks near the Fermi level in the minority bands of Mn_2NiGa and Mn_2NiIn and the peaks at the Fermi level in the minority bands of Mn_2NiSn are all broadened in the **DC** configuration. MnI densities of states are affected most followed by the Ni ones. The minority spin MnI peaks (around -1.5 eV for Mn_2NiGa and Mn_2NiIn, and around -2 eV for Mn_2NiSn) broaden considerably and move closer to Fermi level (around -1.4 eV for Mn_2NiGa and Mn_2NiIn, and around -1.3 eV for Mn_2NiSn). The peaks near or at the Fermi level in the minority channels are now destroyed producing continuously increasing densities of states near the Fermi levels. The peaks in the unoccupied parts of the majority

bands of MnI atoms are severely modified: their intensities decrease considerably and they flatten out into broad plateaus extending into the occupied parts. Thus, the occupied parts in the majority bands start to get filled with states. Consequently, the magnetic moments of MnI atoms decrease in magnitudes as compared to the ones in the **OC** configurations. Densities of states in both spin channels associated with Ni too get modified with sharp peaks in **OC** configurations getting broadened in general. The states in the minority channels start to shift towards the Fermi level, while there is hardly any shift in the states in the majority channels (comparison of panels (d) and (h) illustrate these clearly). These features explain the slight increases in the Ni moment in the **DC** configurations in comparison to the **OC** configurations of all three alloys. The anti-site disorder between MnI and Ni sites do not affect MnII densities of states substantially. The major features of the MnII densities of states in **OC** configuration do not change in **DC** configurations; the peaks only broaden explaining why the MnII moments remain almost intact in spite of anti-site disorder. To summarize, the drastic re-distribution of electronic states in both spin channels of primarily MnI atoms, brought about by the anti-site disorder between the sites of same point group symmetry, quenches the MnI moments substantially reducing the exchange splitting and thereby increasing the total magnetic moment significantly as compared to the **OC** configurations. The degree of this increment depends on the degree of changes in the MnI densities of states. The maximum changes occur in Mn_2NiSn, where, the peak at -2 eV in the MnI minority band moves substantially towards the Fermi level, relocating itself at -1.25 eV as one goes from **OC** to **DC**, the other peaks too make such a move, affecting the electron distribution considerably, explaining why the changes in the moments are the largest in the series.

The reason behind obtaining a large ΔM when anti-site disorder is present, as compared to the "ordered" configurations is that the magnetic moments do not change as substantially as the systems undergo martensitic transformations. The percentage changes quoted in Section 6.3.3 exemplify this. In order to understand the reasons behind this, one needs to inspect the panels (e)-(h) in F 6.4- 6.6 where comparisons between densities of states in the **DC** and **DT** configurations are done. The results suggest that for all three materials, the total densities of states at the Fermi level in the **DT** configurations are less than that in the **DC** configurations. This provides a clue to the stability of the martensitic phases. In fact, the densities of states are suppressed prominently in the minority bands of between -0.3 eV and the Fermi level in the **DT** configurations. In contrast, the minority densities of states in **DT** configurations for all three materials get elevated as compared to the **DC** configurations

between -0.3 eV and -1 eV. These undoubtedly point to the fact that electron states are transferred to the lower energies as the systems undergo martensitic transformations, explaining the stabilizations of the martensitic phases.

From the atom projected densities of states, it is clear that the hybridizations of Ni-MnI 3*d* minority electrons are responsible for such re-distributions of electronic states when the system undergoes a tetragonal deformation. Due to the tetragonal distortion, the Ni-MnI hybridizations strengthen due to the significant reductions of the Ni-MnI bond distances. Table V shows the bond distances between various Mn atoms in the austenite and in the martensitic phases. The results clearly demonstrate that only the Ni-MnI inter-atomic distances reduce by almost 6% in all the cases. On the other hand, the changes in the majority band electronic structures due to tetragonal distortions are overwhelmingly due to the MnI states. A comparison between **DC** and **DT** configurations show that states in the MnI majority bands are pushed into the unoccupied part as the systems undergo martensitic transformations. This coupled with the shifting of minority states towards lower energies produce a larger exchange splitting of MnI resulting in an increase of the net MnI moment as compared to the austenitic phases. Thus the total moment in the martensitic phases do not change as much as they do in the austenite phases upon changes in the sublattice occupancies due to anti-site disorder in the sites with tetrahedral symmetries, resulting in a larger ΔM in the "disordered" configurations. In the next section, we show comparative results on inter-atomic exchange interactions across the structures, configurations and the materials in order to understand the trends in the magnetic properties of Mn_2NiX series.

6.3.5 Effects of configurations on exchange interactions and the Curie temperatures of Mn_2NiX

Our calculated results on inter-sublattice and intra-sublattice exchange interactions are presented in F 6.7- 6.9. The results suggest that in all three materials, the magnetic properties are governed by competitions between two interactions: Ni-MnII and MnI-MnII. The MnI-MnII interactions are anti-ferromagnetic while the Ni-MnII interactions are ferromagnetic. Comparisons of **OC** and **OT** configurations show that upon tetragonal distortions, the anti-ferromagnetic MnI-MnII interactions strengthen while the ferromagnetic Ni-MnII interactions weaken, resulting in a net loss of MnII moments and subsequent low moments in

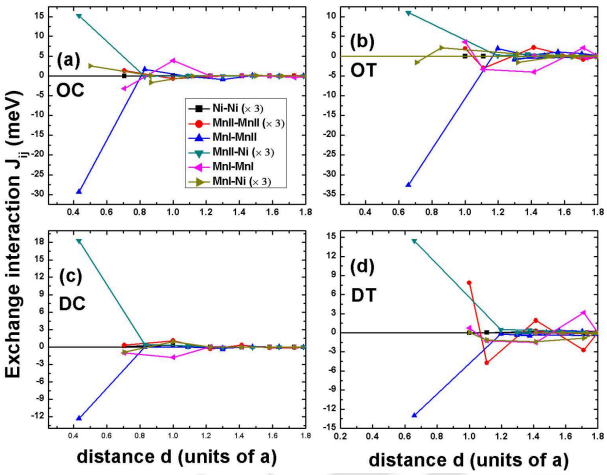

F 6.7: Magnetic exchange interactions (J_{ij}) as a function of inter-atomic distance d for Mn_2NiGa. Panels (a), (b), (c) and (d) represent ordered cubic (**OC**), ordered tetragonal (**OT**), disordered cubic (**DC**) and disordered tetragonal (**DT**) configurations, respectively [260].

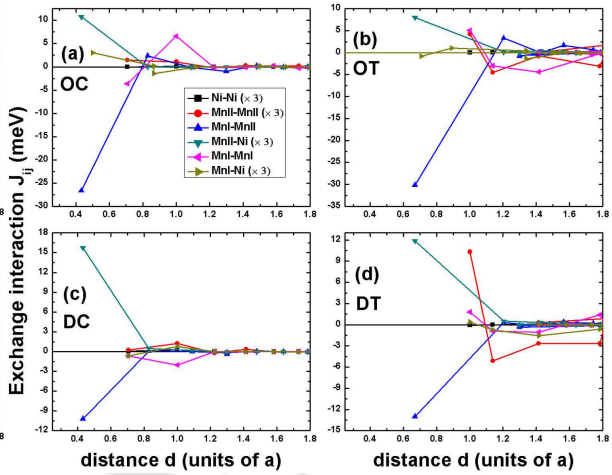

F 6.8: Magnetic exchange interactions (J_{ij}) as a function of inter-atomic distance d for Mn_2NiIn. Panels (a), (b), (c) and (d) represent ordered cubic (**OC**), ordered tetragonal (**OT**), disordered cubic (**DC**) and disordered tetragonal (**DT**) configurations, respectively [260].

the **OT** configurations. Drastic modifications in the exchange interactions are observed due to anti-site disorder. A comparison between **OC** and **DC** configurations show that for all three alloys, the Ni-MnII interactions strengthen that is become more ferromagnetic while the MnI-MnII interactions weaken substantially. The weakening of the most prominent antiferromagnetic interaction and strengthening of the most prominent ferromagnetic interaction in presence of anti-site disorder strengthen the ferromagnetic interactions in the systems resulting in the enhancement of the overall magnetic moments when anti-site disorder is present. However, comparative assessments of **DC** and **DT** configurations show that upon tetragonal distortions, the ferromagnetic Ni-MnII interactions weaken and the antiferromagnetic MnI-MnII interactions strengthen. The weakening of the former being substantial, the antiferromagnetic interactions in the **DT** configurations are more significant than those in the **DC** configurations, resulting in a lower total moment in the former configurations in comparison to the later ones.

The intra-sublattice exchange interactions are much weaker than the inter-sublattice ones and thus do not contribute enough to understand the trends in the magnetic properties. However, unlike the inter-sublattice ones, no common trend across the materials is observed in

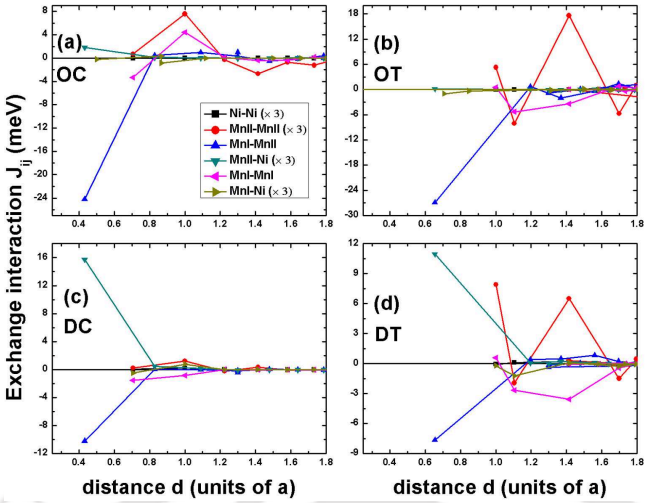

F 6.9: Magnetic exchange interactions (J_{ij}) as a function of inter-atomic distance d for Mn_2NiSn. Panels (a), (b), (c) and (d) represent ordered cubic (**OC**), ordered tetragonal (**OT**), disordered cubic (**DC**) and disordered tetragonal (**DT**) configurations, respectively [260].

some of these interactions. The Ni-Ni interactions are the weakest and are weakly ferromagnetic for all materials and for all configurations. The MnI-MnI interactions are oscillatory in the **OC** configurations and become slightly anti-ferromagnetic in the **DC** configurations. In the **DT** configurations, they again become oscillatory with first neighbor being strongly ferromagnetic and second and third neighbors being slightly anti-ferromagnetic; the only exception being Mn_2NiSn where the second and third neighbor anti-ferromagnetic interactions are stronger than the first neighbor ferromagnetic one. The Ni-MnI interactions become weak and predominantly anti-ferromagnetic as one goes from **OC** to **DC** configurations where they are predominantly ferromagnetic. Under tetragonal distortions in the **DC** configurations, the first neighbor interactions change to become slightly ferromagnetic offering no other significant changes. The MnII-MnII interactions vary qualitatively quite a bit across materials. In the **OC** configurations, they are oscillatory in case of Mn_2NiSn with dominant interactions being ferromagnetic. For the other two materials, the interactions are primarily ferromagnetic and weaker in comparison to Mn_2NiSn. The anti-site disorder keeps the interactions largely intact except that they are weaker in Mn_2NiSn. The tetragonal distortions modify these interactions significantly by making them more oscillatory. However, the strengths of the ferromagnetic and anti-ferromagnetic components in the oscillatory exchange interactions are nearly equal and thus compensate. To summarize, the magnetic exchange interactions in these materials are thus influenced by the inter-sublattice interactions and changes in their relative strengths upon changes in structures and configurations help make connections to the

trends in the magnetic properties.

As was mentioned earlier, Curie temperatures T_c for Mn_2NiGa and Mn_2NiSn are quite high and therefore, promising. Using the exchange interactions, we now calculate the T_c of these materials in two different configurations, **OC** and **DC** using Mean-field approximation [266, 267]. The results are presented in T 6.6.

T 6.6: The calculated Curie temperatures (T_c) in K for Mn_2NiX systems in **OC** and in **DC** configurations.

System	**OC**	**DC**
Mn_2NiGa	797	410
Mn_2NiIn	681	340
Mn_2NiSn	542	240

The results show that the Curie temperatures calculated in the **DC** configuration agree much better with the experimental results [103] than that calculated in the **OC** configuration for Mn_2NiGa. Our results also agree closely with the reported data in Ref. [261]. Although no experimental result on T_c of Mn_2NiIn is available so far T_c of $Mn_2Ni_{1+x}In_{1-x}$ have been experimentally measured in the range of x=0.5-0.6 and they are found to vary only little and stay close to 350 K [268]. Our results in the **DC** configuration, thus, have an excellent agreement. In case of Mn_2NiSn, our results from **OC** configuration are surprisingly close to the experimental value of T_c [269] while that calculated in the **DC** configuration is rather low. This can be because of a sublattice ordering in the experimental sample different than the considered **DC** configuration here. Our results have already suggested that the values of T_c are extremely sensitive to the state of order as the exchange configurations are modified substantially between configurations. Overall, the calculated T_c in the **DC** configurations agree reasonably well with the experimental trends.

6.4 Summary

With the aid of *ab initio* calculations, we have investigated compositional and structural stabilities along with the magnetic properties of inverse Heusler Mn_2NiX alloys in connection with the improvement of shape memory and magnetocaloric effects. We find that the out of

the four alloys initially considered here, three are potentially better shape memory materials as a large value of ΔM can be achieved even in these compositions whereas in prototype Ni_2MnX systems, one has to vary the ratio of Ni, Mn and X judiciously to achieve the same. We also find that these materials would show inverse magneto-caloric effect, which is technologically desirable for green environment. Our investigations reveal that these properties emerge due to existence of anti-site disorder in one of the Mn and the Ni sublattices. It is also found that the electronic structures associated with the Mn atom, which makes an alloy with Ni, are primarily responsible for the dramatic changes in the magnetic properties, and consequently for improved functionalities. This work, thus, shows that the Mn_2NiX alloys in the inverse Heusler structure can be considered as potential functional materials and that more experimental verifications of their functional properties are required.

Chapter 7

Conclusions and Scopes for future work

7.1 Conclusions

In this thesis, we have investigated the potential shape memory alloy series Mn_2NiX in detail with the help of first-principles electronic structure methods. Our investigations include the study of phase stability related to shape memory effect, the study of macroscopic origin of the SME from lattice dynamics, the study of magnetic structure of the ground state and a study of the effect of anti-site disorder on functional properties.

In the first chapter, the concepts relevant to the descriptions of this class of materials such as shape memory effect, martensitic transformation, pseudoelasticity are discussed in detail along with possible applications of shape memory alloys. The nitty-gritties of MSME and the information on state-of-the-art research on MSMAs are discussed to familiarize the reader with the materials, their importances and the problems that are worth researching into.

In the next chapter, we discuss the theoretical background of the various methods that have been used in this thesis. After a brief introduction of the Density Functional Theory (DFT), the backbone for modern first-principles electronic structure based methods, we present an overview of the various implementations of DFT which have been used in this thesis.

In the following chapter, we perform detailed calculations to explore the possibility of realizing the SME in Mn_2NiX (X= Al, Ga, In, Sn) materials. A volume conserving and energy lowering phase transformation from cubic to unmodulated tetragonal structure, corresponding

to an expansion in the c-axis, confirm that all the above materials are potential shape memory alloys. The presence of shallow minima corresponding to $(c/a)< 1$ in the calculated energy curves indicate the signatures of modulated phases which could be considered precursor to the martensitic transformations. Our results on total energy curves, the magnetic moments and the electronic structures show that Mn_2NiAl and Mn_2NiGa are quite similar in their properties while Mn_2NiIn and Mn_2NiSn are different than the former but bear close resemblances among themselves.

In a bid to pinpoint the origin of the martensitic transformations in these materials, we present our results on their lattice dynamics in chapter 4. We find that all the four MSMAs show unstable transverse acoustic TA_2 phonon modes along $[\xi\xi 0]$ direction, which in conformity with the results of the previous chapter, explain the instability in the high temperature cubic phase. We explain the anomalous phonon softening from the nesting features in the minority spin Fermi surfaces. Once again, Mn_2NiAl and Mn_2NiGa show similarities in their vibrational spectra, which suggest that the instabilities associated with them are purely mechanical. These features in the phonon spectra also suggest that pre-mertensitic modulated phases indeed do occur in these materials and that these phases could be quite complicated.

In chapter 5, we investigate into the ground state magnetic structures of Mn_2NiX materials with the focus on possibilities of obtaining noncollinear spin structures. Our calculations showed that under external pressure, produced by about 3.5% compressions of the lattice constants, Mn_2NiX materials, except Mn_2NiIn, undergo a magnetic phase transformation from collinear to noncollinear structures, the later being combinations of different spin spirals. For Mn_2NiIn more compressions are necessary for stable noncollinear state. This phenomenon adds to the possible functionalities of these materials as this is a signature of magnetic barocaloric effect. We explain their volume dependent magnetic phase transformation from the analysis of band structures and nesting features in the Fermi surfaces associated with bands with different spin orientations. We also explore the effects of crystal structure and chemical compositions on the magnetic ground states and conclude that spin alignments of inequivalent Mn atoms in Mn_2NiX materials are responsible for the noncollinear states found in the calculations.

In the chapter 6, we investigate the effects of anti-site disorder on the magnetic properties and subsequent functionalities of Mn_2NiX materials. We find that a state with anti-site disorder in sublattices of tetrahedral symmetry is energetically lower than the perfect ordered

inverse Heusler state. The consequences is that magnetizations in the high temperature cubic phases increase by an order of magnitude in comparison to these in the perfectly ordered states resulting in a large value of ΔM, where ΔM is the magnetizations in the low temperature martensitic phase with respect to that in the high temperature phase. Such large and negative values of ΔM open up the possibilities of obtaining martensitic transformations on applications of small magnetic fields and significant inverse magnetocaloric effects in Mn_2NiX materials.

The contents of this thesis, thus, show various facets of Mn_2NiX materials in great detail, which have not yet been explored the way it is done here. The results of various investigations clearly show that the members of the Mn_2NiX series are indeed promising multifunctional materials and that more studies, particularly experimental ones, are required to unearth their complete potentials.

7.2 Scopes for future work

The extensions of the work presented in this thesis can be in various directions. One direction would be to investigate the tetragonal variants of these materials. In this thesis, we have clearly shown the existence of modulated tetragonal phases. A complete investigation in this direction can throw light into the sequences of phase transformation in these alloys from austenite to nonmodulated martensitic structure.

Another possible extension could be towards the calculations of thermodynamical properties and phase diagrams of these materials. In this thesis, the arguments and explanations are based upon calculations at T= 0 K. An extension of this work towards more realistic technological applications and a better understanding from scientific point of view is the inclusion of finite temperature effects. Thus, one needs to compute the free energies by including the effects of vibrational and magnetic entropies in order to estimate the thermodynamic parameters such as T_M. Such a task is challenging and computationally demanding too.

Another possible extension could be towards a comprehensive investigation on effects of chemical disorder in sublattices other than those considered here and on effects of doping of magnetic sublattices with other magnetic elements such as Co and Fe. The need for this possible extension arises due to the availability of recent experimental results which claim

that (i) the chemical disorder is present in the *X* sublattices too; at least in case of Mn_2NiGa and (ii) the doping of magnetic sublattices of Mn_2NiGa with other magnetic elements bring in substantial changes in the magnetic and thermodynamic properties. An extension of the scheme followed in this thesis would surely help understanding the complex physics that goes on in the presence of multi-sublattice disorder.

Bibliography

[1] D. C. Lagoudas (ed.), *Shape Memory Alloys: Modeling and Engineering Applications*, Springer (2008), ISBN: 978-0-387-47684-1.

[2] J. M. Sater, Society of Photo-optical Instrumentation Engineers., Society for Experimental Mechanics (U.S.), American Society of Mechanical Engineers. *Smart structures and materials 1997 Industrial and commercial applications of smart structures technologies : 4-6 March 1997, San Diego, California*., Bellingham, Wash. : Society of Photo-optical Instrumentation Engineers (1997).

[3] T. W. Duerig, K. N. Melton, D. Stoeckel and C. M. Wayman, *Engineering aspects of shape memory alloys*, Butterwort heinemann Ltd: London (1990).

[4] "Smart Materials and Structures". Official web-page URL: http://www.iop.org/EJ/journal/SMS

[5] A. Planes, L. Mañosa and A. Saxena (Eds.), *Magnetism and Structure in Functional Materials*, Springer publication, Vol. 79 (2005).

[6] T. Kakeshita, T. Fukuda, A. Saxena and A. Planes (Eds.), *Disorder and Strain-Induced Complexity in Functional Materials*, Springer publication, Vol. 148 (2012).

[7] D. J. Leo, *Engineering Analysis of Smart Material Systems*, John Wiley & Sons, Inc., Hoboken, NJ, USA (2008).

[8] Gustav Gautschi, *Piezoelectric Sensorics: Force, Strain, Pressure, Acceleration and Acoustic Emission Sensors, Materials and Amplifiers*, Springer-verlag Berlin Heidelberg New York, (2002).

[9] A. Kholkin, B. Jadidian and A. Safari, *Encyclopedia of Smart Materials*, Ceramics, Piezoelectric and Electrostrictive, Wiley Online Library (2002).

[10] Institute of Electrical and Electronics Engineers, *IEEE Standard on Magnetostrictive Materials: Piezomagnetic Nomenclature* **319**, (1971).

[11] *Handbook of Giant Magnetostrictive Materials (Electromagnetism)*, G. Engdahl and I. D. Mayergoyz (Eds.), Academic Press, 1st ed. (1999).

[12] I. A. Parinov, *Piezoceramic Materials and Devices*, Nova Science Publishers (2010).

[13] E. Fukada, *IEEE Trans. Ultrason., Ferroelectr., Freq. Control* **47**, 6 (2000).

[14] J. S. Harrison, and Z. Ounaies, *Piezoelectric Polymers, Encyclopedia Of Polymer Science and Technology*, **3** (2002).

[15] M. Ruzicka, *Electrorheological Fluids: Modeling and Mathematical Theory*, Springer, 2000 ed.

[16] N. M. Wereley, *Magnetorheology: Advances and Applications*, Royal Society of Chemistry (2003).

[17] A. Ölander, *J. Am. Chem Soc* **54**, 3819 (1932).

[18] A. B. Greninger and V. G. Mooradian, *Trans. Amer. Inst. Min. (Metall.) Engrs.* **128**, 337 (1938).

[19] A. B. Greninger, *Trans. Amer. Inst. Min. (Metall.) Engrs.* **133**, 204 (1939).

[20] L. B. Vernon and H. M. Vernon, "*Process of manufacturing articles of thermoplastic synthetic resins*", US Patent 2234993, (1941).

[21] W. J. Buehler, J. W. Gilfrich and R. C. Wiley, *J. Appl. Phys.* **34**, 475 (1963).

[22] F. E. Wang, W. J. Buehler and S. J. Pickart, *J. Appl. Phys.* **36**, 3232 (1965).

[23] "The Alloy That Remembers", *Time*, September **13**, 1986. Retrieved October 8, 2008. http://www.time.com/time/magazine/article/0,9171,838687,00.html

[24] C. M. Wayman, *Introduction to the crystallography of martensitic transformations*, MacMillan, New York, 1964.

[25] C. M. Wayman, *J. Less. Common. Met.* **28**, 97 (1972).

[26] E. C. Bain and N. Y. Dunkirk, *Trans. AIME* **70**, 25 (1924).

[27] A. T. Zayak, *A first-principles investigation of the magnetic, structural and dynamical properties of Ni_2MnGa*, Ph. D Thesis, November (2003).

[28] H. K. D. H. Bhadeshia, *http://www.msm.cam.ac.uk/phase-trans/2002/martensite.html*

[29] C. M. Wayman, *Mater. Sci. Forum* **56-58**, 1 (1990).

[30] K. Otsuka and C. M. Wayman (Eds.), *Shape memory materials*, Cambridge University Press , United Kingdom (1998).

[31] G. Grimval, *Thermophysical Properties of Materials*, North Holland, Netherlands (1999).

[32] A. K. Jena and M. C. Chaturvedi, *Phase Transformation in Materials*, Prentice Hall, New York (1992).

[33] Z. Nishiyama, *Martensitic Transformation*, Academic, New York (1978).

[34] Z. Nishiyama, *Sci. Rep. Tohoku Imp. Univ.* **23**, 637 (1934).

[35] G. V. Kurdjumov and G. Sachs, *Z. Phys.* **64**, 325 (1930).

[36] E. Hoffmann, H. Herper, P. Entel, S. G. Mishra, P. Mohn and K. Schwarzn, *Phys. Rev. B* **47**, 5589 (1993).

[37] A. Bekker and L. C. Brinson, *Acta Mater.* **46**, 3649 (1998).

[38] L. C. Brinson, *J. Intell. Mater. Syst.* **4**, 229 (1993).

[39] Y. Yamada, *Phys. Rev. B* **46**, 5906 (1992).

[40] G. Kauffman and Isaac Mayo, *"Memory Metal." Chem Matters Oct.* **4-7** (1993).

[41] D. Stöeckel, *The Shape Memory Effect- Phenomenon, Alloys and Applications*, Proceedings: Shape Memory Alloys for Power Systems EPRI, pp. 1-13 (1995).

[42] J. H. Mulder *et al.*, *On the High Temperature Shape Memory Capabilities of Ni-(TiZr) and Ni-(TiHf) Alloys*, *Proc. of SMST.* (A. R. Pelton, el al. eds.) (1995).

[43] D. Stöeckel and T. Borden, *Metall* **46**, 668 (1992).

[44] D. Stöeckel, *Springs* **30**, 35 (1991).

[45] A. R. Pelton, D. Stöckel and T. W. Duerig, *Mat. Sci. Forum* **327-328**, 63-70 (2000).

[46] T. Duerig, A. Pelton and D. Stöckel, *Mat. Sci. Eng. A* **273-275**, 149 (1999).

[47] J. P. Joule, *Annals of Electricity, Magnetism, and Chemistry* **8**, 219224 (1842).

[48] J. P. Joule, *The London, Edinburgh and Dublin philosophical magazine and journal of science (Taylor and Francis).* 30, Third Series: **76-87**, 225241 (1847).

[49] A. E. Clark, *Ferromagnetic Materials*, E. P. Wohlfarth (ed.), North-Holland, Amsterdam, Vol. **1**, 531-589 (1980).

[50] S. J. Murray, M. Marioni, S. M. Allen, R. C. O'Handley, and T. A. Lograsso, *Appl. Phys. Lett.* **77**, 886 (2000).

[51] O. Heczko, A. Sozinov and K. Ullakko, *IEEE Trans. Magn.* **36**, 3266 (2000).

[52] A. Sozinov, A. A. Likhachev, N. Lanska and K. Ullakko, *Appl. Phys. Lett.* **80**, 1746 (2002).

[53] R. Tickle, R. D. James, T. Shield, M. Wuttig and V. V. Kokorin, *IEEE Trans. Magn.* **35**, 4301 (1999).

[54] Q. Pan and R. D. James, *J. Appl. Phys.* **87**, 4702 (2000).

[55] Y. W. Lai, N. Scheerbaum, D. Hinz, O. Gutfleisch, R. Schäfer, L. Schultz and J. McCord, *Appl. Phys. Lett.* **90**, 192504 (2007).

[56] A. Planes, L. Mañosa and M. Acet, *J. Phys.: Condens. Matter* **21**, 233201 (2009).

[57] A. Hubert and R. Schäfer, *Magnetic domains: the analysis of magnetic microstructures*, Springer-Verlag, GmbH, Germany (1998).

[58] R. C. O'Handley, *Modern Magnetic Materials: Principles and Applications*, Wiley, New York (2000).

[59] K. Ullakko, J. K. Huang, C. Kanter, V. V. Kokorin and R. C. O'Handley, *Appl. Phys. Lett.* **69**, 1966 (1996).

[60] P. J. Webster, K. R. A. Ziebeck, S. L. Town, and M. S. Peak, *Philo. Mag. B* **49**, 295 (1984).

[61] P. J. Webster, *Contemp. Phys.* **10**, 559 (1969).

[62] P. J. Webster and K. R. A. Ziebeck, *J. Phys. Chem. Solids.* **34**, 1647 (1973).

[63] B.Wedela, M. Suzukia, Y. Murakamia, C. Wedela, T. Suzukib, D. Shindoa and K. Itagakia, *J. Alloy. Compd.* **290**, 137 (1999).

[64] V. V. Martynov and V. V. Kokorin, *J. Phys. III (France)* **2**, 739 (1992).

[65] P. J. Brown, J. Crangle, T. Kanomata, M. Matsumoto, K. -U. Neumann, B. Ouladdiaf and K. R. A Ziebeck, *J. Phys.: Condens. Matter.* **14**, 10159 (2002).

[66] J. Pons, V. A. Chernenko, R. Santamarta and E. Cesari, *Acta Mater.* **48**, 3027 (2000).

[67] V. A. Chernenko and V. V. Kokorin, *Proceedings of the International Conference on Martensitic Transformations*, (ICOMAT-92, Monterey). (Monterey Institute for Advanced Studies, 1993), p. 1205.

[68] V. V. Martynov, *J. Physique IV* **5**, C8-91 (1995).

[69] A. N. Vasilev, A. D. Bozhko, V. V. Khovailo, I. E. Dikshtein, V. G. Shavrov, V. D. Buchelnikov, M. Matsumoto, S. Suzuki, T. Takagi and J. Tani, *Phys. Rev. B* **59**, 1113 (1999).

[70] A. Zheludev, S. Shapiro, P.Wochner, A. Schwartz, M. Wall and L. Tanner, *Phys. Rev. B* **51**, 11310 (1995).

[71] Y. Ma, S. Awajia, K. Watanabea, M. Matsumotob and N. Kobayashia, *Solid. State. Commun.* **113**, 671 (2000).

[72] J. Marcos, A. Planes, L. Mañosa, F. Casanova, X. Batlle and A. Labarta, *Phys. Rev. B* **66**, 224413 (2002).

[73] C. Biswas, R. Rawat and S. R. Barman, *Appl. Phys. Lett.* **86**, 202508 (2005).

[74] R. J. McQueeney, Y. Petrov, T. Egami, G. Shirane and Y. Endoh, *Phys. Rev. Lett.* **82**, 628 (1999).

[75] G. Shirane and Y. Yamada, *Phys. Rev.* **177**, 858 (1969).

[76] D. Louca, T. Egami, E. L. Brosha, H. Röder and A. R. Bishop, *Phys. Rev. B* **56**, R8475 (1997).

[77] W. Reichardt and M. Braden, *Physica B* **263-264**, 416 (1999).

[78] A. Planes and L. Mañosa, *Solid State Phys.* **88**, 159 (2001); and references therein.

[79] Z. Jincang, L. Lihua, D. Cheng, L. Jianqi, C. Hong, L. Xigui and C. Guosheng, *Phys. Rev. B* **65**, 54513 (2002).

[80] J. M. Tranquada, B. J. Sternlieb, J. D. Axe, Y. Nakamura and S. Uchida *Nature* **375**, 561 (1995).

[81] X. Meng, K. Z. Baba-Kishi, G. K. H. Pang, H. L. Chang, C. L. Choy and H. S. Luo, *Phil. Mag. Lett.* **84**, 191 (2004).

[82] L. Tanner, *Phil. Mag.* **14**, 111 (1966).

[83] S. M. Shapiro, J. Z. Larese, Y. Noda, S. C. Moss and L. E. Tanner, *Phys. Rev. Lett.* **57**, 3199 (1986).

[84] J. Friedel, *J. Phys. (Paris) Lett.* **35**, L59 (1974).

[85] P. A. Lindgård and O. G. Mouritsen, Phys. Rev. Lett. **57**, 2458 (1986).

[86] C. Zener, *Phys. Rev.* **71**, 846 (1947).

[87] G. L. Zhao and B. N. Harmon, *Phys. Rev. B* **45**, 2818 (1992).

[88] G. L. Zhao and B. N. Harmon, Phys. Rev. B **48**, 2031 (1993).

[89] S. M. Shapiro, B. X. Yang, Y. Noda, L. E. Tanner and D. Schryvers, *Phys. Rev. B* **44**, 9301 (1991).

[90] P. W. Anderson, *Qualitative considerations on the statistics of the phase transition in batio$_3$-type ferroelectrics* In: Fizika Dielekrikov, ed. by G.I. Skanavi, Academia Nuak, Moscow, USSR, (1960), pp. 290295.

[91] W. Cochran, *Adv. Phys.* **9**, 387 (1960).

[92] A. Zheludev , S. Shapiro, P. Wochner and L. Tanner, *Phys. Rev. B* **54**, 15045 (1996).

[93] A. N. Vasil'ev, E. I. Estrin, V. V. Khovailo, A. D. Bozhko, R. A. Ischuk, M. Matsumoto, T. Takagi and J. Tani, *J. Phys.: Condens. Matter* **13**, 9655 (2001).

[94] F. Zuo, X. Su and K. Wu, *Phys. Rev. B* **58**, 11127 (1998).

[95] G. L. Zhao and B. N. Harmon, *Phys. Rev. B* **45**, 2818 (1992).

[96] A. Planes, E. Obrado, A. Gonzales-Comas and L. Mañosa, *Phys. Rev. Lett.* **79**, 3926 (1997).

[97] A. N. Vasil'ev, A. D. Bozhko, V. V. Khovailo, I.E. Dikshtein, V. G. Shavrov, V. D. Buchelnikov, M. Matsumoto, S. Suzuki, J. Takagi, and J. Tani, *Phys. Rev. B* **59**, 1113 (1999)..

[98] T. Büsgen, J. Feydt, R. Hassdorf, S. Thienhaus, M. Moske, M. Boese, A. Zayak, and P. Entel, *Phys. Rev. B* **70**, 014111 (2004).

[99] V. V. Godlevsky and K. M. Rabe, *Phys. Rev. B* **63**, 134407 (2001).

[100] T. Krenke, M. Acet and E. F. Wassermann, *Phys. Rev. B* **73**, 174413 (2006).

[101] T. Krenke, M. Acet, E. F. Wassermann, X. Moya, L. Mañosa and A. Planes, *Phys. Rev. B* **72**, 014412 (2005).

[102] R. B. Helmholdt and K. H. J. Buschow, *J. Less. Common. Met.* **128**, 167 (1987).

[103] G. D. Liu, J. L. Chan, Z. H. Liu, X. F. Dai and G. H. Wu, *Appl. Phys. Lett.* **87**, 262504 (2005).

[104] G. D. Liu, X. F. Dai, S. Y. Yu, Z. Y. Zhu, J. L. Chen, and G. H. Wu, *Phys. Rev. B* **74**, 054435 (2006).

[105] S. Singh, M. Maniraj, S. W. D'Souza, R. Ranjan and S. R. Barman, *Appl. Phys. Lett.* **96**, 081904 (2010).

[106] P. J. Brown, T. Kanomata, K. Neumann, K. -U. Neumann, B. Ouladiaff, A. Sheikh and K. R. A. Ziebeck, *J. Phys.: Condens. Matter* **22**, 506001 (2010).

[107] L. Ma, W. H. Wang, C. M. Zhen, D. L. Hou, X. D. Tang, E. K. Liu and G. H. Wu, *Phys. Rev. B* **84**, 224404 (2011).

[108] H. Luo, G. Liu, Z. Feng, Y. Li, L. Ma, G. Wu, X. Zhu, C. Jiang, and H. Xu, J. Magn. Magn. Mater. **321**, 4063 (2009).

[109] P. Hohenberg and W. Kohn, *Phys. Rev. B* **136**, B864 (1964).

[110] R. M. Martin, *Electronic structure: Basic theory and Practical Methods*, Cambridge University Press, United Kindom (2004).

[111] W. Kohn and L. J. Sham, *Phys. Rev. B* **140**, A1133 (1965).

[112] P. Schwerdtfeger, *Chem. Phys. Chem.* **12**, 3143 (2011).

[113] D. J. Singh and L. Nordström, *Plane waves, pseudopotentials and the LAPW method*, 2nd Ed., Springer Publication, New York, (2004).

[114] T. L. Loukes, *The Augmented-Plane-Wave Method*, Benjamin, New York, (1967).

[115] J. C. Slater, *Phys. Rev.* **51**, 846 (1937).

[116] J. C. Slater, *Advan. Quantum Chem.* **1**, 35 (1964).

[117] O. K. Andersen, *Phys. Rev. B* **12**, 3060 (1975).

[118] J. Korringa, *Physica XII* **13**, 392 (1947).

[119] W. Kohn and N. Rostoker, *Phys. Rev.* **94**, 1111 (1954).

[120] L. Hedin, *Phys. Rev.* **139**, A796 (1965).

[121] J. Kubler, K. -H. Hock, J. Sticht and A. R. Williams, *J. Phys. F: Met. Phys.* **18**, 469 (1988).

[122] L. M. Sandratskii, *Advan. Phys.* **47**, 91 (1998).

[123] L. Nordström and D. J. Singh, *Phys. Rev. Lett.* **76**, 4420 (1996).

[124] D. Hobbs, G. Kresse and J. Hafner, *Phys. Rev. B* **62**, 11556 (2000).

[125] M. J. Stott and E. Zaremba, *Phys. Rev. A* **21**, 12 (1980).

[126] S. Y. Savrasov, *Phys. Rev. B* **54**, 16470 (1996).

[127] S. Baroni, S. de Gironcoli, A. Dal Corso and P. Giannozzi, *Rev. Mod. Phys.* **73**, 515 (2001).

[128] I. Turek, V. Drchal, J. Kudrnovsky, M. Sob and P. Weinberger, *Electronic Structure of Disordered Alloys, Surfaces and Interfaces*, Springer; 1997 ed..

[129] A. Jezierski, *J. Magn. Magn. Mater.* **140-144**, 91 (1995).

[130] C. M. da Silvaa, D.E. Brandćob and A. A. Gomes, *J. Magn. Magn. Mater.* **62**, 160 (1996).

[131] R. McCormack and D. de Fontaine, *Phys. Rev. B* **54**, 9746 (1996).

[132] A. Bansil, S. Kaprzyk, P. E. Mijnarends, and J. Tobola, *Phys. Rev. B* **60**, 13396 (1999).

[133] G. H. Fecher, H. C. Kandpal, S. Wurmehl, J. Morais, Hong-Ji Lin, H. J. Elmers, G. Schönhense and C. Felser, *J. Phys.: Condens. Matter.* **17**, 7237 (2005).

[134] V. N. Antonov, H. A. D ̄urr, Yu. Kucherenko, L. V. Bekenov and A. N. Yaresko, *Phys. Rev. B* **72**, 054441 (2005).

[135] Y. Miura, K. Nagao and M. Shirai, *Phys. Rev. B* **69**, 144413 (2004).

[136] M. Born and R. Oppenheimer, *Ann. Phys. (Leipzig)* **84** (20), 457 (1927).

[137] J. P. Perdew and Y. Wang, *Phys. Rev. B* **33**, 8800 (1986); **40**, 3399(E) (1989).

[138] J. P. Perdew, *Electronic Structure of Solids 91* edited by P. Ziesche and H. Eschrig, Akademie Verlag, Berlin, (1991) p. 11.

[139] Y. Zhang and W. Yang, *Phys. Rev. Lett.* **80**, 890 (1998).

[140] R. Armiento and A. E. Mattsson, *Phys. Rev. B* **72**, 085108 (2005).

[141] Z. Wu and R. E. Cohen, *Phys. Rev. B* **73**, 235116 (2006).

[142] J. P. Perdew, A. Ruzsinszky, G. I. Csonka, O. A. Vydrov, G. E. Scuseria, L. A. Constantin, X. Zhou and K. Burke, *Phys. Rev. Lett.* **100**, 136406 (2008).

[143] A. D. Becke, *J. Chem. Phys.* **98**, 1372 (1993).

[144] K. Kim and K. D. Jordan, *J. Phys. Chem.* **98**, 10089 (1994).

[145] J. Heyd, G. E. Scuseria and M. Ernzerhof, *J. Chem. Phys.* **118**, 8207 (2003).

[146] C. Herring, *Phys. Rev.* **57**, 1169 (1940).

[147] T. Starkloff and J. D. Joannopoulos, *Phys. Rev. B* **16**, 5212 (1977).

[148] W. C. Topp and J. J. Hopfield, *Phys. Rev. B* **7**, 1295 (1973).

[149] D. Vanderbilt, *Phys. Rev. B* **41**, 7892 (1990).

[150] K. Laasonen, R. Car, C. Lee and D. Vanderbilt, *Phys. Rev. B* **43**, 6796 (1991).

[151] K. Laasonen, A. Pasquarello, R. Car, C. Lee and D. Vanderbilt, *Phys. Rev. B* **47**, 10142 (1993).

[152] P. E. Blöchl, *Phys. Rev. B* **50**, 17953 (1994).

[153] A. Gonis, *Green functions for ordered and disordered systems*, North-Holland, (1992).

[154] O. K. Andersen, O. Jepsen, and G. Krier, *Lectures on Methods of Electronic Structure Calculation*, World Scientific, Singapore, (1994), p. 63.

[155] L. Vitos, *The EMTO Method and Applications, in Computational Quantum Mechanicals for Materials Engineers*, Springer-Verlag, London, (2007).

[156] L. Vitos, I. A. Abrikosov and B. Johansson, *Phys. Rev. Lett.* **87**, 156401 (2001).

[157] L. Vitos, Johansson. B, J. Kollar and H. L. Skriver, *Phys. Rev. B.* **62**, 10046 (2000).

[158] L. Vitos, H. L. Skriver, B. Johansson, and J. Kollár, *Comput. Mater. Sci.* **18**, 24 (2000).

[159] E. Wigner and F. Seitz, *Phys. Rev.* **43**, 804 (1933).

[160] O. K. Andersen, *Solid State Commun.* **13**, 133 (1973).

[161] L. Vitos, J. Kollár and H. L. Skriver, *Phys. Rev. B* **55**, 13521 (1997).

[162] L. Vitos, J. Kollár and H. L. Skriver, *Phys. Rev. B* **49**, 16694 (1994).

[163] J. Kollár, L. Vitos and H. L. Skriver, *Phys. Rev. B* **49**, 11288 (1994).

[164] D. Shin, *Thermodynamic properties of solid solution from Special Quasirandom*, Ph. D thesis, May 2007.

[165] P. Soven, *Phys. Rev.* **156**, 809 (1967).

[166] D. W. Taylor, *Phys. Rev.* **156**, 1017 (1967).

[167] A. Zunger, S. -H. Wei, L. Ferreira and J. E. Bernard, *Phys. Rev. Lett.* **65**, 353 (1990).

[168] S.-H. Wei, L. G. Ferreira, J. E. Bernard and A. Zunger, *Phys. Rev. B* **42**, 9622 (1990).

[169] K. C. Hass, L. C. Davis and A. Zunger, *Phys. Rev. B* **42**, 3757 (1990).

[170] Z. W. Lu, S.-H. Wei and A. Zunger, *Phys. Rev. B* **44**, 10470 (1991).

[171] Z. W. Lu, S.-H. Wei and A. Zunger, *Phys. Rev. B* **45**, 10314 (1992).

[172] V. Ozolins, C. Wolverton and A. Zunger, *Phys. Rev. B* **57**, 6427 (1998).

[173] A. V. Ruban, S. I. Simak, P. A. Korzhavyi and H. L. Skriver, *Phys. Rev. B* **66**, 024202 (2002).

[174] C. Wolverton, *Acta Mater* **49**, 3129 (2001).

[175] B. Dutta *First-principles based computation of lattice dynamics in substitutionally disordered alloys*, Ph. D thesis, August 2011.

[176] S. Paul and S. Ghosh, *J. Phys.: Condens. Matter* **23**, 206003 (2011).

[177] S. Paul and S. Ghosh, *J. Appl. Phys.* **110**, 063523 (2011).

[178] S. R. Braman, S. Banik, A. K. Shukla, C. Kamal and A. Chakrabarti, *Europhys. Lett.* **80**, 57002 (2007).

[179] H. Luo, G. Liu, F. Meng, S. Li, W. Zhu, G. Wu, X. Zhu, and C. Jiang, Physica B **405**, 3092 (2010).

[180] A. Chakrabarti and S. R. Barman, *Appl. Phys. Lett.* **94**, 161908 (2009).

[181] V. A. Chernenko, J. Pons, C. Segui, and E. Cesari, *Acta Mater.* **50**, 53 (2002).

[182] A. T. Zayak, W. A. Adeagabo, P. Entel, and K. M. Rabe, Appl. Phys. Lett. **88**, 111903 (2006).

[183] L. Nordström and D. J. Singh, *Phys. Rev. Lett.* **76**, 4420 (1996).

[184] L. Nordström and A. Mavromas, *Europhys. Lett.* **49**, 775 (2000).

[185] http://elk.sourceforge.net/

[186] J. P. Perdew, K. Burke and M. Ernzerhorf, *Phys. Rev. Lett.* **77**, 3865 (1996).

[187] P. Giannozzi, S. Baroni, N. Bonini, M. Calandra, R. Car, C. Cavazzoni, D. Ceresoli, G. L. Chiarotti, M. Cococcioni, I. Dabo, A. Dal Corso, S. de Gironcoli, S. Fabris, G. Fratesi, R. Gebauer, U. Gerstmann, C. Gougoussis, A. Kokalj, M. Lazzeri, L. Martin-Samos, N. Marzari, F. Mauri, R. Mazzarello, S. Paolini, A. Pasquarello, L. Paulatto, C. Sbraccia, S. Scandolo, G. Sclauzero, A. P. Seitsonen, A. Smogunov, P. Umari and R. M. Wentzcovitch, *J. Phys.: Condens. Matter* **21**, 395502 (2009).

[188] G. Kresse and J. Furthmuller, *Phys. Rev. B* **54**, 11169 (1996).

[189] G. Kresse and D. Joubart, *Phys. Rev. B* **59**, 1758 (1999).

[190] http://www.vasp.at/

[191] D. Vanderbilt, *Phys. Rev. B* **41**, 7892 (1990).

[192] S. G. Louie, S. Froyen and M. L. Cohen, *Phys. Rev. B* **26**, 1738 (1982).

[193] J. P. Perdew, *Electronic Structure of Solids* P. Ziesche and H. Eschrig (Eds.), Akademic Verlag, Berlin , (1991) pg. 11.

[194] H. Ebert, D. Ködderitzsch and J. Minar, *Rep. Prog. Phys.* **74**, 096501 (2011).

[195] see http://olymp.cup.uni-muenchen.de/ak/ebert/SPRKKR. SPR-KKR is a high quality Density Functional Theory based electronic srtucture code, co-ordinated by H. Ebert.

[196] A. V. Ruban and H. L. Skriver, *Phys. Rev. B* **66**, 024201 (2002).

[197] S. R. Barman and A. Chakrabarti, *Phys. Rev. B* **77** 176401 (2008).

[198] A. T. Zayak, P. Entel, J. Enkovaara, A. Ayuela, and R. M. Nieminen, *J. Phys.: Condens. Matter* **15**, 159 (2003).

[199] J. Enkovaara, O. Heczko, A. Ayuela, and R. M. Nieminen, *Phys. Rev. B* **67**, 212405 (2003).

[200] Q. Hu, C. Li, R. Yang, S. E. Kulkova, D. I. Bazhanov, B. Johansson and L. Vitos, *Phys. Rev. B* **79**, 144112 (2009).

[201] I. Galanakis, and E. Şaşioğlu, *Appl. Phys. Lett.* **98**, 102514 (2011).

[202] S. Paul, B. Sanyal and S. Ghosh, *J. Phys.: Condens. Matter* **27**, 035401 (2015).

[203] L. Mañosa, A. Planes, J. Zarestky, T. Lograsso, D. L. Schlagel and C. Stassis, *Phys. Rev. B* **64**, 024305 (2001).

[204] A. T. Zayak and P. Entel, *J. Magn. Magn. Mater.* **290-291** 874 (2005).

[205] X. Moya, L. Mañosa, A. Planes, T. Krenke, M. Acet, V. O. Garlea, T. A. Lograsso, D. L. Schlagel and J. L. Zarestky *Phys. Rev. B* **73**, 064303 (2006).

[206] S. Ağduk and G. Gökoğlu, *Eur. Phys. J. B* **79**, 509 (2011).

[207] S. Ağduk and G. Gökoğlu, *J. Alloys Compd.* **511**, 9 (2012).

[208] H. Hellmann, *Einfuhrung in die Quantenchemie Deuticke*, Leipzig (1937).

[209] R. P. Feynman, *Phys. Rev.* **56**, 340 (1939).

[210] A. Messiah, *Quantum Mechanics*, North-Holland, Amsterdam (1962).

[211] M. Methfessel and A. T. Paxton, *Phys. Rev. B* **40**, 3616 (1989).

[212] A. T. Zayak, P. Entel, K. M. Rabe, W. A. Adeagbo and M. Acet, *Phys. Rev. B* **72**, 054113 (2005).

[213] Y. Lee, J. Y. Rhee and B. N. Harmon, *Phys. Rev. B* **66**, 054424 (2002).

[214] C. Bungaro, K. M. Rabe and A. Dal Corso, *Phys. Rev. B* **68**, 134104 (2003).

[215] O. I. Velikokhatnyi and I. I. Naumov, *Phys. Solid State* **41**, 617 (1999).

[216] P. Entel, V. D. Buchelnikov, M. E. Gruner, A. Hucht, V. V. Khovailo, S. K. Nayak and A. T. Zayak, *Mater. Sci. Forum* **583**, 21 (2008).

[217] M. Siewert, M. E. Gruner, A. Dannenberg, A. Hucht, S. M. Shapiro, G. Xu, D. L. Schlagel, T. A. Lograsso and P. Entel, *Phys. Rev. B* **82**, 064420 (2010).

[218] Z. Jian-Tao, Z. Kun, W. Jia-Jia, Y. Xin-Quan, Y. Jin and W. San-Xie, *Acta. Phys. Sin.* **61** 213102 (2012).

[219] M. Born and K. Huang, *Dynamical Theory of Crystal Lattices,* (Clarendon, Oxford, 1956).

[220] K. Otsuka and X. Ren, *Progress in Materials Science*, **50**, 511 (2005).

[221] T. Černoch, M. Landa, P. Novák, P. Sedlák and P. Šittner, *J. Alloys. compd.* **378**, 140 (2004).

[222] S. M. Shapiro, G. Xu, G. Gu, J. Gardner and R. W. Fonda, Phys. Rev. B **73**, 214114 (2006).

[223] S. M. Shapiro, G. Xu, B. L. Winn, D. L. Schlagel, T. Lograsso and R. Erwin, *Phys. Rev. B* **76**, 054305 (2007).

[224] A. Planes and L. Mañosa, *Solid State Phys.* **55**, 159 (2001).

[225] S. Paul, S. Ghosh and B. Sanyal, *J. Phys.: Condens. Matter* **26**, 196004 (2014).

[226] Y. Tsunoda, *J. Phys. F* **18**, L251 (1988).

[227] C. Zhoua and C. D. Gong, *Phys. C* **169**, 245 (1990).

[228] E. Arrigoni, G. C. Strinati and M. Geddo, *Phys. C* **185**, 1691 (1990).

[229] E. Dagotto, A. Moreo, F. Ortolani, D. Poilblanc and J. Riera, *Phys. Rev. B* **45**, 10741 (1992).

[230] I. Ichinose and T. Matsui, *Phys. Rev. B* **45**, 9976 (1992).

[231] A. P. Kampf and W. Brenig, *J. Low Temp. Phys.* **95**, 335 (1994).

[232] N. Hasselmann, A. H. Castro Neto and C. Morais Smith, *Europhys. Lett.* **56**, 870 (2001).

[233] N. Hasselmann, A. H. Castro Neto and C. Morais Smith, *Phys. Rev. B* **69**, 014424 (2004).

[234] V. Juricic, L. Benfatto, A. O. Caldeira, and C. Morais Smith, *Phys. Rev. Lett.* **92**, 137202 (2004).

[235] V. Juricic, L. Benfatto, A. O. Caldeira, and C. Morais Smith, *Phys. Rev. B* **71**, 064421 (2005).

[236] A. Lüscher, A. I. Milstein, and O. P. Sushkov, *Phys. Rev. Lett.* **98**, 037001 (2007).

[237] N. Choudhury, L. Walizer, S. Lisenkov and L. Bellaiche, *Nature* **470**, 513 (2011).

[238] M. Liebs, K. Hummler, and M. Fähnle, *Phys. Rev. B* **51**, 8664(R) (1995).

[239] R. Lorenz, J. Hafner, S. S. Jaswal, and D. J. Sellmyer, *Phys. Rev. Lett.* 74, 3688 (1995).

[240] R. Lorenz and J. Hafner, *Appl. Phys.* **79**, 5051 (1996).

[241] J. Schliemann, *Phys. Rev. B* **67**, 045202 (2003).

[242] H. J. Xiang, C. Lee, and M. -H. Whangbo, *Phys. Rev. B* **76**, 220411(R) (2007).

[243] J. Hafner and R. Lorenz, *Comput. Mater. Sci.* **8**, 170 (1997).

[244] H. Nagasawa and S. Murayama, *J. Magn. Magn. Mater.* **15-18**, 93 (1980).

[245] T. Asada, *J. Magn. Magn. Mater.* **140-144**, 47 (1995).

[246] D. Hobbs and J. Hafner, *J. Phys.: Condens. Matter* **13**, L681 (2001).

[247] D. Hobbs and J. Hafner, *Phys. Rev. B* **68**, 014408 (2003).

[248] John F. Drain, Ralf Drautz, and D. G. Pettifor, *Phys. Rev. B* **89**, 134102 (2014).

[249] R. Lizárraga, L. Nordström, O. Eriksson, and John Wills, *Phys. Rev. B* **78**, 064410 (2008).

[250] Y. O. Kvashnin, S. Khmelevskyi, J. Kudrnovský, A. N. Yaresko, L. Genovese, and P. Bruno, *Phys. Rev. B* **86**, 174429 (2012).

[251] T. Shimada, J. Okuno and T. Kitamura, *Phys. Rev. B* **85**, 134440 (2012).

[252] B. Sanyal, O. Eriksson and C. Aron, *Phys. Rev. B* **74**, 184401 (2006).

[253] S. Prosandeev, L. Bellaiche and J. Íñiguez, *Phys. Rev. B* **85**, 214431 (2012).

[254] J. Enkovaara, A. Ayuela, J. Jalkanen, L. Nordström and R. M. Nieminen, *Phys. Rev. B* **67**, 054417 (2003).

[255] A. I. Liechtenstein, M. I. Katsnelson and V. A. Gubanov, *J. Phys. F* **14**, L125 (1984).

[256] A. I. Liechtenstein, M. I. Katsnelson, V. P. Antropov and V. A. Gubanov, *J. Magn. Magn. Mater* **67**, 65 (1987).

[257] M. Methfessel and J. Kübler, *J. Phys. F: Met. Phys.* **12**, 141 (1982).

[258] R. Lizárraga, L. Nordström, L. Bergqvist, A. Bergman, E. Sjöstedt, P. Mohn and O. Eriksson, *Phys. Rev. Lett.* **93**, 107205 (2004).

[259] S. Paul, B. Sanyal and S. Ghosh, *J. Phys.: Condens. Matter* **25**, 236005 (2013).

[260] S. Paul, A. Kundu, B. Sanyal and S. Ghosh, *J. Appl. Phys.* **116**, 133903 (2014).

[261] S. W. D'Souza, A. Chakrabarti and S. R. Barman, http://arXiv.org/abs/1310.6130v1 (2013).

[262] S. H. Vosko, L. Wilk and M. Nusair, *Can. J. Phys.* **58**, 1200 (1980).

[263] A. Van de Walle, P. Tiwary, M. de Jong, D. L. Olmsted, M. Asta, A. Dick, D. Shin, Y. Wang, L. Q. Chen and Z. K. Liu, CALPHAD **42**, 13 (2013).

[264] G. Grimvall, *Phys. Scr.* **13**, 59 (1976).

[265] P. Söderlind and B. Johansson, *Thermochim. Acta* **218**, 145 (1993).

[266] E. Sasioglu, L. M. Sandratskii and P. Bruno, *Phys. Rev. B* **70**, 024427 (2004).

[267] J. Rusz, L. Bergqvist, J. Kudrnovsky and I. Turek, *Phys. Rev. B* **73**, 214412 (2006).

[268] D. N. Lobo, S. Dwivedi, C. A. Desilva, N. O. Moreno, K. R. Priolkar and A. K. Nigam, *J. Appl. Phys.* **114**, 173910 (2013).

[269] K. H. J. Buschow, P. G. van Engen and D. B. de Mooij, *J. Magn. Magn. Mater.* **40**, 339 (1984).

Publications

Peer-reviewed journals

1. **Souvik Paul** and Subhradip Ghosh, First-principles prediction of shape memory behavior and ferrimagnetism in Mn_2NiSn, *J. Phys.: Condens. Matter* **23**, 206003 (2011).
2. **Souvik Paul** and Subhradip Ghosh, First-principles investigations of the electronic structure and properties related to shape-memory behavior in Mn_2Ni*X* (*X*= Al, Ga, In, Sn) alloys, *J. Appl. Phys.* **110**, 063523 (2011).
3. **Souvik Paul**, Subhradip Ghosh and Biplab Sanyal, Magnetic properties of Mn_2NiSn shape memory alloy, *J. Phys.: Condens. Matter 25*, 236005 (2013).
4. **Souvik Paul**, Subhradip Ghosh and Biplab Sanyal, Emergence of spin spiral magnetic order in Mn based inverse Heusler alloys, *J. Phys.: Condens. Matter* **26**, 196004 (2014).
5. **Souvik Paul**, Ashis Kundu, Biplab Sanyal and Subhradip Ghosh, Anti-site disorder and improved functionalities of Mn_2Ni*X* (*X*= Al, Ga, In, Sn) alloys with inverse Heusler structure, *J. Appl. Phys.* **116**, 133903 (2014).
6. **Souvik Paul**, Biplab Sanyal and Subhradip Ghosh, First-principles study of the lattice instabilities in Mn_2Ni*X* (*X*= Al, Ga, In, Sn) magnetic shape memory alloys, *J. Phys.: Condens. Matter* **27**, 035401 (2015).

Conference Proceedings

1. **Souvik Paul** and Subhradip Ghosh, Effects of chemical disorder on magnetism in inverse Heusler alloy Mn_2NiSn, *AIP Conf. Proc.*, **1512**, 1258 (2013).

Conferences

1. **Souvik Paul**, Biswanath Dutta and Subhradip Ghosh, *A Density Functional Theory based prediction of shape memory effect and magnetic structure in Mn_2NiSn*, "Condensed Matter Days 2011 (CMDAYS'11)" at Gauhati University, Guwahati, India August 24-26, 2011.

2. Biswanath Dutta, **Souvik Paul** and Subhradip Ghosh, *First-principles based investigation of the lattice dynamics in* $Ni_{0.50}Pt_{0.50}$, "Condensed Matter Days 2011 (CMDAYS'11)' at Gauhati University, Guwahati, India (2011).
3. **Souvik Paul** and Subhradip Ghosh, *An ab-initio study of the structural and magnetic properties of* Mn_2NiSn, "International Workshop on Functional Materials (IWFM-2011)" at NIST Brahmapur, Orissa, India, December 20- 22, 2011.
4. **Souvik Paul** and Subhradip Ghosh, *Effect of chemical disorder on the magnetism in inverse Heusler alloy* Mn_2NiSn, "57^{th} Department of Atomic Energy-Solid State Physics Symposium (DAE-SSPS 2012)" at IIT Bombay, Mumbai, India, December 3-7, 2012.
5. **Souvik Paul** and Subhradip Ghosh, *First-principles based study of magnetizations in* Mn_2NiSn *shape memory alloy*, "Electronic Structure Approaches to Atoms, Molecules, Clusters and Solids" at Advanced Centre of Research in High Energy Materials, University of Hyderabad, Andhra Pradesh, India, December 7-11, 2013.
6. **Souvik Paul**, Subhradip Ghosh and Biplab Sanyal, *Volume dependent magnetic ordering in* Mn_2NiX *alloys with inverse Heusler structure*, "International Conference on Magnetic materials and Applications (MagMA-2013)" at IIT Guwahati, Assam, India, December 5-7, 2013.
7. **Souvik Paul**, Subhradip Ghosh and Biplab Sanyal, *Vibrational properties of* Mn_2NiX *alloys in inverse Heusler structure*, "Asia Sweden Meeting on understanding Functional materials from Lattice Dynamics (ASMFLD-2014)" at IIT Guwahati, Assam, India, January 9-11, 2014.

Schools/ Workshops/ Conferences attended

1. *Condensed Matter Days 2011 (CMDAYS'11)* at Gauhati University, Guwahati, India August 24-26, 2011.
2. *International Workshop on Functional Materials (IWFM-2011)* at NIST Brahmapur, Orissa, India, December 20-22, 2011.
3. *57^{th} Department of Atomic Energy-Solid State Physics Symposium (DAE-SSPS 2012)* at IIT Bombay, Mumbai, India, December 3-7, 2012.
4. *Electronic Structure Approaches to Atoms, Molecules, Clusters and Solids* at Advanced Centre of Research in High Energy Materials, University of Hyderabad, Andhra Pradesh, India, December 7-11, 2013.

5. *International Conference on Magnetic materials and Applications (MagMA-2013)* at IIT Guwahati, Assam, India, December 5-7, 2013.
6. *Asia Sweden Meeting on understanding Functional materials from Lattice Dynamics (ASMFLD-2014)* at IIT Guwahati, Assam, India, January 9-11, 2014.